



1

0062725

TECH LIBRARY KAFB, NM

# **HIGH-POWER AND 2.5 kW ADVANCED-TECHNOLOGY ION THRUSTER**

Final Report

By

Ion Physics Department Staff  
Hughes Research Laboratories  
A Division of Hughes Aircraft Company  
3011 Malibu Canyon Road  
Malibu, CA 90265

Prepared For

NATIONAL AERONAUTICS AND SPACE ADMINISTRATION

NASA LEWIS RESEARCH CENTER

Contract NAS 3-19703

William R. Kerslake, Program Manager







0062725

## TECHNICAL REPORT STANDARD TITLE PAGE

1. Report No. NASA CR-135,163		2. Government Accession No.		3. Recipient's Catalog No.	
4. Title and Subtitle HIGH POWER AND 2.5 kW ADVANCED TECHNOLOGY ION THRUSTERS				5. Report Date February 1977	
				6. Performing Organization Code	
7 Author(s) R.L. Poeschel, et al.				8. Performing Organization Report No.	
9. Performing Organization Name and Address  Hughes Research Laboratories 3011 Malibu Canyon Road Malibu, CA 90265				10. Work Unit No.	
				11. Contract or Grant No. NAS 3-19703	
12. Sponsoring Agency Name and Address National Aeronautics and Space Administration Lewis Research Center 21000 Brookpark Road Cleveland, OH 44135				13. Type of Report and Period Covered Final Report 27 May 1975-26 Sep 1976	
				14. Sponsoring Agency Code	
15. Supplementary Notes  Project Manager: William R. Kerslake, NASA Lewis Research Center, Cleveland, Ohio					
16. Abstract <p>This report describes work performed to advance ion thruster technology in several important areas. One task of the program was devoted to examining possibilities for improving component technology that could be utilized in the 30 cm Engineering Model Thruster (EMT). The topics covered included grid short removal techniques, discharge chamber erosion testing, study of double ionization processes, development of advanced cathode technology, evaluation of barium impregnated porous tungsten cathode inserts and porous tungsten vaporizer material, and a study of magnetic circuit design considerations. The program resulted in demonstration of useful techniques for grid short removal and discharge chamber erosion monitoring, establishment of relationships between double ion production and thruster operating parameters, verification of satisfactory specifications on porous tungsten vaporizer material and barium impregnated porous tungsten inserts, demonstration of a new hollow cathode configuration, and specification of magnetic circuit requirements for reproducing desired magnetic mappings.</p> <p>A second task was devoted to determining the capacity of a 30 cm EMT to operate at higher beam voltages and currents (higher power). Operation at 2 A beam current and higher beam voltage (2 to 5 kV) was shown to be essentially equivalent to operation at 1.1 kV with regard to efficiency, life-time and operating conditions. The only additional requirement is an improvement in high voltage insulation and propellant isolator capacity. Operation at minimum voltage (1.1 to 1.3 kV) and higher beam currents (2 to 4 A) was shown to increase thruster discharge chamber erosion in proportion to beam current. All components appear capable of meeting operating requirements for higher beam currents, however, the total extraction voltage must be increased to obtain beam currents greater than 2.5 A.</p> <p>A final task was to explore alternatives to molybdenum for manufacturing ion optics grids. No direct substitution for molybdenum could be found and an evaluation of stainless steel grids showed them to be mechanically unstable in the EMT design configuration.</p>					
17. Key Words (Selected by Author(s)) Electric Propulsion 30 cm Ion Thruster Double Ion Thrust Loss Mercury Propellant				18. Distribution Statement  UNCLASSIFIED — Unlimited	
19. Security Classif. (of this report)  Unclassified		20. Security Classif. (of this page)  Unclassified		22. Price*	
				21. No. of Pages 132	

***PAGE MISSING FROM AVAILABLE VERSION***

## FOREWORD

The work described herein was performed in the Hughes Research Laboratories Ion Physics Department of the Hughes Aircraft Company. This department is managed by Mr. J.H. Molitor. The work was performed under Contract NAS 3-19703, monitored by Mr. William R. Kerslake of NASA Lewis Research Center. Major technical contributions to this effort were made by:

R.L. Poeschel	Project Manager and principal investigator
R.P. Vahrenkamp	Double ionization studies and high power thruster operation
R.L. Seliger	Hollow Cathode Studies
S. Kami	Ion Optics Design and Fabrication
L. Dulmage, R. Scholl, and J. Wood	Data collection, instrumentation, and technical assistance

***PAGE MISSING FROM AVAILABLE VERSION***

## SUMMARY

The High-Power and 2.5 kW Advanced-Technology Ion Thruster Program has been conducted as several independent but related projects directed towards extending the capabilities and operating limits of 30 cm thruster technology. Thruster investigations were carried out using a thruster representative of the 700-800 series engineering model thruster (EMT). Under the category of thruster improvements, several subprojects were successfully completed and appreciable progress was made on others. One project that was completed demonstrated the removal of ion optics short circuits caused by metallic flakes by using a pulsed capacitive discharge. This process was shown to be effective in clearing shorts without causing appreciable electrode damage. In another completed project, the magnetic circuit was analyzed and extensively documented to show which elements most affect the thruster magnetic induction distribution. Only those components affecting the cathode region were found to be hyper-critical. Significant progress was made in developing multilayer thin-film erosion monitors for evaluating discharge chamber sputtering rates. Meaningful measurements can now be made in 8 to 10 hr test time. Similarly, the investigation of double-ion formation processes has advanced the documentation and modelling of discharge chamber processes. The only obvious avenues of approach to reducing double-ion production that can be identified from the results obtained are a lowering of plasma potentials (without loss of efficiency) through use of small-hole accelerator grids, and an improvement in plasma density uniformity — perhaps by use of some form of boundary (cusped) magnetic configuration. A hollow cathode configuration was investigated that required neither alkaline earth nor a heater for operation. Cathode operation was achieved under conditions similar to those required of thruster cathodes, but integration into a thruster was only partially successful. Preliminary investigation of barium impregnated porous tungsten cathode insert material showed that barium depletion is not excessive for temperatures below  $1100^{\circ}\text{C}$ . Although the results obtained are not totally conclusive,

they indicate that the impregnated inserts should have more than adequate lifetime. Finally, porous tungsten material obtained from a commercial vendor was evaluated to determine its suitability for vaporizer fabrication. The samples tested were satisfactory in all respects.

The work performed to explore operation (thrust) of a 30 cm thruster at higher power levels successfully demonstrated operation at both high (6500 sec) and low (3100 sec) specific impulse. Low specific impulse operation was achieved at the minimum beam voltage required (1100 to 1300 V) to extract the desired beam current (up to 4 A). High impulse operation at 2 A beam current has negligible effect on thruster operational characteristics (e.g., propellant utilization stability, sputtering erosion). Operation at high current (4 A), however, results in significantly higher erosion rates but only slightly higher operating temperatures. The EMT ion optics design tested was marginal for 4 A operation below about 2200 V total extraction voltage. Except for these considerations, there were no other observations that can be construed as deterrents to high-power operation.

A study was conducted in an attempt to identify an alternative to molybdenum for fabrication of ion optics grids. Although there is no apparent material which could be readily substituted, several materials have the desired properties (Ta, Cb, Ti). A process for chemical milling the apertures would have to be developed for these materials to make use of proven fabrication techniques. An experimental set of stainless-steel grids were built and tested with partial success. The forming and chemical etching processes were successfully completed but only 1 A of beam current could be extracted without producing inter-electrode short circuits. Operation was marginal and test results indicated that the source of difficulty was the relatively high thermal expansion coefficient of stainless steel in combination with the electrode and support configuration now used. Although stainless steel should not be totally ruled out as a possibility, a new mechanical design will be required to achieve successful operation at 2 A beam current.

## TABLE OF CONTENTS

Section		Page
	SUMMARY . . . . .	v
I.	INTRODUCTION . . . . .	1
II.	IMPROVEMENTS FOR 30 cm THRUSTER TECHNOLOGY. . . . .	3
	A. Sputtering Erosion Monitors . . . . .	3
	B. Doubly Charged Ion Investigation . . . . .	32
	C. Improved Cathode Reliability . . . . .	51
	D. Magnetic Circuit Design . . . . .	56
	E. Neutralizer Insert Tests . . . . .	72
	F. Vaporizer Material Evaluation . . . . .	81
III.	HIGH-POWER OPERATION OF A 30 cm THRUSTER . . . . .	89
	A. Operation of a 30 cm Thruster at Increased Beam Current . . . . .	89
	B. Operation of a 30 cm Thruster at Increased Beam Voltage . . . . .	98
	C. Short-Duration Endurance Evaluation . . . . .	101
IV.	DESIGN AND FABRICATION OF ION OPTICS ELECTRODES FOR LARGE DIAMETER THRUSTERS . . . . .	103
	A. Alternative Grid Material Study . . . . .	103
	B. Stainless-Steel Grid Ion Optics Assembly . . . . .	108
V.	CONCLUSIONS . . . . .	113
	REFERENCES . . . . .	117

***PAGE MISSING FROM AVAILABLE VERSION***



## LIST OF ILLUSTRATIONS

Figure		Page
1	Illustration of the ion machining technique used to measure the layer thickness of the multilayer erosion monitor deposition sample . . . . .	7
2	Photographs of multilayer erosion monitors as mounted on internal thruster surfaces for erosion measurements . . . . .	8
3	Illustration of "diagnostic etch" for erosion monitor analysis . . . . .	9
4	Photograph of interface between masked and unmasked region of erosion monitor after the diagnostic etch . . . . .	10
5	Photographs showing examples of charge exchange erosion patterns seen on multilayer erosion monitor attached to the downstream side of the accelerator electrode . . . . .	12
6	Schematic diagram of short removal circuit . . . . .	17
7	Current waveform and equivalent circuit assumed for grid short clearing current analysis . . . . .	18
8(a)	Screen grid electrode used for short removal tests . . .	21
8(b)	Accel grid electrode used for short removal tests . . . .	21
9	Results of removing short circuit with 500 V grid clearing circuit . . . . .	24
10	Appearance of electrode apertures after short removal in vacuum . . . . .	25
11	Comparison of electrode aperture before and after removal of 0.005 in. diameter spotwelded shorting wires . . . . .	26
12	Documentation of removal of 0.002 in. diameter spotwelded Ta shorting wire . . . . .	28
13	Schematic diagram of circuit to simulate screen supply output . . . . .	29

Figure		Page
14	Results of removing short circuit with simulated screen supply output . . . . .	30
15	Electrode damage for several values of $C_1$ at 1000 V discharge . . . . .	31
16	Effect of reduced accelerator aperture diameter on perveance and trajectories for EM optics . . . . .	35
17	Theoretical total voltage requirements . . . . .	37
18	Backstreaming limits on thruster centerline . . . . .	37
19	Beam divergence thrust loss for operation at minimum accelerator aperture diameter . . . . .	40
20	Schematic of 30 cm thruster showing approximate equipotential lines . . . . .	42
21	Simulation of upstream potential distribution showing calculated ion trajectories . . . . .	43
22	Dimensions of 400 series and 700 to 900 series baffle support . . . . .	45
23	Effect of grid open area on double ion content . . . . .	49
24	Theoretical double ion ratios utilizing parameters representative of EM, SHAG 1 and SHAG 2 optics . . . .	49
25	Double ion ratios for EM, SHAG 1 and SHAG 2 optics . . . . .	50
26	Hollow cathode configuration representative of 30 cm thruster technology . . . . .	52
27	Thin wall hollow cathode/baffle polepiece configuration . . . . .	54
28	Power supply schematic for thin-wall cathode operation . . . . .	54
29	Thruster made-up for simulating and documenting magnetic induction distributions . . . . .	57
30	Magnetic field plotting apparatus . . . . .	59
31	Comparison of radial magnetic field component versus axial distance for thrusters . . . . .	60

Figure		Page
32	Comparison of axial magnetic field component versus axial distance for thrusters . . . . .	61
33	Axial magnetic field component . . . . .	62
34	Radial magnetic field component . . . . .	63
35	Axial magnetic field component versus axial location . . . . .	64
36	Radial magnetic field component versus axial location . . . . .	64
37	Dimensions of magnetic circuits representative of 400 series thrusters and 700 series thrusters . . . . .	66
38	Comparison of magnetic field vectors along axial path . . . . .	67
39	Comparison of magnetic field vectors along axial path . . . . .	68
40	Photograph of soft iron member interconnecting radial and axial magnets . . . . .	71
41	Typical neutralizer control characteristic . . . . .	73
42	Variation in characteristic after accumulated time . . .	75
43	Barium loss per 1000 hr versus operating temperature . . . . .	79
44	Comparison of mercury flow rate and vaporizer temperature . . . . .	87
45	Bubble pattern of vaporizer . . . . .	88
46	Comparison of high current points with maximum perveance limit . . . . .	91
47	Schematic drawing of thruster discharge chamber . . . .	95
48	Schematic drawing of thruster discharge chamber showing thermocouple locations . . . . .	96
49	30 cm dished grid hydroforming press and fixture . . . .	104

Figure		Page
50	Grid stress relieving fixture . . . . .	105
51	Ion optical system assembly using titanium support ring . . . . .	109
52	Stainless steel electrode spacing chart showing region of arcing . . . . .	111

## LIST OF TABLES

Table		Page
1	Average Current per Hole Characteristics for 30 cm Dished Grid at 2 A Beam Current . . . . .	34
2	Optics Specifications . . . . .	39
3	Beam Dispersion Data . . . . .	39
4	Volume Averaged Plasma Properties for EMT and SHAG 1 Optics . . . . .	42
5	Summary of 1000 hr Insert Test Data Determined by Insert Weight Loss . . . . .	78
6	Summary of 1000 hr Insert Test Data Determined by Chemical Analysis of the Insert and Cathode . . . .	80
7	Composition of Endurance Test Mercury Samples . . . . .	83
8	Vaporizer Material Test Summary . . . . .	85
9	Grid Parameters of the Ion Optical System . . . . .	90
10	Thruster Performance Data . . . . .	93

## I. INTRODUCTION

The objectives of this High-Power and 2.5 kW Advanced-Technology Ion Thruster Program were to develop new technology applicable to the improvement of 30 cm thrusters (now being developed under engineering model thruster (EMT) programs, and also to explore the feasibility and methods of obtaining high power operation of a single thruster module. The program was divided into three major more or less independent tasks. Task I covered technology areas where improvements could be useful to current or future EMT development efforts. Subtasks of Task I treated the subjects of sputter erosion monitoring, double ionization processes, advanced cathode technology, magnetic circuit design considerations, clearance of ion optics grid shorts, neutralizer insert evaluation, and porous tungsten vaporizer material evaluation. Work under Task II investigated the operation of a 30 cm thruster (representative of the 700 series EMT design) at higher power levels (up to 10 kW) either by increasing the beam voltage or beam current. Lifetime implications of high power operation were evaluated under this task also. Task III provided an evaluation of materials other than molybdenum for ion optics electrode fabrication in the event that molybdenum is unavailable in the size, quantity or quality required in the future. A stainless steel electrode set was evaluated. Discussion of the work performed is organized in the following three sections in approximately the same format as the task description.

***PAGE MISSING FROM AVAILABLE VERSION***

## II. IMPROVEMENTS FOR 30 cm THRUSTER TECHNOLOGY

Development of 30 cm thrusters at both NASA Lewis Research Center (NASA LeRC) and Hughes Research Laboratories (HRL) has brought the technology level to an application-ready status. The work performed under this task had the objectives of reinforcing thruster documentation and evaluating possible alternatives for improving EMT technology. Several topics were covered, varying from discharge chamber erosion monitoring to evaluation of commercially available porous tungsten for vaporizer fabrication. The scope and relative completeness of these studies also varied in that topics such as the study of double-ionization processes were sufficiently broad and fundamental that only a limited number of parameters were evaluated whereas other topics such as the magnetic circuit design study and the grid clearance experiments, were sufficiently limited in scope that little, if any, benefit could be anticipated by pursuing these subjects further. The other projects — erosion monitoring, hollow cathode improvements, neutralizer insert evaluation, and porous tungsten vaporizer evaluation — fall somewhere between these extremes. The work performed is described in the following sections.

### A. Sputtering Erosion Monitors

Endurance testing of 30 cm thrusters has shown that erosion of discharge chamber components by ion sputtering is a life-limiting factor that requires careful consideration in the design of a long-life thruster system.<sup>1,2</sup> Two aspects of this problem are explored here. They deal with how to (1) monitor erosion without long-term testing, and (2) remove flakes of backspattered material that have short-circuited the grids of the accelerator assembly. Both of these projects were successfully completed under this program.



## 1. Sputtering Erosion Monitors

Performance on this task was aided considerably by the concurrent sputtering erosion measurements being performed (under COMSAT Contract IS-679, Ref. 3) on an 8 cm thruster discharge. Results from this work allowed us to quickly reject several techniques. Three constraints were placed on the selection of an erosion monitoring technique; it should:

- Not require radical thruster modification
- Be capable of producing test results in a short time period (10 to 40 hr)
- Not require abnormal thruster operation.

The third constraint was imposed to facilitate evaluating the effects of changes in operating parameters.

In consideration of the above constraints, the objective of this erosion monitor development was to demonstrate a capability for monitoring erosion rates with better than order of magnitude accuracy as a function of "normal" thruster operating parameters and in a relatively short time period. This is in contrast to operating the thruster for short periods of time under extreme operating conditions to accelerate erosion rates for identifying erosion sites and determining relative erosion of thruster components. Post test examination of the 30 cm thruster tested for 10,000 hours under the Endurance Test Program (NAS 3-15523) has provided adequate information to identify erosion sites and to determine relative erosion rates. Consequently, the task here was one of determining submicron changes in surfaces. Two techniques considered were

- Surface profilometer measurement of polished surfaces
- Determination of material removed from a specially layered material.

The first technique is quite simple to perform in the sense that the surface profile is easily measured. However, interpreting the

results is quite difficult. The initial sample surface must be polished until it has variations less than the anticipated erosion. A suitable "bench mark" must be established to serve as a reference for determining the amount of material eroded away. Several attempts were made to achieve these conditions under the COMSAT program without consistent success. The initial polished surface could be obtained, but we were unsuccessful in establishing a suitable reference using the usual discharge chamber materials because:

- Operating the polished element in the thruster produces warping and destroys the accuracy of the reference
- Masking to obtain a reference distorts the erosion pattern near the edge of the mask (distortion depends on the mask's thickness), and too much "scanning" distance is required to produce an accurate depth measurement.

Consequently, the development effort on the erosion monitor was concentrated on adapting the alternating thin-film technique to the measurement of the anticipated rates.

Since this technique can be readily adapted to measuring surface erosion rate, two multilayer monitoring materials were explored. One consisted of alternated layers of molybdenum and copper deposited on a stainless-steel substrate; it was used to monitor screen grid erosion. The substrate material was perforated to match the screen grid hole pattern. The second monitoring material consisted of alternated layers of tantalum and copper deposited on either a stainless-steel or tantalum substrate; it was used to monitor the tantalum pole piece (baffle) cover erosion. The alternated laminar films were made by sputter deposition in the Sputtering Processes Laboratory of HRL. Layer thickness was carefully controlled by maintaining the sputtering ion beam voltage and current constant and by precisely timing the deposition. A small piece of polished material was sputter deposited during preparation of the multilayer monitor material for calibration purposes.

Layer thickness was calibrated by measurements on the coated, polished sample as follows. First, a pattern of 25  $\mu\text{m}$  lines and spaces

was established on the sample surface using optical exposure of photoresist through a suitable mask. The multilayer material was then ion beam machined away as shown in Figure 1 to make the layer interfaces readily identifiable. After that step, the photoresist mask was removed chemically; and the original polished surface provides the necessary bench mark for Dektak\* measurements. By guiding the Dektak stylus along the readily identified interface between layers, the interface depth can be determined for each interface, thereby determining layer thickness. The layer thickness of samples analyzed in this manner was approximately  $60 \pm 0.6$  nm for the usual deposition control conditions.

Portions of the thin-film substrate were mounted on the thruster components, as shown in Figure 2 with a portion of the monitor masked. The thruster was operated long enough to remove several, but not all, of the 60 nm layers. Typical monitors had eight tantalum or molybdenum layers and seven copper layers, with the first layer (Mo or Ta) being double thickness. Because copper erodes about 20 to 40 times faster than either Mo or Ta, the copper layers were factored into the analysis as only a portion of a layer. Therefore, the total thickness of the deposited layers was equivalent to approximately 566 nm of Mo or 553 nm of Ta.

The monitors were removed and analyzed after the thruster was operated. Since it was not always possible to identify the layer interfaces at the boundary of the region masked during the test, a "diagnostic etch" was required. The etch formed an angular cut through the remaining layers, which allowed rapid identification of the interfaces by the same procedure as used calibrating the deposition sample. This was done quite simply by "loosely" masking the sample and then ion beam machining a groove in the remaining layers, as shown in Figure 3. Positioning the mask above the surface as shown provides the tapered edge in the groove. Photomicrographs of the diagnostic etch region are shown in Figure 4. Figure 4(a) shows the blistering that sometimes occurred; such blistering makes it impossible to analyze the

---

\*Dektak Surface Profilometer, Sloan Instrument, Inc., Santa Barbara, Calif.

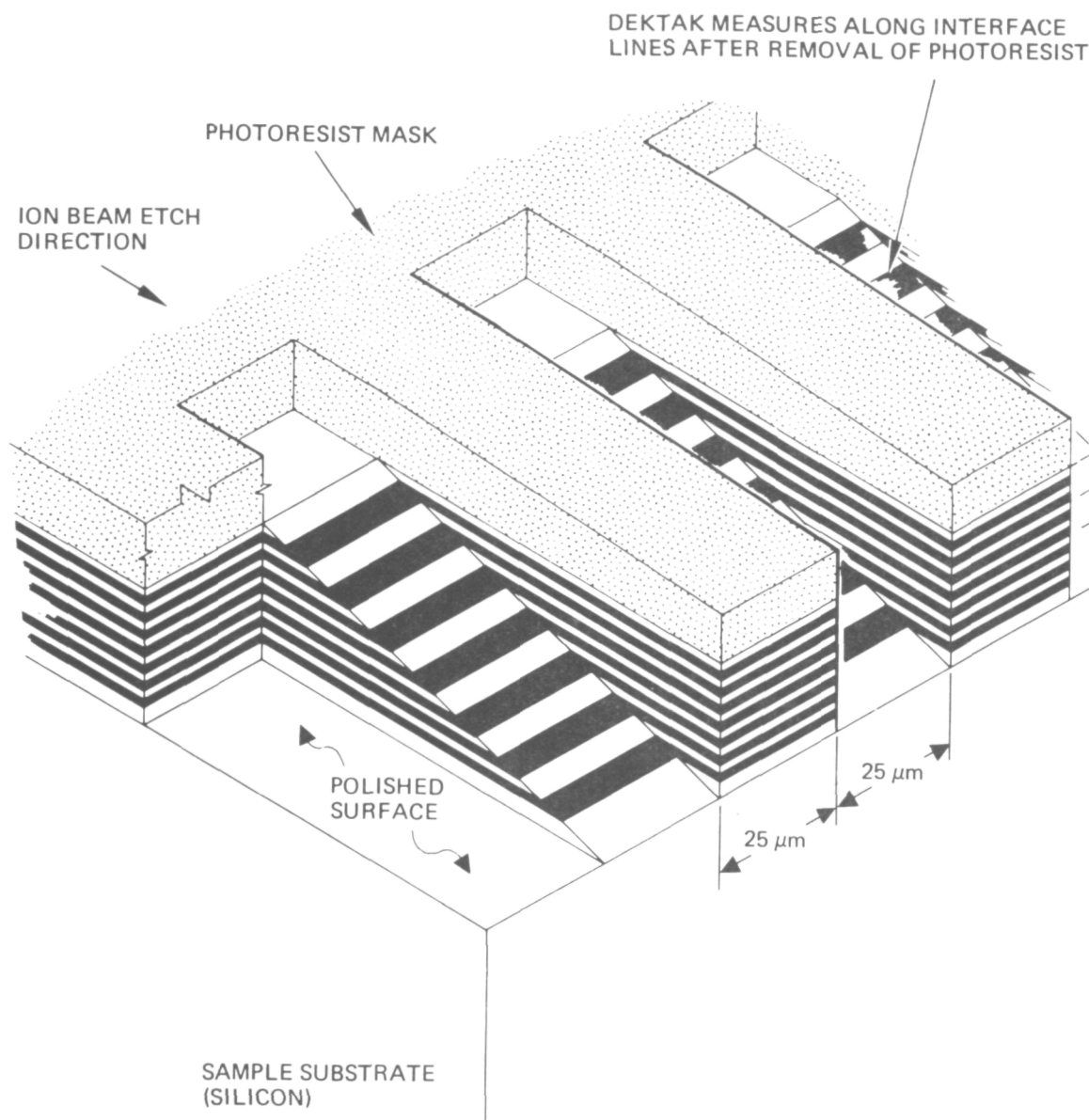
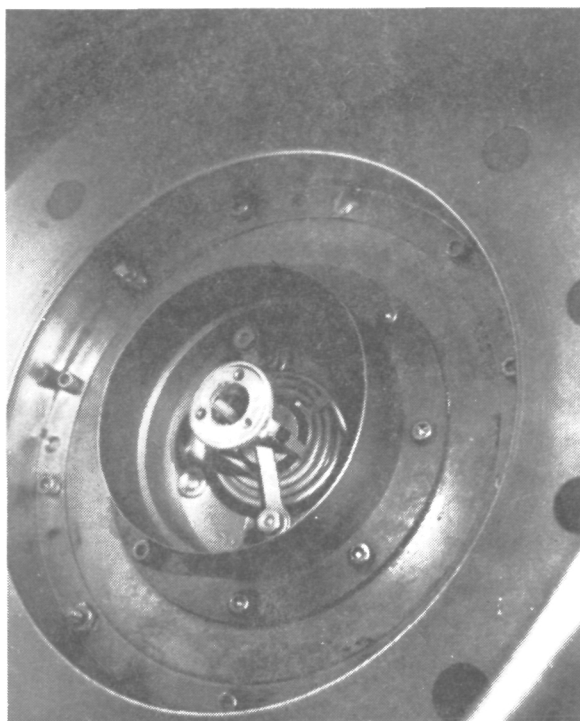
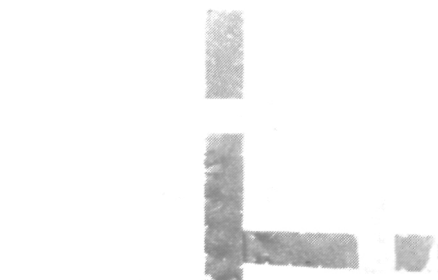


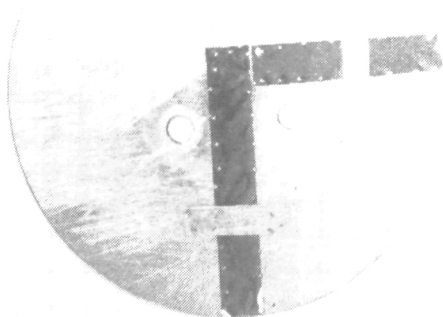
Figure 1. Illustration of the ion machining technique used to measure the layer thickness of the multilayer erosion monitor deposition sample.



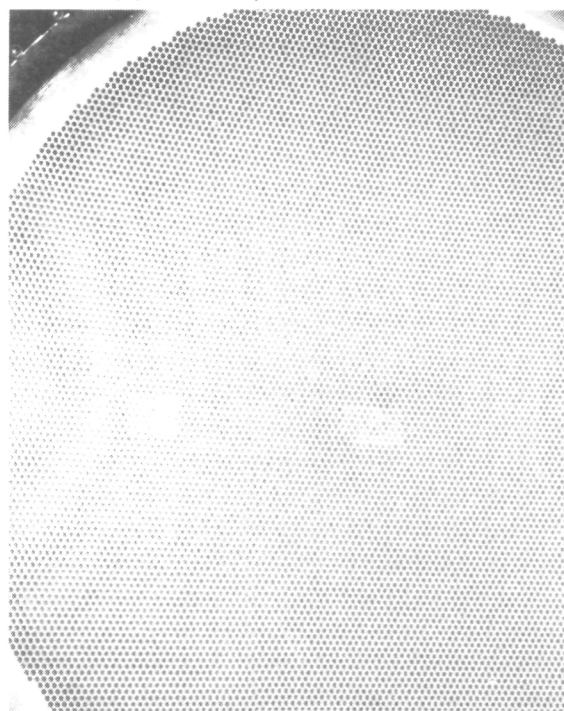
(a) BAFFLE SUPPORT



(b) BAFFLE, UPSTREAM SIDE



(c) BAFFLE, DOWNSTREAM SIDE



(d) SCREEN ELECTRODE, UPSTREAM SIDE

Figure 2. Photographs of multilayer erosion monitors as mounted on internal thruster surfaces for erosion measurements.

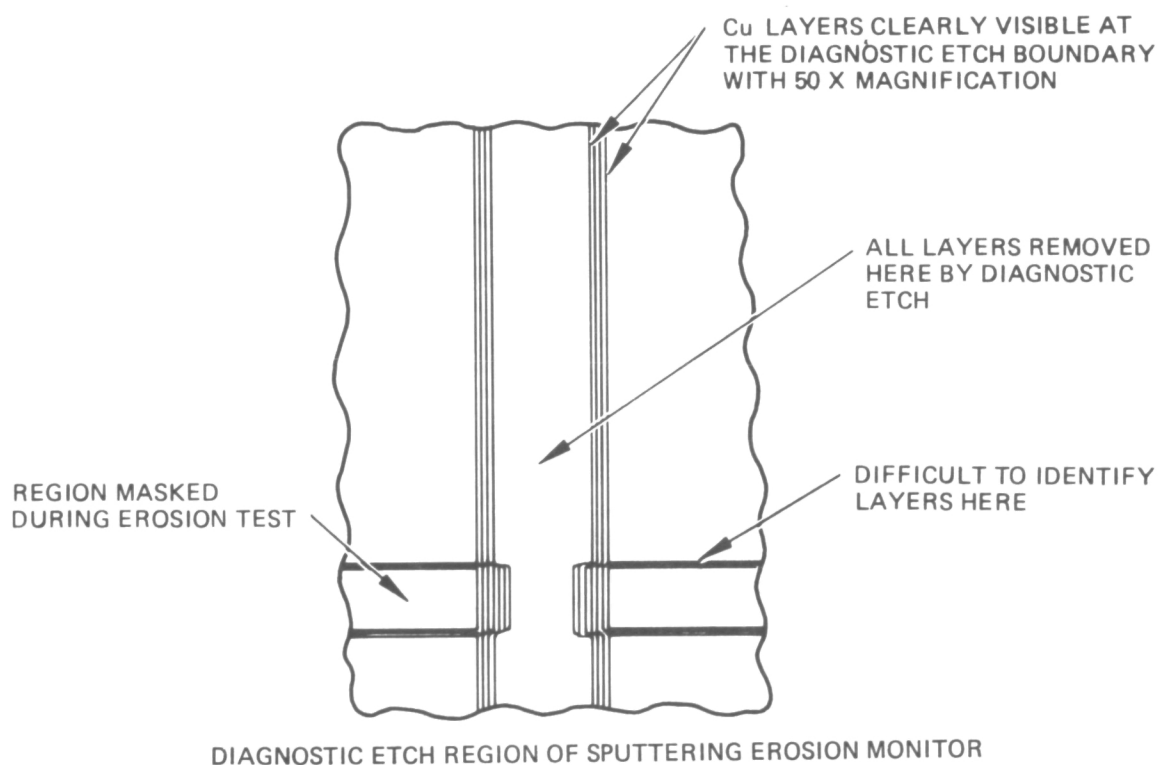
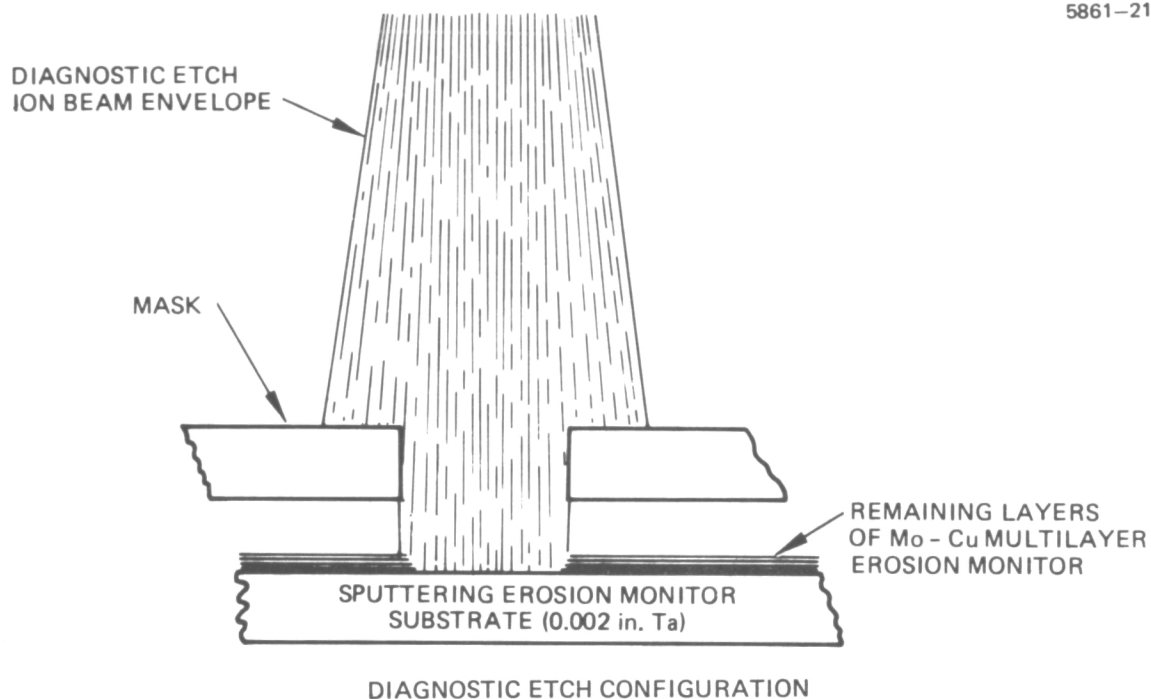


Figure 3. Illustration of "diagnostic etch" for erosion monitor analysis.



Figure 4. Photograph of interface between masked and unmasked region of erosion monitor after the diagnostic etch (500x).  
(a) Layers have "blistered" and are impossible to analyze  
(b) Remaining layers can be distinctly followed from masked region to unmasked region (4 layers remaining).

the lower copper layers darkened is not known; these layers did not darken in the calibration sample material.

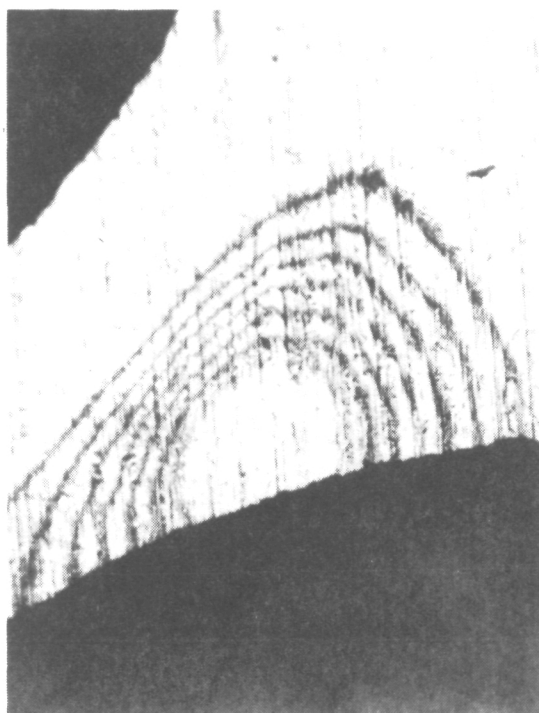
Multilayer erosion monitors were also used on the downstream accel electrode surface to monitor charge-exchange erosion. Figure 5 shows the typical charge-exchange erosion pattern for two locations. The erosion pattern indicates that the charge-exchange ions were focused by the space-charge potentials of the ion beam in each aperture. Consequently, the observed pattern displacement in Figure 5(a) indicates that the ion beamlets were not centered as well in the adjacent apertures as they were for the pattern shown in Figure 5(b). This displacement is to be expected for a compensated, dished ion-optics set since the beamlets are vectored towards the axis and consequently pass through the accel apertures nearer the inner boundary. Since a very regular offset pattern is expected around the grid periphery, these monitors could serve as a check on the screen-grid/accelerator-electrode alignment accuracy as well as for erosion rate monitors.

The absolute accuracy of multilayer thin-film erosion monitors was not completely evaluated because there are several unknowns which were considered too basic to evaluate within the scope of this project. Among the factors which were not adequately investigated are:

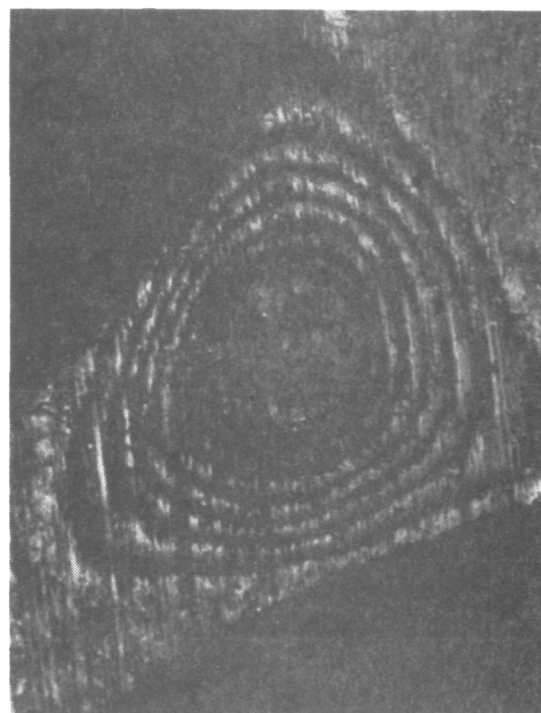
- Sputtering rate of sputter-deposited material as compared to bulk material
- Dependence of sputtering rates or deposition rates on ambient conditions (partial pressure of impurities)
- Uniformity of sputter-deposited layers
- Dependence of sputtering rates on temperature or possible error introduced because the thin monitor material was not the same temperature as the surface being monitored

Using multilayer monitors requires making assumptions with respect to each of these factors. First, it was necessary to assume that sputter deposited material erodes at the same rate as bulk material, and that ambient vacuum facility conditions have insufficient impurity concentrations to affect these rates (both for deposition of the laminar





(a)



(b)

Figure 5. Photographs showing examples of charge exchange erosion patterns seen on multilayer erosion monitor attached to the downstream side of the accelerator electrode.

films and erosion monitoring). Second, it was assumed that the layers are uniform to within  $\pm 1\%$  of layer thickness over the area of the monitor material and of the calibration sample and from layer to layer. Finally, it was assumed that deposition and erosion processes are unaffected by the temperature of the thin substrate, and that the multi-layer monitor attains the same temperature as the surface on which it is mounted.

Perhaps the best justification for using these laminar film-erosion monitors can be made by comparing the screen grid erosion rate in the endurance test of thruster SN 701 with the rates measured for thruster SN 301B under similar conditions. Assuming that the material removed in  $10^4$  hr was 0.18 mm of molybdenum ( $\sim 0.007$  in.), the erosion rate in the center of the grid for operation at 1.4 A beam current was 18 nm/hr. This erosion rate can be extrapolated to 35.0 nm/hr for operating at 2 A beam current by multiplying by the ratio of beam currents (2.0/1.4) and double-ion concentrations (0.15/0.11).<sup>1</sup> Operating thruster SN301B (that thruster is electrically equivalent to the endurance test thruster) at 2 A beam current for 15 hr removed seven layers of Mo and nearly seven layers of Cu—an equivalent thickness of 433 nm of Mo. This is equivalent to an erosion rate of 28.8 nm/hr and is in reasonably good agreement considering the uncertainties present.

The double- and single-ion concentrations measured on axis in thruster SN301B can be used to predict the erosion rate of the screen grid. The measured double-ion current density was  $1.9 \text{ mA/cm}^2$ , and the single-ion current density was  $4.1 \text{ mA/cm}^2$ . The erosion rate,  $W$ , in nm/hr for molybdenum can be shown to be

$$W_{++} = 1753 J_{++} S_{++} \quad (1)$$

and

$$W_{+} = 3506 J_{+} S_{+} \quad , \quad (2)$$

where the subscript determines the ion species,  $J$  is the current density in  $\text{mA}/\text{cm}^2$ , and  $S$  (in units of atoms per ion) is the sputtering coefficient for the ion at the appropriate energy. Since most ion production is thought to occur in the region of peak plasma potential, the energy of the ions striking the screen is considered to correspond to 40 V acceleration. Hence the values of  $S_{++}$  (80 eV) and  $S_{+}$  (40 eV) are taken to be  $7 \times 10^{-3}$  and  $5 \times 10^{-4}$ , respectively. The total erosion rate is the sum of  $W_{+}$  and  $W_{++}$  and is, therefore, 30.5 nm/hr. This value is slightly higher than that indicated by the erosion monitors and lower than the endurance test extrapolation, however the difference is the same order as the estimated accuracy. Consequently, the multilayer laminar thin-film technique for erosion monitoring is concluded to be an effective means of rapidly evaluating relative erosion rates for changes in operating conditions and surface materials. Absolute accuracy depends on the validity of assumptions made in analyzing the result. Absolute accuracy may also be possible if all the factors discussed earlier can be unequivocally evaluated.

## 2. Clearance of Short-Circuited Ion Optics

The erosion of discharge chamber components and/or the accelerator electrode by ion sputtering generates a flux of metallic material that redeposits and forms thin coatings on thruster surfaces that are not subject to ion bombardment. These thin coatings tend to separate and form flakes of metallic material that vary in size and cross section. These flakes can find their way into the accelerator electrode gap and short circuit the screen and accelerator electrodes.<sup>2</sup> Although some of the smaller flakes are removed by the output capacitance of the screen (or beam) power supply, the current required to clear flakes that have larger cross sections exceeds the capabilities of the power supplies used for normal thruster operation.

Such shorts can be removed quite effectively by discharging a capacitor, charged to high voltage, directly into the short.<sup>2, 5</sup> Damage to the electrodes caused by this intentional arc depends on the shorting conditions and the energy discharged. Initial work by Beebe et al.<sup>5</sup> served to demonstrate the feasibility of short removal by capacitive

discharge and to document the grid damage that can occur under a variety of arc discharges. The experiments described here are an extension of this work to evaluate the circuit requirements necessary for removing short circuits under controlled conditions and to document the grid damage associated with the arc discharge generated. These experiments show that a minimum stored energy of about 2 J is required to clear a "typical" short and that damage to the electrodes at this energy is relatively insignificant. A discussion of what constitutes a typical short and significant damage is included with the description of the experimental procedures and results.

Metallic flakes can be formed by ion sputtering within the discharge chamber or by charge-exchange ion sputtering of the accelerator electrode. In either case, this sputtering produces a flux of atoms that deposit in thin layers at thruster locations that are not subjected to ion bombardment. Eventually, these deposits spall, forming flakes of metallic material. Flakes of 0.04 mm (0.0015 in.) thickness were found in the 700 series 30 cm 10,000 hr endurance test thruster<sup>2</sup> with cross sections in excess of  $1.9 \times 10^{-3} \text{ cm}^2$  ( $3 \times 10^{-4} \text{ in.}^2$ ). This cross section is slightly larger than a 0.127 mm (0.005 in.) diameter wire. Although changes in the design of thruster deposition sites in the 800 and 900 series 30 cm EMTs should reduce the cross sections of flakes by about a factor of 20, a wire having a 0.13 mm (0.005 in.) diameter is considered, somewhat arbitrarily, to be representative of a worst-case "typical" flake.

Next we consider how the short circuit contact is made. If a flake of material finds its way into the ion optics electrode during operation, it could be welded in place by the beam power supply. If it lodges between the electrodes during a period when the thruster is not operating, then there may be only a simple ohmic contact. In either case, the screen and accel power supplies will not turn on normally because of the preset overload limits. Since clearance of the short may occur differently for these two cases, both cases were investigated. The most probable situation is the case representing all the possibilities intermediate to the above limiting cases in which the

metallic short is welded (or partially welded) to one electrode and makes poor contact with the other. Although this intermediate condition may be the worst case insofar as short clearance and grid damage are concerned, it is considered untractable for documentation and systematic study.

The circuit diagram for the grid-clearing experiments is shown in Figure 6. A commercially available spark gap was selected as the switching element because it has the ability to repeatedly switch very large currents in nanosecond time intervals with a low spark-gap voltage drop (30 V). The advantage of the spark gap over a relay contact or an SCR switch is that the energy in the capacitor can be efficiently transferred into fractional ohm load impedances, whereas the current must be limited to prevent damage to relay or switch contacts, and high-current SCRs generally have slow switching times. In either of these latter cases, appreciable energy is dissipated in the switching element instead of in the load. A standard laboratory high-voltage power supply is used to charge the energy storage capacitor ( $C_1$  in Figure 6) through the charging resistor ( $R_1$  in Figure 6).  $R_1$  is selected with  $C_1$  to provide a 10 to 20 sec charge time. When the firing voltage of the spark gap is reached, the capacitor discharges through  $R_2$  and the short circuit applied to the electrode set, thereby eliminating the material causing the short. The worst damage is to be expected when  $R_2 = 0$  and the total capacitor energy is discharged into the short. This energy input to the short is varied in the experiments described below by changing the value of  $C_1$  and the spark-gap firing voltage with  $R_2 = 0$ . The capacitor used for  $C_1$  is a nonpolarized type representative of those used in thruster power processor units.

The current waveform is quite reproducible and does not appear to vary appreciably with the method of attaching the short or with the cross section of the shorting material. Figure 7(a) shows a representative oscilloscope waveform of the current with the appropriate parameters indicated. Figure 7(b) shows an equivalent circuit for the grid-clearing experiment and current measurement. The current  $i(t)$  in this circuit is given by

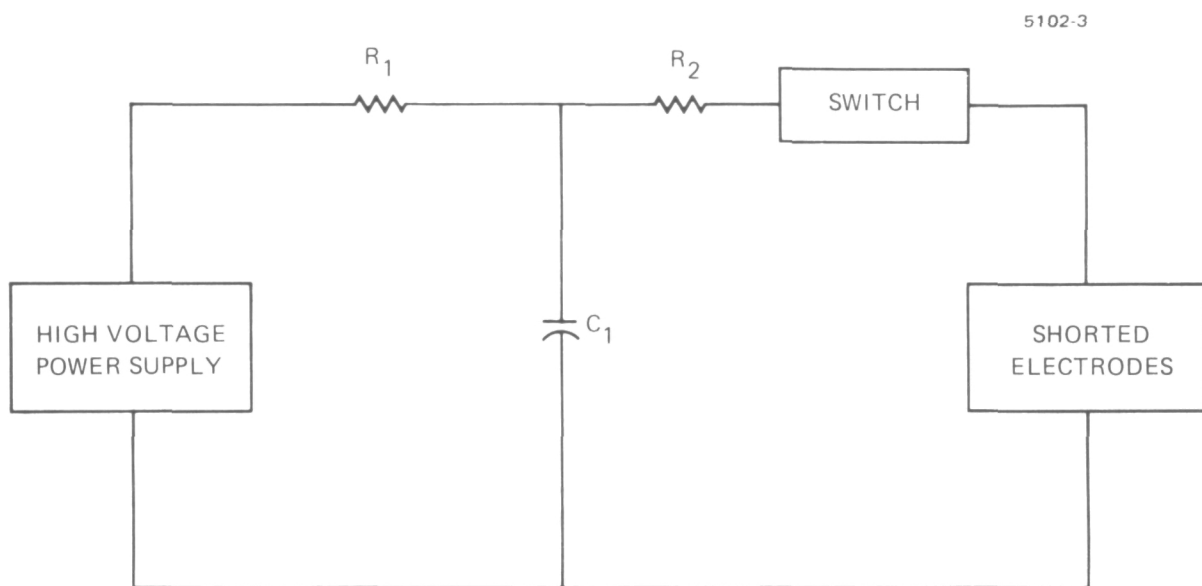
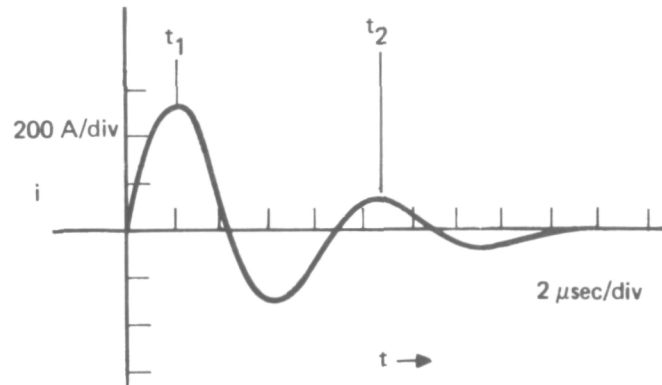


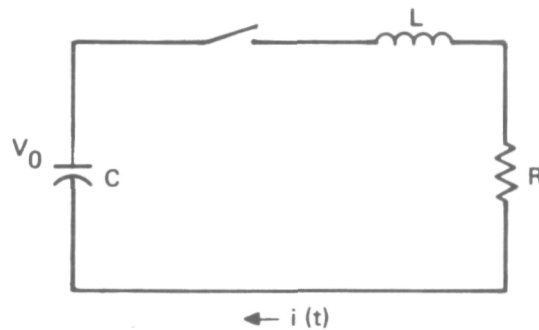
Figure 6. Schematic diagram of short removal circuit.

5102-1



a) OSCILLOSCOPE WAVEFORM FOR CURRENT,  $i(t)$ , IN GRID CLEARING CIRCUIT

5101-2



b) EQUIVALENT CIRCUIT FOR GRID SHORT CLEARING. THE SWITCH REPRESENTS THE SPARK GAP AND R AND L ARE THE LUMPED RESISTANCE AND INDUCTANCE OF THE SWITCH, THE CAPACITOR, C, AND THE WIRING

Figure 7. Current waveform and equivalent circuit assumed for grid short clearing current analysis.

$$i(t) = \frac{V_o}{\omega L} e^{-\zeta \omega_n t} \sin \omega t \quad , \quad (3)$$

where

$$\omega = \sqrt{1 - \zeta^2} \omega_n = \frac{2\pi}{t_2 - t_1}$$

$$\omega_n = \frac{1}{\sqrt{LC}}$$

$$\zeta = \frac{R}{2} \sqrt{\frac{C}{L}} \leq 1 \quad .$$

For waveform shown in Figure 7(a),  $C = 1 \mu\text{f}$ ,  $V_o = 830 \text{ V}$ ,  $t_2 - t_1 = 9 \mu\text{sec}$ , and  $i(t_1)/i(t_2) = 4$ . These values yield

$$\zeta = 0.215$$

$$\omega_n^2 = 1.96 \times 10^{-12}$$

$$L = 1.96 \mu\text{h}$$

$$R = 0.6 \Omega$$

$$i_{\text{max}} = 429 \text{ A} \quad .$$

The waveform shown is the voltage across a  $0.01 \Omega$  shunt, recorded at  $2 \text{ V/div}$ , hence the vertical scale is  $200 \text{ A/div}$ . The measured peak current, which is a  $2.6 \text{ div.}$  deflection, is  $520 \text{ A}$  and agrees reasonably well with the current value calculated from the circuit parameters. On the basis of a few variations in the capacitor value and the shorting wire cross section, the dominant circuit parameters are found to be more a function of the switching element, the lead length, and the capacitor type than of the shorting element; consequently, the equivalent circuit for any grid-clearing device will be determined by the component parameter  $L$  and  $C$ .



The objective of this evaluation was to determine a set of parameters that could clear typical short circuits from the ion optics electrodes without significant damage to the electrodes. The simulation of a typical short circuit has already been discussed and it is now appropriate to discuss the considerations relating to what constitutes grid clearance and significant electrode damage.

In thruster operation, grid clearance would be satisfied if the beam voltage could be applied and a beam extracted without initiating an overcurrent condition. In the simulation experiment conducted here, this condition was interpreted as the removal of all portions of the shorting element that protrude into the interelectrode space. This means that separating the shorting wire in the center of the interelectrode space does not constitute satisfactory grid clearance, even though the short circuit is opened.

A simple set of criteria for evaluating electrode damage cannot be easily formulated. One possible standard might be the absence of visible evidence of electrode material removal from grid clearance. This is too severe a condition to place on the clearance mechanism, since the alternative is in effect a total thruster failure if the ion beam cannot be turned on. Consequently, some damage and visible removal of material should be allowed. However, how much material removal is acceptable is an open question. Consequently, the experiments were performed more with the intent of documenting the visible electrode damage than of attempting to discriminate between an acceptable and an unacceptable amount of damage. The following paragraphs describe the results of these experiments; where appropriate, comments are included concerning the damage observed.

Initial experiments were performed by simply inserting small pieces of wire through a set of electrode apertures to form a short circuit, removing the short by capacitive discharge, and visually observing the results. To facilitate observation, the electrodes were specially prepared by electropolishing to form a reference system and clean surfaces for detecting damage (see Figure 8). Segments of tantalum and molybdenum wire 0.05 mm (0.002 in.) and 0.13 mm (0.005 in.)

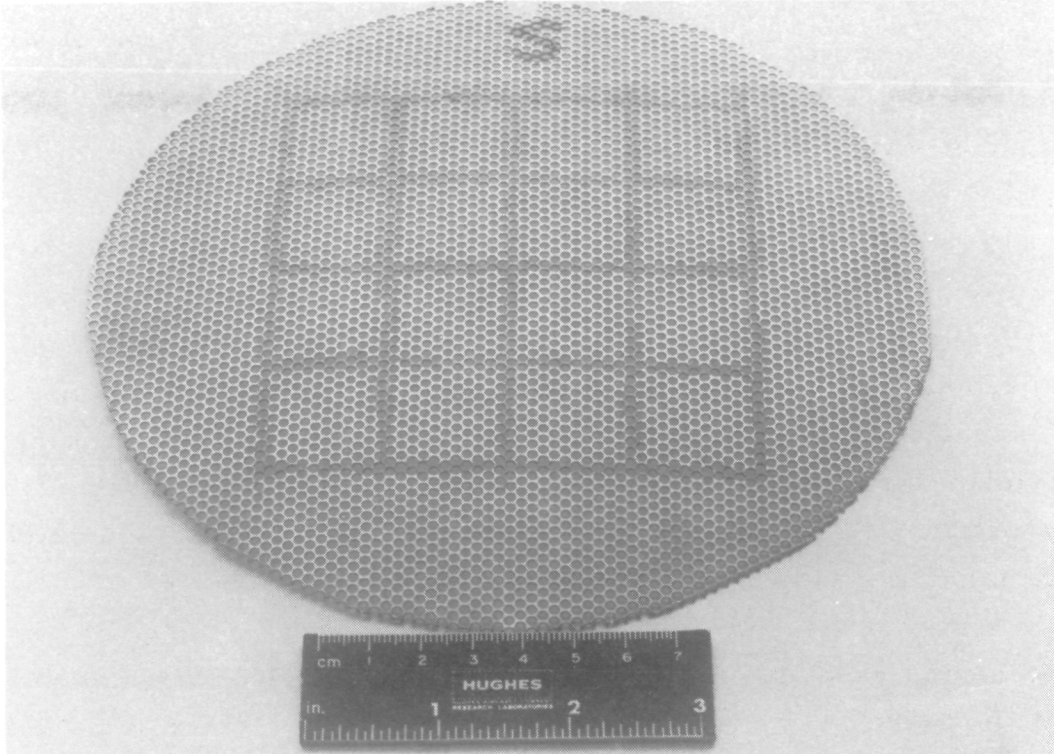


Figure 8(a). Screen grid electrode used for short removal tests.

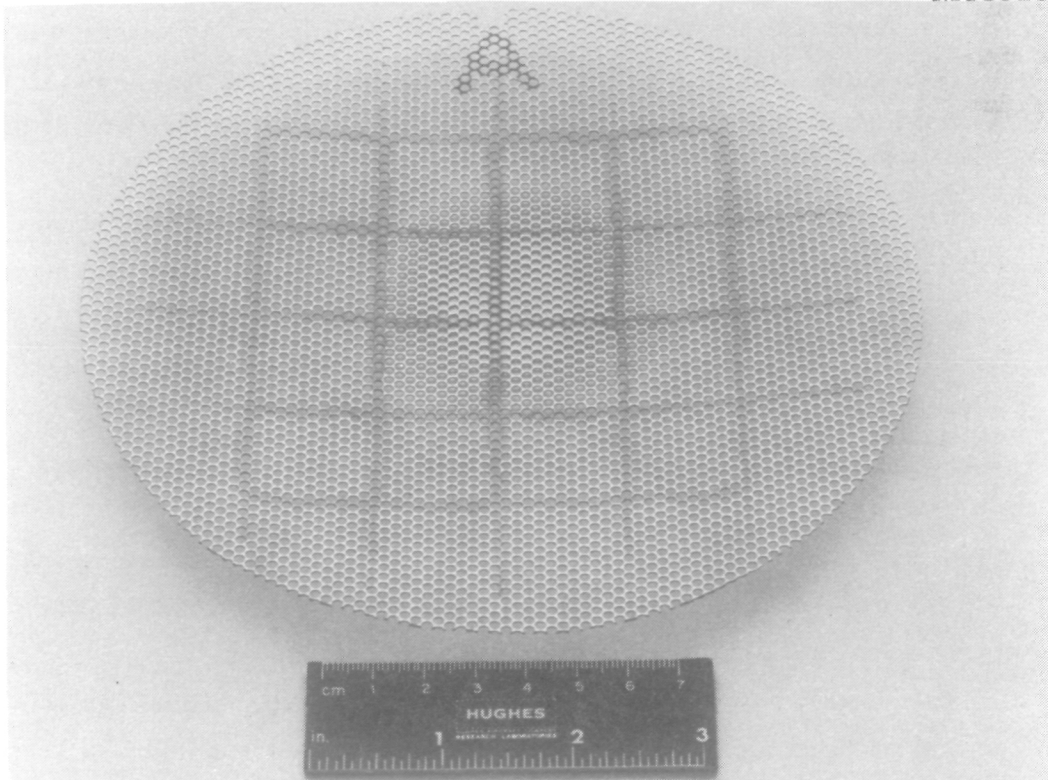


Figure 8(b). Accel grid electrode used for short removal tests.

in diameter were used as short-circuit material representative of flakes that might be formed in future discharge chambers. The circuit of Figure 6 was operated with 0.25 and 1  $\mu\text{f}$  capacitance values for  $C_1$  and spark gap firing voltages of 830 and 1450 V. These shorts were literally "blown away" by all combinations of these voltage and capacitance values with detectable damage to the electrodes seen only for the 1450 V, 1  $\mu\text{f}$  capacitance combination. This damage appeared as a microscopic "chip" where the shorting wire had contacted the electrode; it was considered to be relatively insignificant. It is thought that the mechanism for short removal under these circumstances is either electrostatic or electromagnetic. No difference was observed between the tantalum and molybdenum materials.

As a more severe test of short removal, the shorting wire was spotwelded to each electrode. For the 0.05 mm (0.002 in.) diameter wire, the 0.25  $\mu\text{f}$  capacitor charged to 830 V cleared the short but left the ends of the wire attached to the grids. Inspection under the microscope showed the ends to be slightly "balled" as if the wire had been melted in the center. Increasing  $C_1$  to 1  $\mu\text{f}$  eliminated the wire ends. Although the electrodes were slightly discolored during these tests, it is not possible to differentiate between the discoloration caused by spot welding from that caused by short removal. Similar results were obtained by removing a 0.13 mm (0.005 in.) diameter spot-welded wire using 830 V with 2 and 3  $\mu\text{f}$  capacitance values. In this case, a 1  $\mu\text{f}$  capacitor could not clear the short circuit; the 3  $\mu\text{f}$  capacitor did remove all traces of the shorting wire, but it also caused appreciably greater damage to the electrodes. Thus it is concluded that 2  $\mu\text{f}$  at 830 V would suffice to remove typical short circuits without causing significant electrode damage.

The next experiments were performed to document the characteristics of a grid-clearing circuit being considered by NASA LeRC personnel to provide grid clearance for the entire 30 cm thruster array. This circuit would be permanently connected to all thrusters and isolated by appropriate diodes. Its operation is presently specified at 500 V using a solid-state switch and 0.5 J energy (4  $\mu\text{f}$  capacitance).

Consequently, the detailed documentation that follows was performed using the circuit shown in Figure 6, operated with a 4  $\mu\text{f}$  capacitor as  $C_1$  and a 500 V spark gap to simulate this grid clearing circuit concept. The results of the initial documentation experiments are shown as 50x photographs in Figure 9, in which both Ta and Mo wire segments were placed through the electrode apertures (not welded) and removed by the 500 V circuit. The experiments were performed in air. From left to right, the first view shows the aperture from the accel side with the shorting wire in place, the second photograph is taken with the aperture in the same position after the short has been removed, and the third view shows the screen grid from the opposite side. No marking of the accel electrode is shown by any of the photographs. The screen electrode, which was not photographed before the short removal, was slightly discolored where the wire had made contact, and there may have been a slight material removal. In any case, the marking seen is not considered significant with respect to electrode operation. The most severe case seen in Figure 9 occurred for the 0.13 mm (0.005 in.) Ta wire; this case was selected for testing in vacuum. The experimental conditions for Figure 9 were repeated with the electrode set installed in a bell jar and evacuated to approximately 30 mTorr pressure. Figure 10 shows the results of three repetitions of this test. The electrodes were less marked during these tests than during the tests performed in air.

The technique of simply inserting the wire in the apertures produces a relatively high resistance short, as measured with a low voltage ohmmeter. Therefore, the above test was repeated with the 0.13 mm (0.005 in.) diameter Ta wire spotwelded in place. The 500 V, 4  $\mu\text{f}$  capacitor circuit could not remove this short, even with several operations of the circuit. It was possible to remove the short on the first trial with the circuit of Figure 6 operated with the 1450 V spark gap and the 1  $\mu\text{f}$  value of  $C_1$  ( $R_2 = 0$ ). Figure 11 shows photographs of the aperture with the short in place and after removal (in air). Again, there is some marking of the accel electrode where contact was made by the shorting wire, but it is not certain how much of this marking was

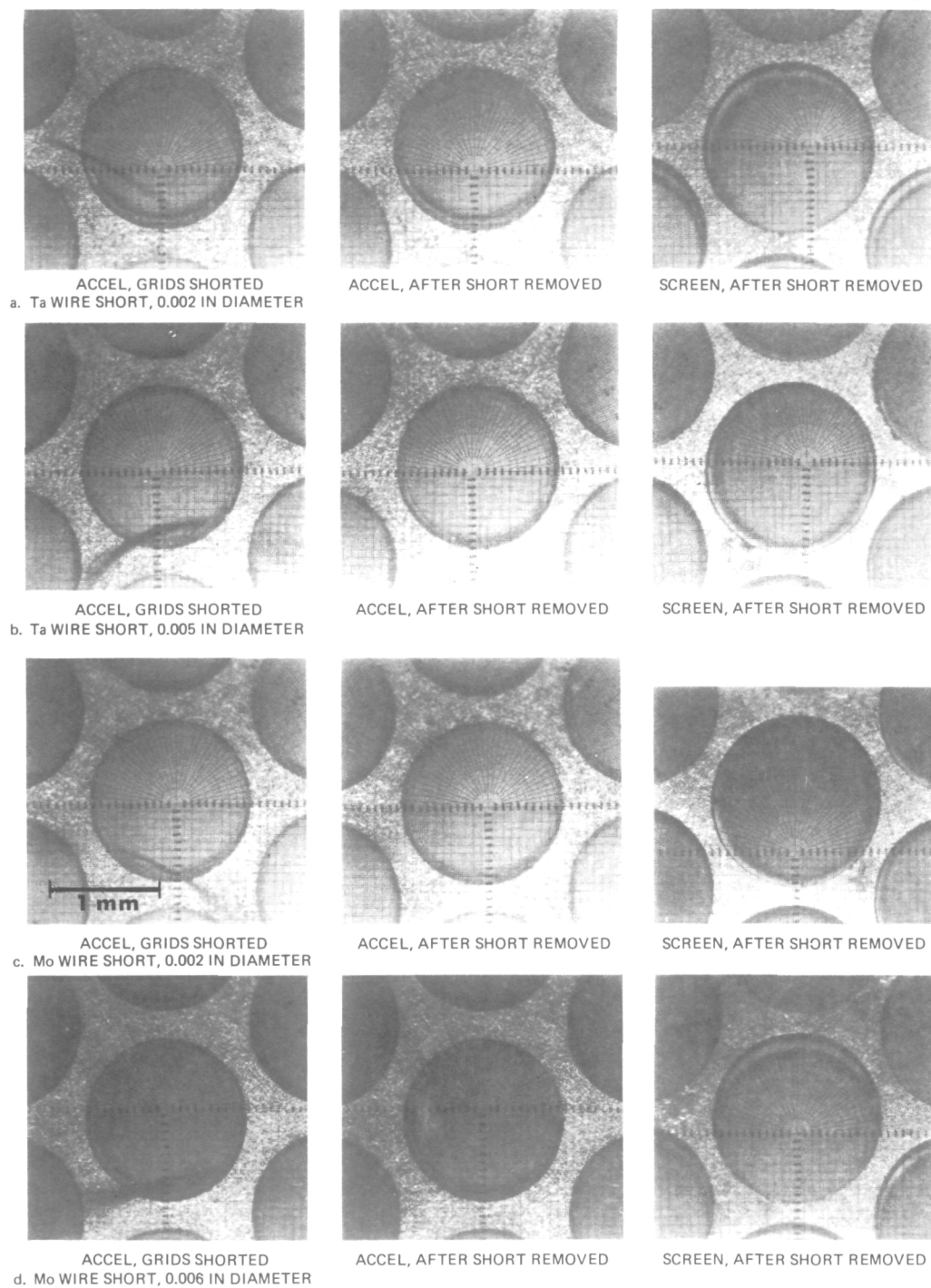
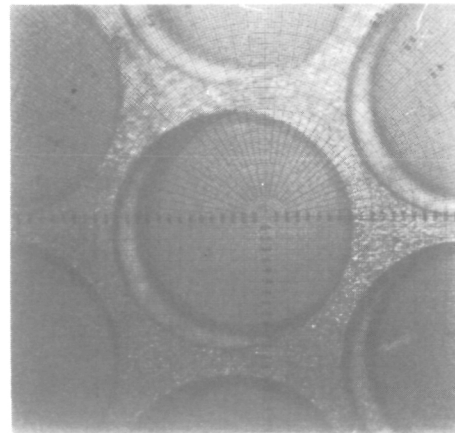
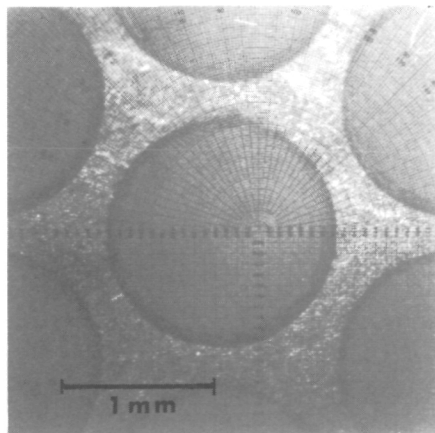
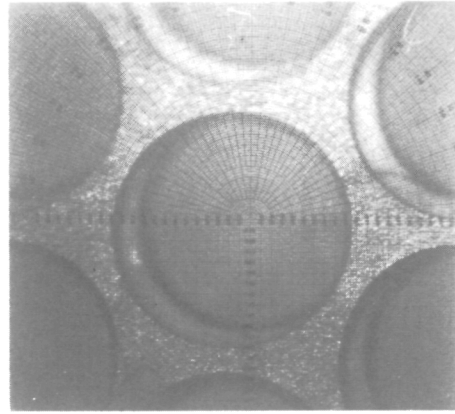
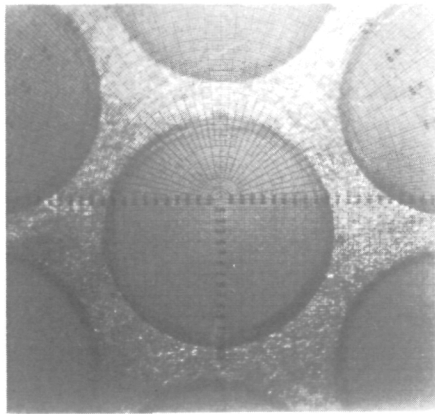
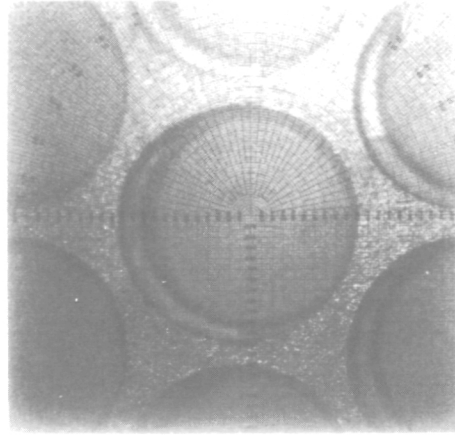
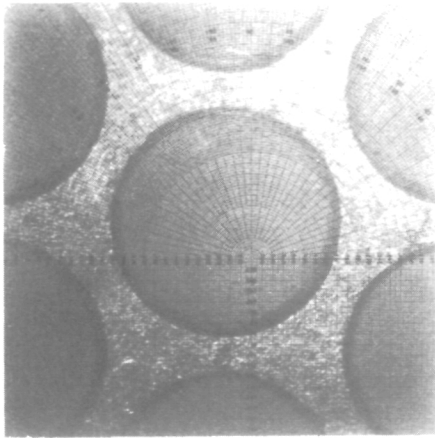


Figure 9. Results of removing short circuit with 500 V grid clearing circuit.

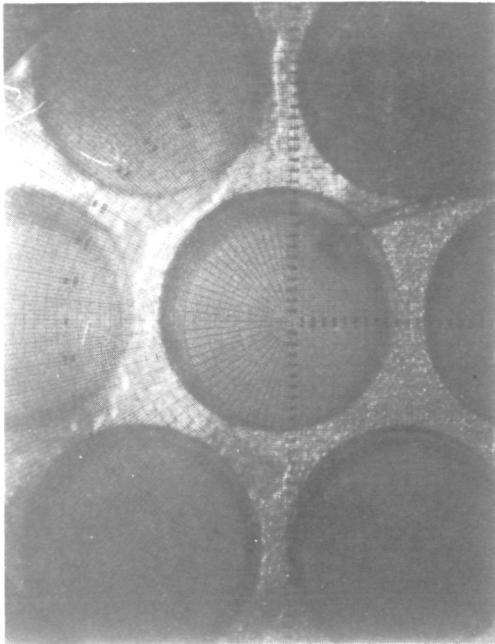


ACCEL, AFTER SHORT REMOVED

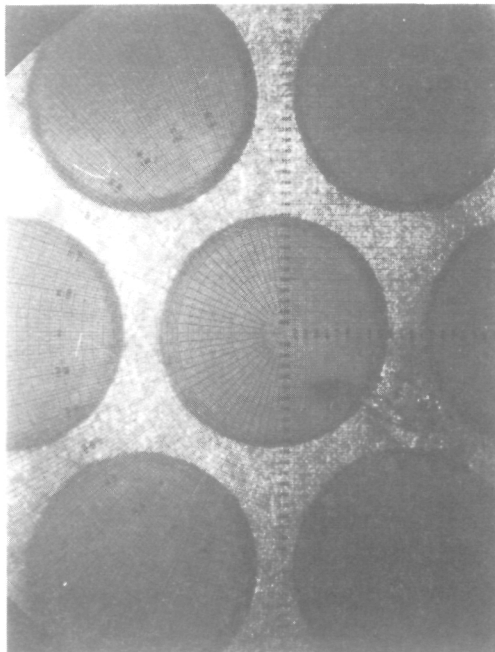
SCREEN, AFTER SHORT REMOVED

Figure 10. Appearance of electrode apertures after short removal in vacuum (0.005 in. Ta wire).

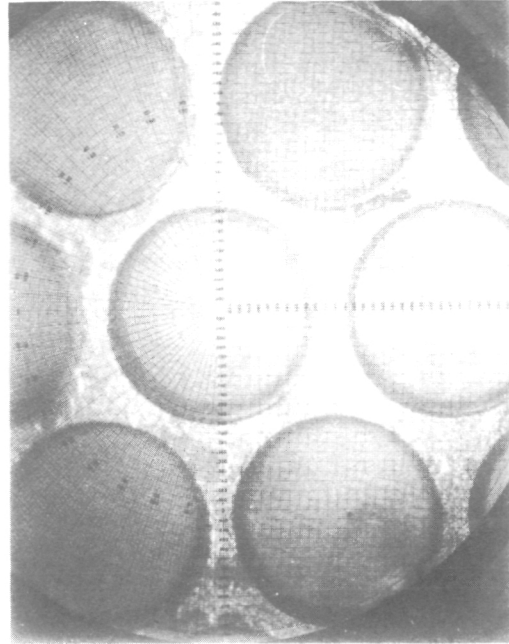




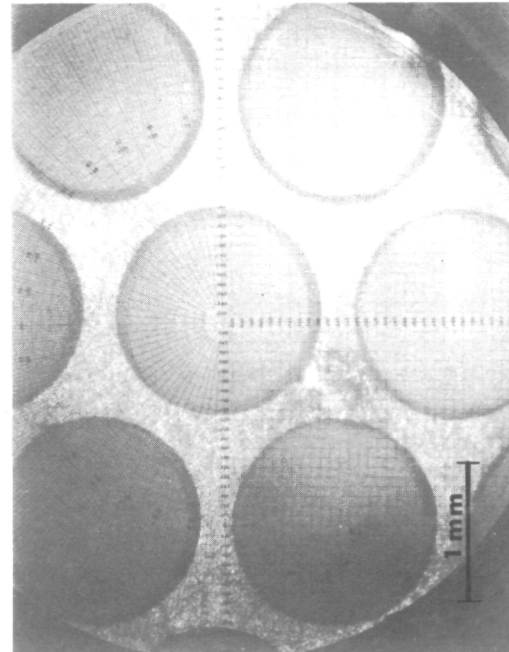
SCREEN, GRIDS SHORTED



ACCEL, GRIDS SHORTED



SCREEN, AFTER SHORT REMOVED



ACCEL, AFTER SHORT REMOVED

Figure 11. Comparison of electrode aperture before and after removal of 0.005 in. diameter spotwelded shorting wire.

caused by the spotweld. In any case, such damage would not reduce lifetime unless grid clearing became necessary too frequently.

The final documentation of the 500 V, 4  $\mu$ f circuit is for the removal of a 0.05 mm (0.002 in.) diameter Ta wire both in air and in vacuum (as shown in Figure 12). When removed in air (upper four photographs), the shorting wire is removed completely; in vacuum (lower four photographs), the wire is severed near one spotweld and pushed away toward the other electrode. This is not satisfactory short removal, since the ion extraction voltages could probably not be applied to the electrodes without breakdown.

Grid clearance capability and the resulting electrode damage was also documented for the screen power supply output filter (as specified for in the EMT power processor). Figure 13 shows the circuit used to represent the power supply. Tests were performed in air as described previously with the shorting wire placed in simple contact with the electrodes. The results are shown in Figure 14; it is apparent that the shorting elements were removed without causing damage. Examination of the electrodes used in the 10,000 hr test of a 30 cm thruster under contract NAS 3-15523 shows no evidence of damage of the type seen in Figures 9 and 11(a 1  $\mu$ f capacitor was connected between the screen and accel electrodes for the last 4000 hr of testing). The circuit shown in Figure 13 was not capable of removing a 0.13 mm (0.005 in.) diameter Ta wire which had been spot welded in place.

The final experiments performed document the damage to electrodes as the stored energy is increased. The circuit of Figure 6 was used with a 1000 V spark gap and increasing values of  $C_1$  to remove a 0.15 mm (0.006 in.) diameter tantalum wire short. Figure 15 shows the marking of the electrodes after removal of the shorting wires by capacitor discharge. The wires were not spot welded for these tests, and the tests were performed in air. Although there is obvious electrode damage in each case, the material removed should not be a factor in electrode lifetime.

Removing metallic grid shorts by capacitive discharge will not significantly damage the ion optics electrodes at least within the limits



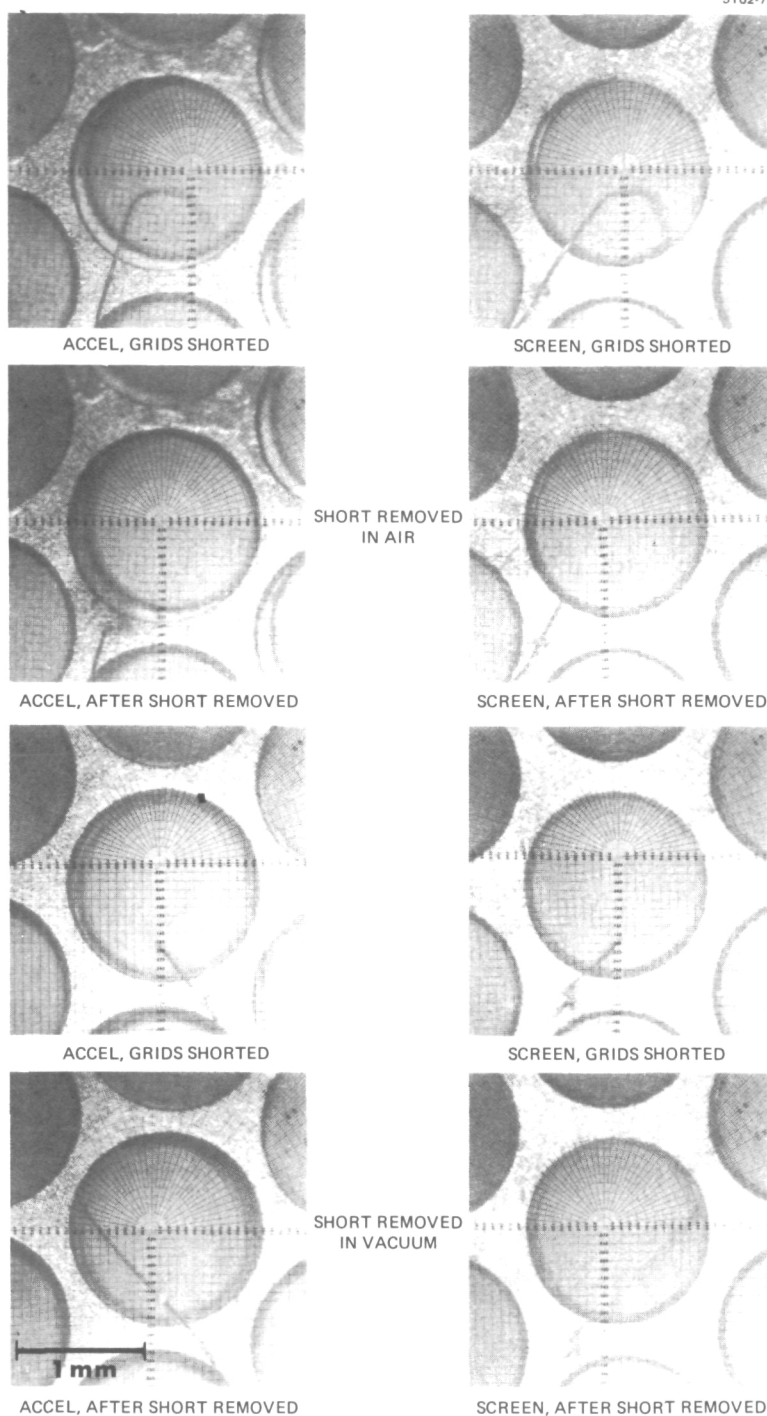


Figure 12. Documentation of removal of 0.002 in. diameter spotwelded Ta shorting wire using 500 V, 4  $\mu$ f circuit in air and in vacuum.

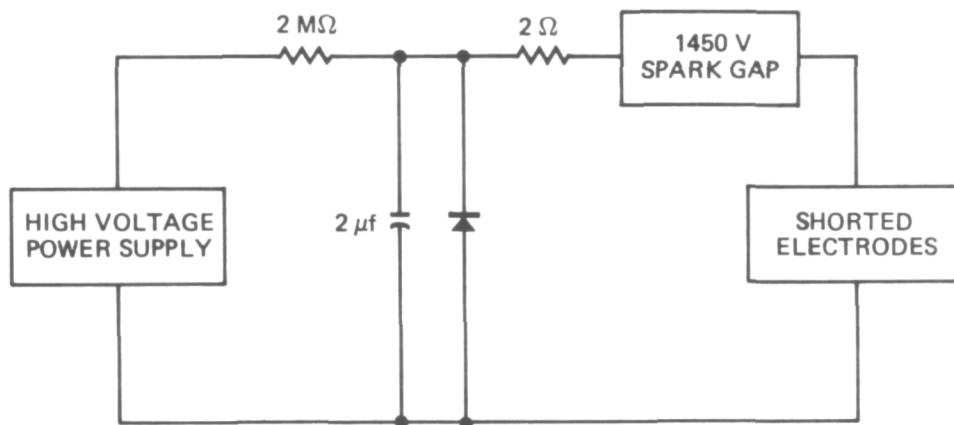


Figure 13. Schematic diagram of circuit to simulate screen supply output.

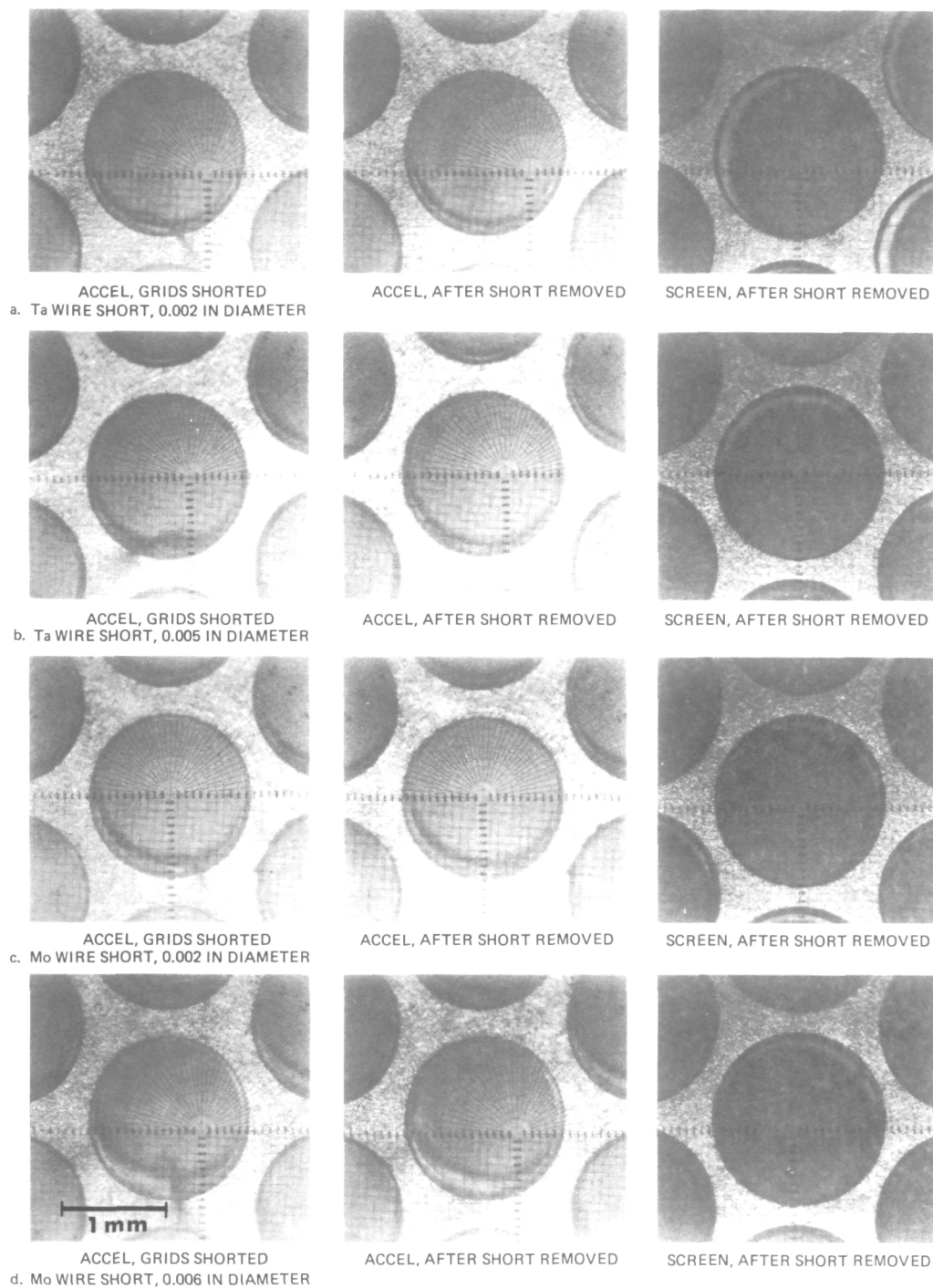


Figure 14. Results of removing short circuit with simulated screen supply output.

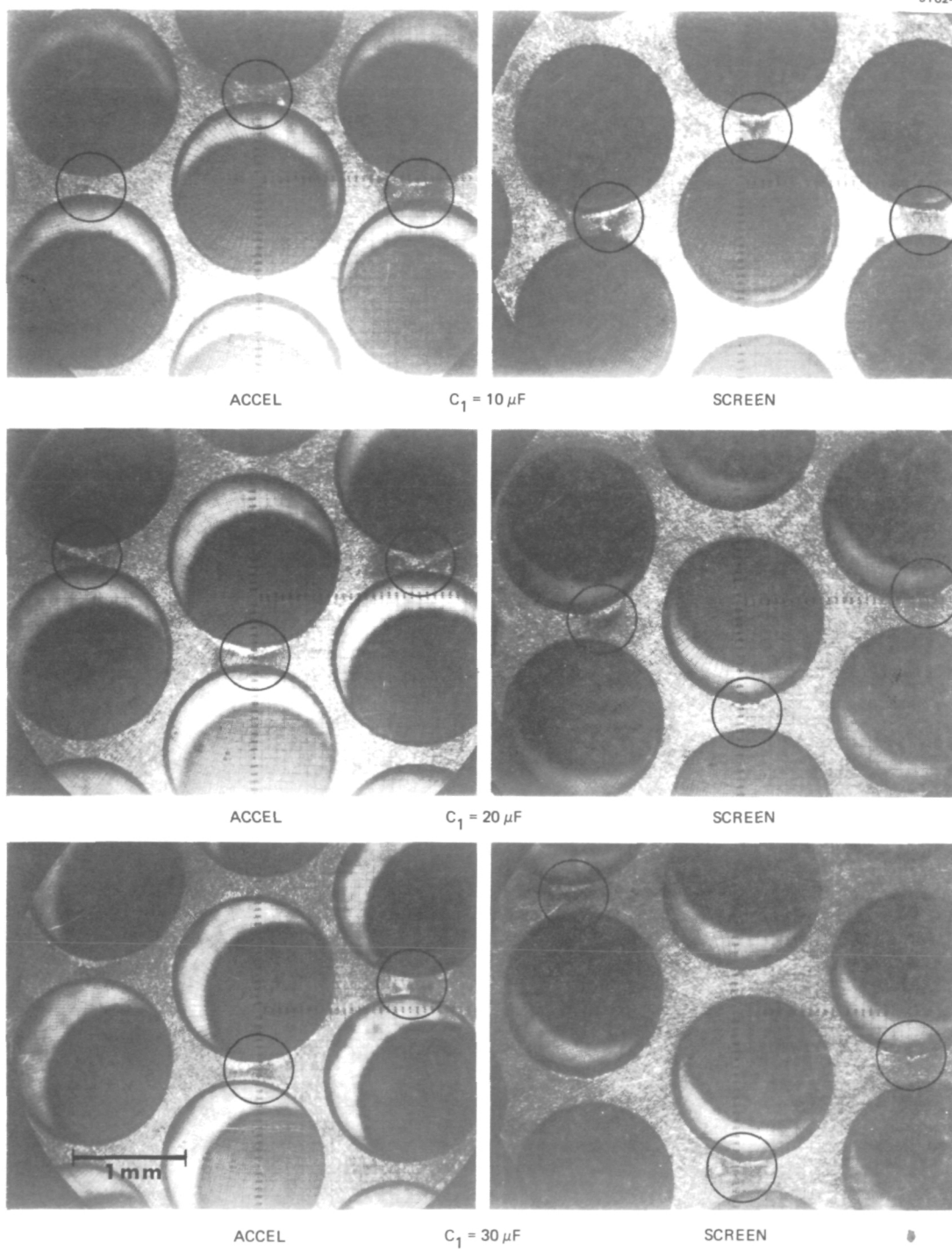


Figure 15. Electrode damage for several values of  $C_1$  at 1000 V discharge.

of the capacitance values and stored energies investigated here. Flakes of grid material up to 0.03 mm (0.001 in.) thick and perhaps 0.25 mm (0.010 in.) wide can be anticipated in thrusters equipped with wire mesh anode liners. Thus, a cross section between that of a 0.05 mm (0.002 in.) and 0.13 mm (0.005 in.) diameter wire is representative of shorts that will be experienced. High current for a short interval appears to be the most effective method for short removal. The 500 V, 4  $\mu$ f capacitor discharge is somewhat marginal both in terms of short removal capability and possible grid damage. On the basis of tests performed here, a capacitor discharge using 2 to 20  $\mu$ f at 1000 V is recommended as the preferred combination of circuit elements. The switching element selected should not require current limitation or slow the current rise time (current limitation should be dominated by the unavoidable wiring inductance). The circuit employing the spark gap that was used in the tests here has also been successfully used (1  $\mu$ f at 1450 V) to clear an optics short which developed during thruster testing at high specific impulse, and this procedure can thereby be recommended without reservation.

#### B. Doubly Charged Ion Investigation

This section describes work begun under the previous contract (NAS 3-17831) to evaluate multiple-ion production and to identify ways of reducing double ion concentrations. The detrimental affects of the doubly charged ion current are manifested in two ways:

- By eroding discharge-chamber components, in particular the baffle and screen grid
- By reducing thrust per unit current, which results in lower total efficiency.

The first effect is now considered the most important, although it was the associated reduction in efficiency that originally motivated this investigation. In this section we describe the experimental and theoretical results which led to a more complete understanding of double-ionization phenomena and means of reducing the concentration of doubly charged ions.

## 1. Small-Hole Accel Grids

Parameter mapping under the earlier program showed that variations in small-hole accelerator grid (SHAG) optics alter the content of double ions in the extracted beam more than variations in any other parameter. Thus, we have attempted to evaluate in detail the critical aspects of 30 cm thruster operation with SHAG optics systems. The aspects which will be discussed are (1) the optical properties of small-hole grids, (2) the discharge chamber plasma properties associated with SHAG optics, and (3) tradeoffs between performance and double ions.

In general, an ion optics assembly which uses extremely small accelerator grid apertures is characterized as a reduced perveance system with significant ion trajectory crossover in the accelerating region. These factors must be weighed against any performance gains or reduction in multiply charged ions that are also characteristic of SHAG optics. As such, the optics analysis is performed with overall thruster performance in mind, realizing that under certain conditions operations with small accelerator apertures may not be ideal from the strict optical-quality point of view.

Minimum accelerator aperture diameter is determined by computer trajectory analysis of a single aperture located in the center region of a typical 30 cm dished-grid optics system, where the minimum size is defined as the diameter where ions are just starting to intercept the edge of the accelerator aperture. Throughout the analysis the following parameters are held constant:

- Screen grid aperture diameter,  $d_s = 1.91$  mm
- Screen grid thickness,  $t_s = 0.38$  mm
- Accelerator grid thickness,  $t_A = 0.51$  mm
- Intergrid spacing,  $\ell_g = 0.64$  mm.

The variables, therefore, are

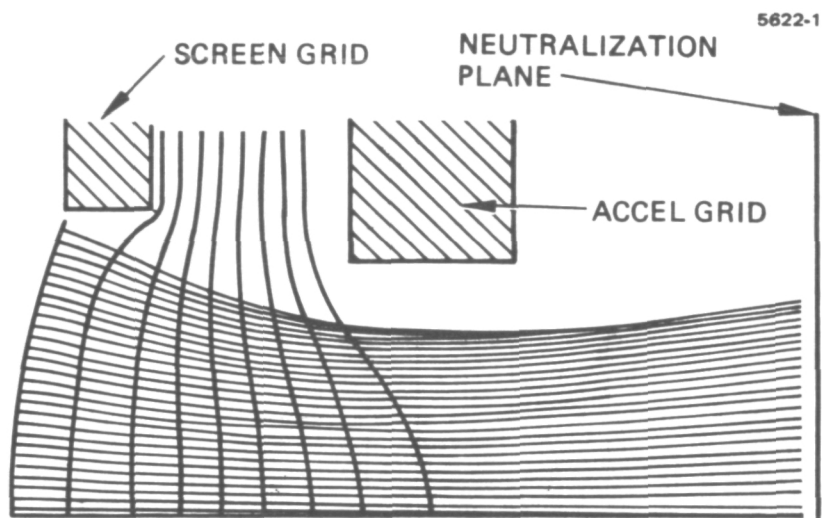
- Ratio of net-to-total voltage,  $R$
- Total voltage,  $V_T$
- Accelerator aperture diameter,  $d_A$ .

Since single-aperture effects are being considered, the current per hole for a thruster operating at a typical 2.0 A beam current must be evaluated. This has been done,<sup>6</sup> with the results shown in Table 1, where a net voltage of 1100 V and an accelerator voltage of -400 V were used to determine the average perveance requirements for each of four constant current density regions. A trajectory analysis for center region apertures can then be done based on these specifications. The results of such an analysis are shown in Figure 16(a). By reducing the accelerator aperture diameter from the EMT specification of 1.52 mm to a smaller diameter of 1.22 mm, the trajectories of Figure 16(b) can be obtained, nearing the point at which direct interception would occur. By using smaller diameter apertures with the same ratio of net-to-total voltage, the perveance increases from 4.5 nanopervs for the EMT optics design to 5.2 nanopervs for the smaller apertures. It is not necessary to readjust the sheath configuration, since the calculated current uniformity remains constant to within  $\pm 5\%$  for both cases. Thus, the EMT optics are not operating at maximum perveance, and the optimal means of increasing this value would be to reduce accelerator aperture diameter to the point of direct interception. However,

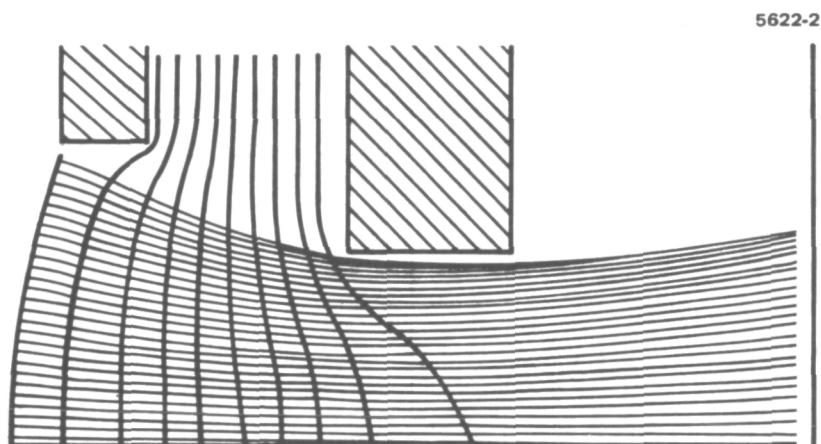
Table 1. Average Current per Hole Characteristics  
for 30 cm Dished Grid at 2 A Beam Current

Region	Normalized Outer Radius	Number of Holes	Average Current per Hole, mA	Average Perveance per Hole, Nanopervs	Total Current, mA
1	0.25	976	0.265	4.56	259
2	0.50	2928	0.220	3.79	644
3	0.75	4880	0.148	2.55	722
4	1.0	6832	0.0548	0.94	374
Note: This data calculated by approximating measured beam profile by four constant current density regions.					

T2091



(a) PERVEANCE = 4.5 nanopervs



(b) PERVEANCE = 5.2 nanopervs

Figure 16. Effect of reduced accelerator aperture diameter on perveance and trajectories for EM optics,  $V_{\text{net}} = 1100$ ,  $V_A = -400$ .



decreasing aperture size further requires increasing total voltage. This relationship is shown in Figure 17, where the minimum accelerator aperture diameter is plotted as a function of total voltage. Along with the curve for center region holes, a curve representative of 3/4 radius holes is also shown. These curves are obtained from trajectory plots at continued lower perveance while simultaneously reducing accelerator aperture diameter to the point of direct interception. The ratio of net-to-total voltage is found not to have a significant effect on minimum aperture size; however, it does alter beam divergence characteristics. The maximum theoretical perveance for center region holes is calculated from Child's Law for a planar diode:

$$\frac{J}{V_T^{3/2}} = \frac{\pi \epsilon_0}{9} \left( \frac{2q}{m} \right)^{1/2} \frac{d_s}{\ell_g} .$$

At this point it is assumed that the accel aperture diameter is equal to the screen aperture diameter and, thus, defines the minimum total voltage at which 2.0 A of beam current can be extracted. This point was also used as a check on the computer analysis and was found to be in good agreement. The typical operating point for the EMT is also shown in Figure 17 for reference.

Two parameters which are not reflected in Figure 17 but which have a significant effect on thruster operation are the electron backstreaming limit and the net-to-total voltage ratio. The backstreaming limit, which is a function of both total voltage and accel aperture size, will be discussed first. The accelerator potential,  $V_A$ , necessary to prevent backstreaming can be estimated by the following relation.<sup>7</sup>

$$V_A = \frac{\exp \frac{t_A}{d_A} d_A V_T}{2\pi \ell_g} \quad (4)$$

This relation is plotted in Figure 18 at the minimum accelerator aperture points, which in turn specify the total voltage requirements. Also

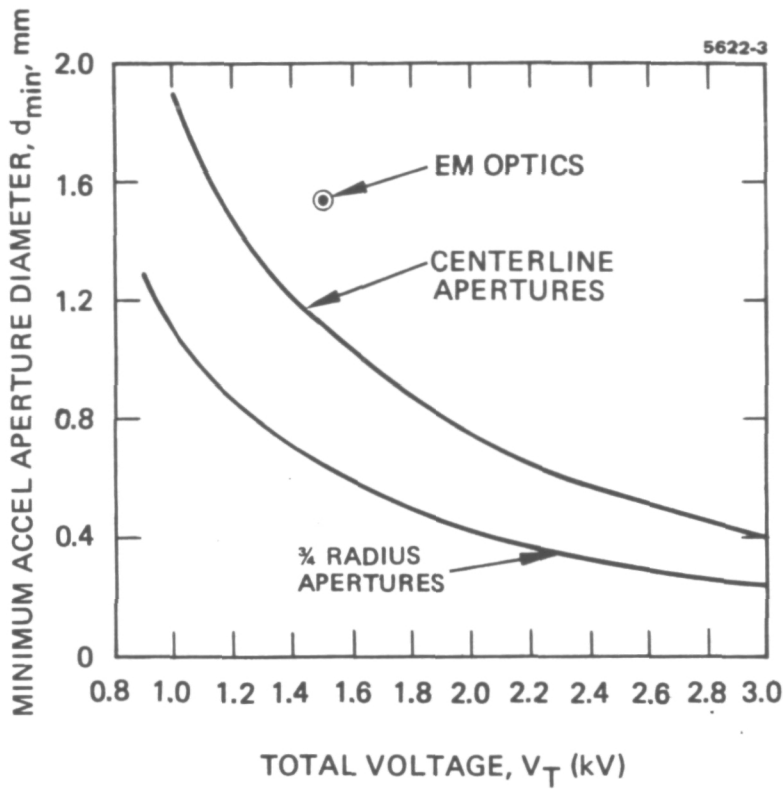
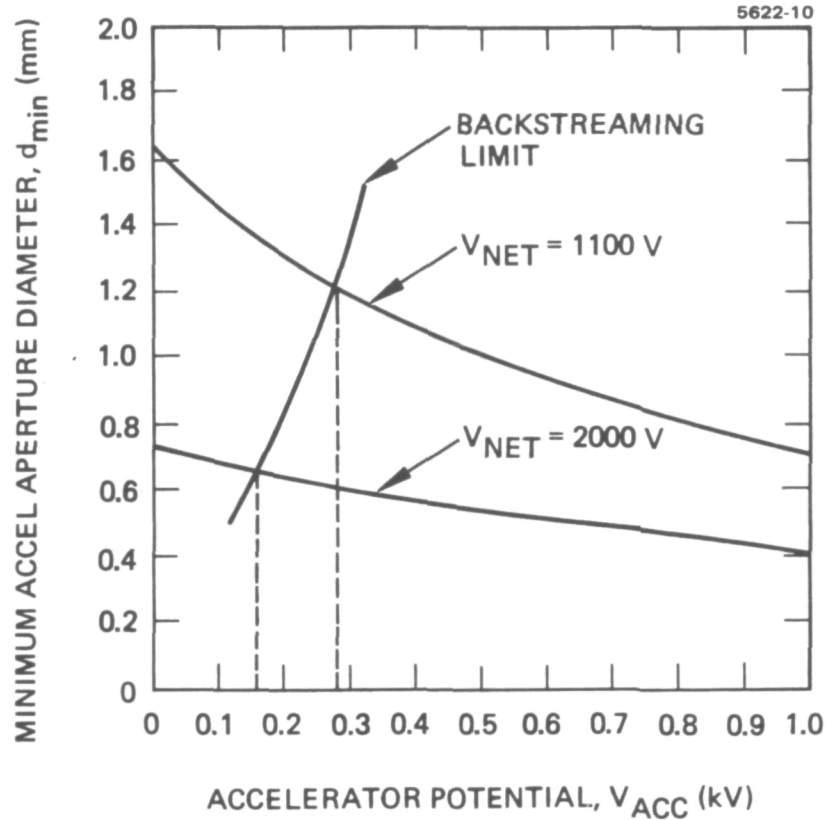


Figure 17.  
Theoretical total voltage requirements necessary to avoid accelerator interception on centerline and at  $3/4$  radius;  $l_g = 0.64$  mm,  $d_s = 1.9$  mm,  $I_B^g = 2.0$  A.

Figure 18.  
Backstreaming limits on thruster centerline for optics operating at minimum accelerator aperture diameter.



shown are two curves which are replots of Figure 17, except the net voltages of 1100 V and 2000 V are specified. Thus, at 1100 V net voltage and an accel aperture of 1.27 mm diameter, approximately -280 V is necessary to prevent both backstreaming and direct interception. At accelerator potentials higher than -280 V, only interception limits aperture size. The curve at 2000 V net voltage demonstrates that SHAG optics would be particularly well suited for high specific impulse operation.

The ratio (R) of net-to-total voltage is also not reflected in the curves of Figure 17, but has a significant effect on optical quality. Because a 30 cm thruster typically operates at 1100 V, this necessarily dictates low R values for very small hole accelerator grids and a resulting increase in beam divergence. However, moderate decreases in aperture size to  $\approx 1.1$  mm diameter should produce no significant change in trajectories, since a high, nearly constant R ratio can be maintained; no change in divergence was noted in the trajectory analysis when the accel aperture was decreased to this value.

To verify the minimum aperture size analysis, two SHAG ion optics sets were assembled with the specifications listed in Table 2. The EMT optics specifications are also shown for reference. Tests were conducted to measure beam dispersion angles and to evaluate thruster performance and double-ion densities. The latter two parameters will be evaluated in a later section and only optical properties will be discussed here. A collimated probe<sup>1</sup> was used to measure divergence angles for the three optics sets at various locations on the thruster's radius. Because of the probe location and small acceptance angle of the probe, the dispersion curves should be representative of an individual aperture. Table 3 lists full-width-half-maximum (FWHM) angles for the three optics sets operated at various accel-decel ratios. These angles are shown for centerline and for 3/4 radius holes. The overall thrust factor for beam divergence loss, which is obtained by integration over the thruster radius, is also shown. For both sets of SHAG optics, the total voltage necessary to reduce accelerator current to a minimum level was found to be within  $\pm 5\%$  of the value predicted by the trajectory analysis. The beam dispersion angles are degraded, as anticipated, when smaller accelerator apertures are used. The data of Table 3 and

Table 2. Optics Specifications

Optics	Screen Aperture Diameter, mm	Accel Aperture Diameter, mm	Grid Spacing, mm	Screen Compensation, % Reduction	Accel Open Area Fraction, %
EMT	1.91	1.52	0.63 to 0.68	0.4	43
SHAG 1	1.91	1.09	0.38 to 0.56	0.4	23
SHAG 2	1.91	0.69	0.51 to 0.66	0.4	9

T2092

Table 3. Beam Dispersion Data

Optics	$V_{NET}$ , V	$V_{ace}$ , V	FWHM (degrees)		R	$F_T$
			$C_L$	3/4 R		
EMT	1100	300	10	10	0.786	0.983
EMT	1100	400	11	12	0.733	0.982
EMT	1100	500	12	13.5	0.688	0.981
SHAG 1	1300	400	11	11	0.765	0.982
SHAG 1	1100	550	14.5	17	0.666	0.979
SHAG 1	1100	600	16	19.5	0.647	0.977
SHAG 2	1200	500	16	22	0.71	0.976
SHAG 2	1250	800	25	22	0.61	0.970

T2093

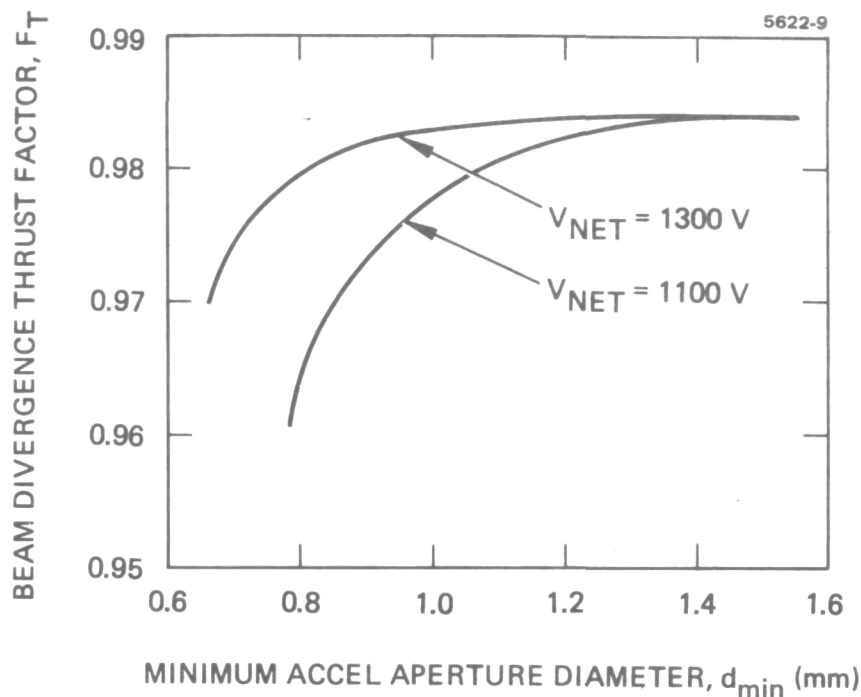


Figure 19. Beam divergence thrust loss for operation at minimum accelerator aperture diameter.

the curves of Figure 17 can be used to estimate the total thrust loss due to beam divergence for SHAG optics systems operating at various net voltages. This is shown in Figure 19, where thrust factor for beam divergence is plotted as a function of minimum accelerator aperture diameter. Beam divergence tends to increase rapidly at very small aperture diameters, particularly at low specific impulse. However, moderate reduction of aperture size to approximately 1.1 mm, as mentioned previously, would be effective in reducing neutral propellant loss without a significant increase in beam divergence.

Thicker accelerator grids might also provide an additional reduction of neutral propellant without affecting either beam trajectories or perveance.<sup>8</sup> However, previous investigations<sup>9</sup> have shown no change in thruster performance when the accelerator grid thickness was increased from 0.51 mm to 0.76 mm. It is also extremely difficult to manufacture an accelerator grid thicker than 0.76 mm with present chemical milling techniques. Thus, it appears that further increasing accelerator grid thickness for a specified aperture size may not be a viable technique for reducing propellant loss.

Because the intent of operating with small-hole accelerator grids is to reduce doubly charged ion densities, a survey of the plasma properties and potential distributions within the discharge chamber was conducted. These properties can then be used as input parameters to double ion production models,<sup>10</sup> thus indicating the effect various thruster operating conditions have on double ionization. Because this was the first time a Langmuir probe survey was taken of a 30 cm thruster, EMT optics and SHAG 1 optics were used in the mappings. The computer technique for analysis of the probe data is described in Ref. 1. The 20 discharge-chamber locations used in the mapping procedure were felt to be sufficient to provide an adequate number of points for averaging and for distribution plotting. Table 4 summarizes the volume averaged plasma properties obtained with EMT and SHAG 1 optics sets at the operating conditions indicated. The plasma properties and distribution appear to be consistent with those of other ion thrusters for which similar data is available.<sup>11</sup> The main difference between operation with the two optics sets is the lower primary electron energy and lower plasma potential which can be achieved with the use of SHAG optics. This is because stable and efficient operation can be achieved at 30 V discharge voltage rather than 37 V. Also, the primary electron energy of approximately 20 V is within 1.5 V of the threshold energy for double ionization of the single-ion ground state.

It was noted during the probing investigation that a low point in plasma potential existed immediately downstream of the baffle and that the potential appeared to rise by several volts in both the axial and radial directions from this point. This was true for both optics sets and at all operating set points used in the tests. Further analysis was done by constructing approximate equipotential lines throughout the discharge chamber based on the Langmuir probe data. The results are shown in Figure 20 for EMT optics operated at 2.0 A beam current. The shape of the equipotential lines did not change significantly with the substitution of SHAG optics, and such a potential distribution suggests that a significant number of ions formed in the primary electron region would never be extracted by the optics system. Instead, they

Table 4. Volume Averaged Plasma Properties for EMT and SHAG 1 Optics. Langmuir probe data is presented in tabular form in Appendix A.

Optics	EMT	EMT	EMT	SHAG 1	SHAG 1
Beam current, A	2.0	1.5	1.0	2.0	1.5
Discharge voltage, V	37.0	37.0	37.0	30.0	30.0
Discharge current, A	10.0	7.5	5.0	11.7	9.5
Maxwellian electron temperature, eV	3.8	3.6	3.3	2.9	3.0
Primary-to-Maxwellian electron density ratio	0.25	0.35	0.50	0.22	0.19
Primary electron energy, eV	27.2	25.5	25.4	19.7	19.6
Electron density, $10^{-10} \text{ cm}^{-3}$	16.4	9.0	7.5	12.8	8.3
Plasma potential, V	36.4	33.8	33.1	22	20.5

T2094

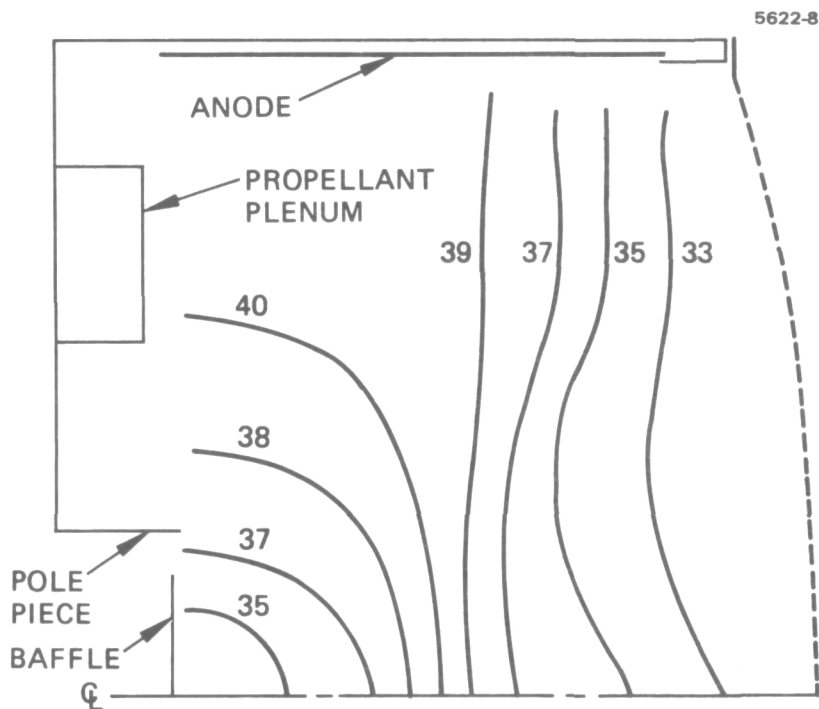


Figure 20. Schematic of 30 cm thruster showing approximate equipotential lines;  $V_{DIS} = 37 \text{ V}$ , EMT at 2 A beam current.

would be focused toward the baffle and polepiece assembly, causing localized erosion. To verify this conjecture, a computer simulation of the potential field was made, and ions were started at arbitrary locations throughout this field. The simulated region of interest is shown in Figure 21, along with the potential lines and ion trajectories. The ions are, in fact, focused toward the baffle and polepiece, apparently not impinging on the backplate or propellant plenum of the thruster. Since the highest plasma density is on the thruster centerline, this suggests a high erosion rate in the center region of the baffle. This modeling seems to be confirmed by the erosion noted in the 10,000 hr lifetest of a 30 cm thruster,<sup>2</sup> where the center of the baffle was totally eroded after approximately 6000 hr of operation at 1.5 A beam current. This lifetest thruster also showed no erosion of the backplate or the rear half of the cathode polepiece, and thus the model appears to be consistent with experimental results.

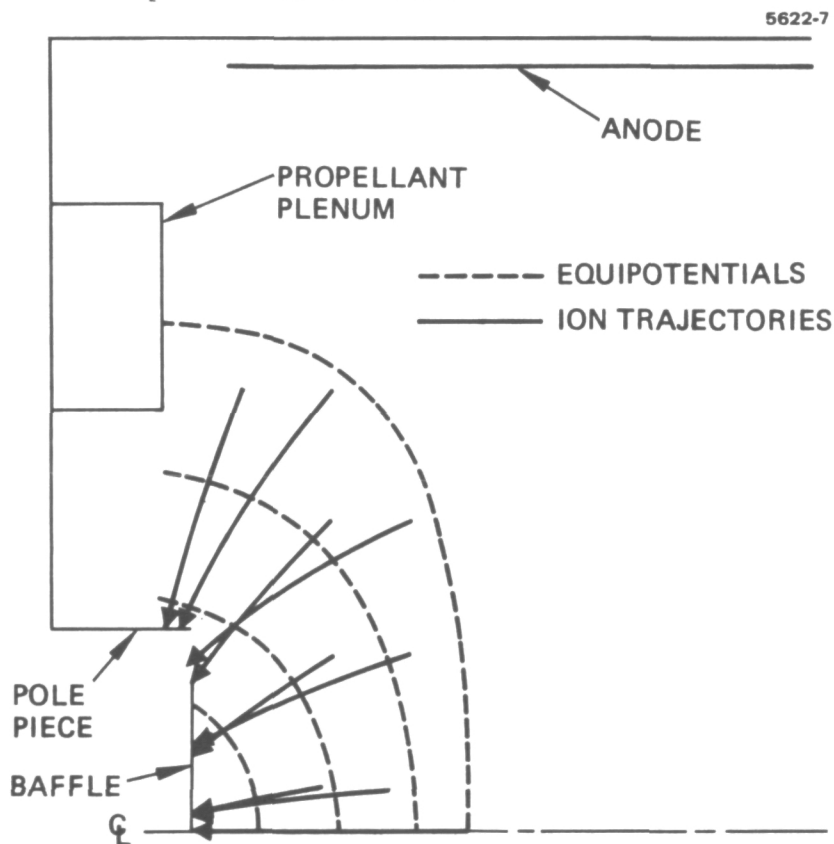


Figure 21. Simulation of upstream potential distribution showing calculated ion trajectories.



It is not obvious what changes in the thruster configuration might be made to alter this potential distribution and reduce the focusing effects.

## 2. Discharge Parameters

Results at NASA Lewis Research Center have indicated that a reduction in baffle erosion could be obtained by modifying the baffle support structure. The modification consisted of incorporating into the "800 series" baffle support the "400 series" dimensions for  $D$ ,  $D_2$ ,  $D_3$ ,  $W_1$ , and  $W_2$ , as shown in Figure 22. Data was taken with the collimated mass spectrometer beam probe in an effort to evaluate double-ion production with the various baffle support structures. Because the scatter in the data was as large as the differences observed, no clear effect of the baffle support could be defined. However, erosion badge monitors showed a reduction in erosion when the "700 series" baffle support was modified to incorporate the "400 series" dimensions. Consideration of the plasma potential distribution shows that this is not necessarily inconsistent, since changes in the double-ion production rate in the vicinity of the cathode polepiece are probably not reflected in beam measurements.

Another alternative for reducing the erosion rate of cathode surfaces (in particular of the cathode polepiece, baffle, and screen grid) is to bias these surfaces positive with respect to the cathode. This can be accomplished by using a longer cathode tube and inserting an insulating spacer between the cathode and the propellant tube flanges. Because the keeper potential is usually 4 to 5 V, this voltage was considered to be a reasonable point at which to bias the thruster shell without suffering a significant power loss. The thruster was operated with SHAG 2 optics at a discharge voltage of 32 V and a keeper potential of 4 V. Operation appeared stable and beam probe scans showed a reduction in double-ion content from 10.5 to 7.5%. However, this reduction was accompanied by a 1 to 2% loss in corrected mass efficiency. But because of the 4 V bias potential, the ion energy (arriving at the walls) was reduced by this amount; this reduction may have a moderate effect on reducing the sputter erosion rates.

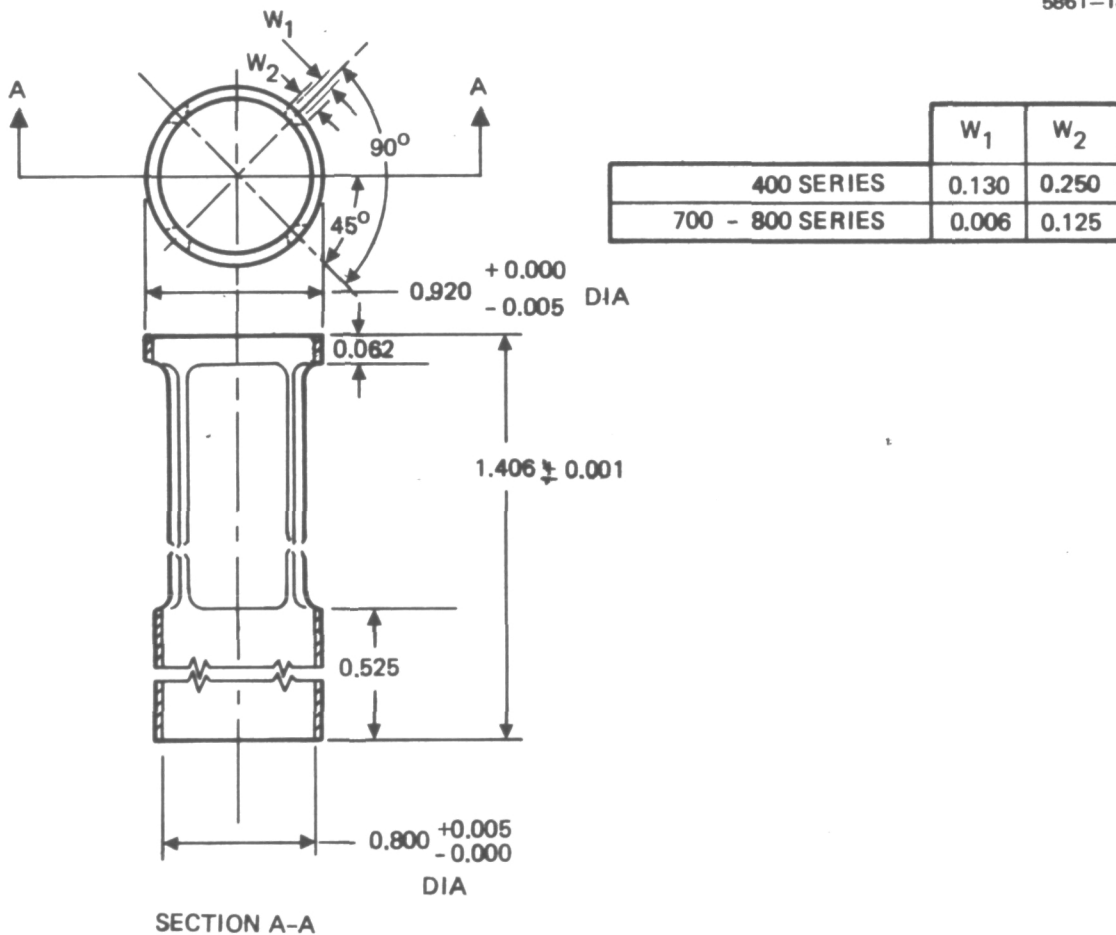
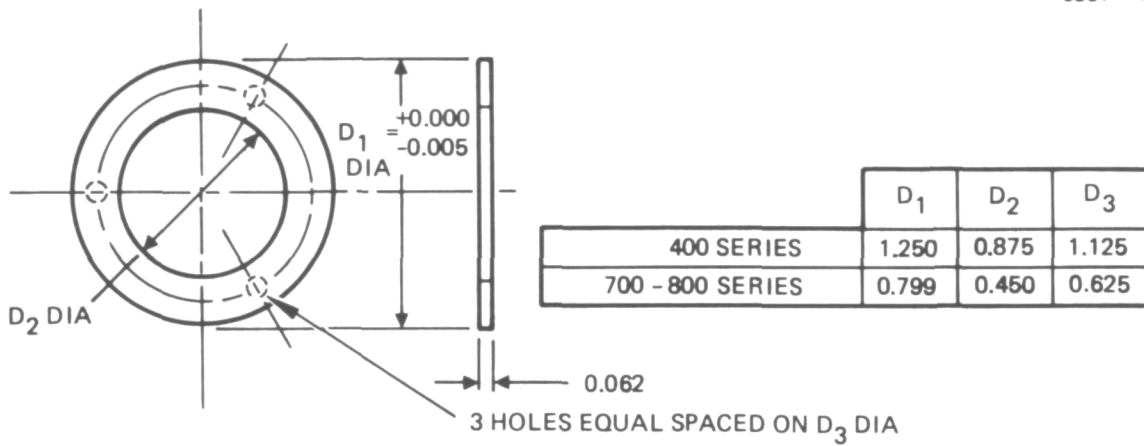


Figure 22. Dimensions of 400 series and 700 to 900 series baffle support.

### 3. Performance and Double-Ion Production

Knowing the discharge chamber plasma properties of EMT and SHAG optics systems, it is now possible to evaluate double-ion production rates for various thruster configurations and operating points. Since small-hole accelerator grids appear to be a possibility for 30 cm thruster operation, the relationship between parameters such as accelerator grid open area fraction, discharge voltage, and mass utilization are reviewed. The following analysis is done, based on a number of simplifying assumptions, to determine the qualitative effect of these parameters on double-ion production. The assumptions which are made include the following:

- Doubly charged ions are generated by electron bombardment of the single-ion ground state
- The ratio of production rates for single and double ions is a good indication of the double-to-single ion ratio in the beam
- Only singly charged ions generated from the atomic ground state will be considered.

With these assumptions, the following relationships hold:

$$\dot{n}^{++} = n^+ \left[ \begin{array}{cc} ++ & ++ \\ \sum_p n_p & + \sum_m n_m \\ + & + \end{array} \right] \quad (5)$$

$$\dot{n}^+ = n_o \left[ \begin{array}{cc} + & + \\ \sum_p n_p & + \sum_m n_m \\ o & o \end{array} \right] \quad (6)$$

$$- n^+ \left[ \begin{array}{cc} ++ & ++ \\ \sum_p n_p & + \sum_m n_m \\ + & + \end{array} \right]$$

where  $\dot{n}^{++}$  is the production rate for doubly charged ions;  $\dot{n}^+$  is the production rate for singly charged ions;  $\Sigma_p$  and  $\Sigma_m$  are the electron-velocity — cross-section products for primary and Maxwellian electrons;<sup>12</sup> and  $n_o$ ,  $n_p$ , and  $n_m$  are the neutral particle, primary electron, and Maxwellian electron densities, respectively. By taking the ratio of these equations and noting that

$$n_o \geq \frac{4 I_o}{ev_o A_A} \quad (7)$$

$$n^+ = \frac{I^+}{ev^+ A_S} \quad (8)$$

$$\frac{I_o}{I^+} = \frac{1 - \eta_m^+}{\eta_m^+} \quad (9)$$

$$v^+ = \sqrt{\frac{q T_e}{m} \left( 1 + \frac{n_p}{n_m} \right)} \quad , \quad (10)$$

where  $A_A$  and  $A_S$  are the effective open areas of the accelerator and screen grids, respectively, and  $\eta_m^+$  is approximately equal to the corrected mass efficiency,  $\eta_{mc}$ , it is possible to arrive at the following relationship for the average double-to-single ion current ratio:

$$\frac{I^{++}}{I^+} = \frac{0.707}{\left( \frac{1 - \eta_{mc}}{\eta_{mc}} \right) \left( \frac{v^+}{v_o} \right) \left( \frac{A_S}{A_A} \right) \left[ \frac{\Sigma_o^+ n_p + \Sigma_o^+ n_m}{\Sigma_{+p}^{++} n_p + \Sigma_{+m}^{++} n_m} \right]} - 1 \quad , \quad (11)$$

where  $v^+/v_0$  is the ion-to-neutral velocity ratio. Thus, the double-ion ratio appears as a function of several other ratios, some of which can be manipulated to achieve a lower double ion density. Several cross-plots of Eq. (11) are made utilizing pertinent data obtained from the Langmuir probe experiments. Figure 23 shows the effect of the accel-to-screen open area ratio on the doubly charged ion content in the mass efficiency range of interest. The electron energy and temperature are held constant to average values representative of EMT and SHAG optics. Considerable reduction in the doubly charged ion content can be achieved by lowering this ratio, assuming that the mass efficiency can be maintained. Because SHAG optics are a relatively lower perveance system, not only is the accelerator open area lower, but the effective screen area is simultaneously increased because of the increased sheath area. A more comprehensive plot of Eq. (11) is shown in Figure 24; it includes the effect of discharge voltage. For low accelerator transmission, the discharge voltage has little effect on the double-ion ratio for a given mass efficiency. However, mass efficiency is also a function of discharge voltage and, as such, a reduction in discharge voltage will require an increase in discharge current and/or beam current to maintain constant mass utilization efficiency.

Thruster performance was evaluated for the three optics sets listed previously, including double-ion scans utilizing a mass spectrometer probe.<sup>1</sup> The results are shown in Figure 25 where the data is plotted analogous to Figure 24. The agreement between the experimental and theoretical curves is good considering the assumptions which were made. The performance gains which can be realized over EMT optics with the use of small accelerator holes are evident with the SHAG 2 optics set. At 2.0 A beam current, a reduction of 50% in doubly charged ions can be achieved with a simultaneous increase in propellant utilization from 88 to 92%.

The results of this study can best be summarized by listing the advantages and disadvantages of small-hole accelerator grid ion optical systems for a 30 cm thruster. The principal advantages are as follows:

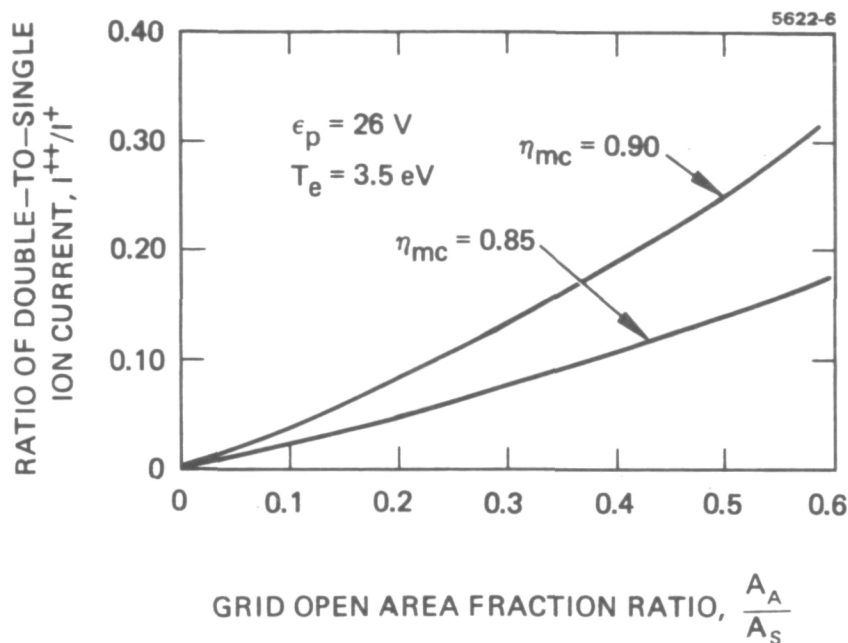


Figure 23. Effect of grid open area on double ion content.

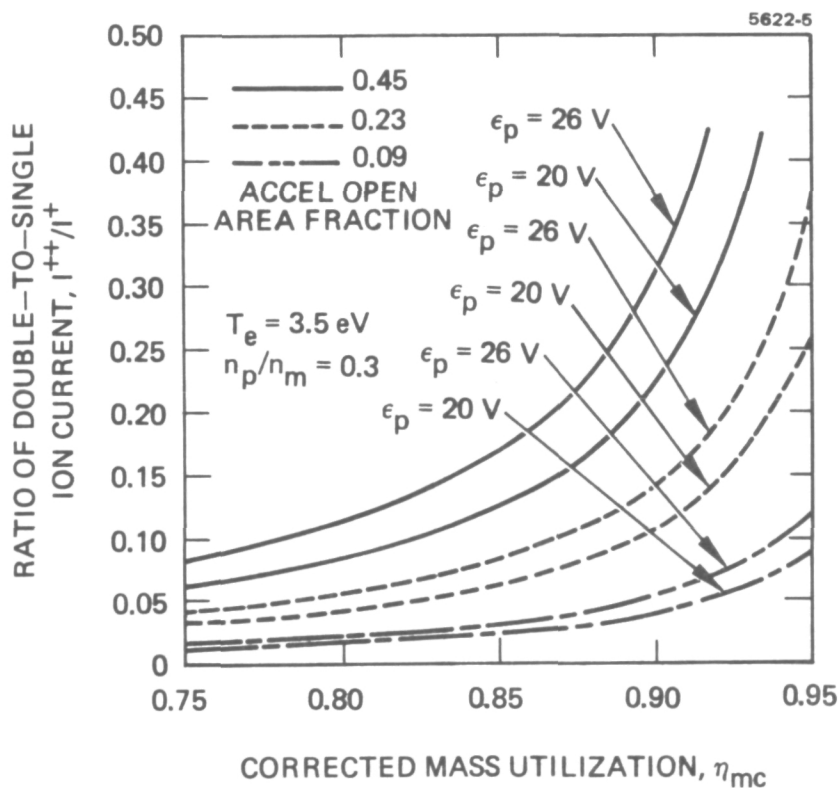


Figure 24. Theoretical double ion ratios utilizing parameters representative of EM, SHAG 1 and SHAG 2 optics.

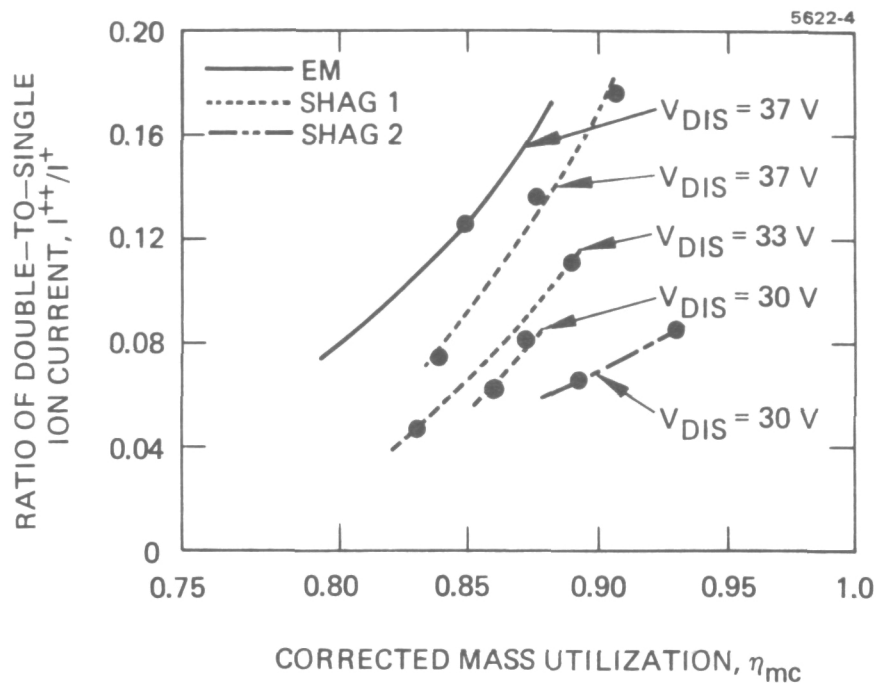


Figure 25. Double ion ratios for EM, SHAG 1 and SHAG 2 optics.

- Low double-ion ratios can be achieved at thruster design efficiencies
- Sputtering energy is reduced because efficient operation can be maintained at low plasma potential
- The increased web thickness allows more area for charge exchange erosion
- Because of beam size and backstreaming limits, SHAG optics would be well suited for high-specific-impulse operation
- The larger sheath area of SHAG optics helps reduce screen grid erosion.

The disadvantages are:

- SHAG optics systems have lower perveance if very small apertures are used
- At low specific impulse, beam divergence increases significantly for very small apertures

- A low open-area fraction results in more thermal distortion of the accelerator grid
- At low specific impulse, SHAG optics requires higher accelerator potential, thus increasing charge-exchange energy.

Thus, there are several tradeoffs which must be examined in detail if SHAG optics systems are to be considered for long-term thruster operation. Performance tradeoffs with respect to thruster efficiency and beam divergence can be readily evaluated; however, prime consideration should be given to erosion rates of various thruster components, namely, the screen and the accelerator grids. This requires accurate modeling and measurement techniques, and a complete erosion evaluation would be necessary before any long-term testing with SHAG optics could be recommended.

#### C. Improved Cathode Reliability

Thirty centimeter mercury ion thrusters currently employ hollow cathodes of the type shown in Figure 26 to fulfill both the main discharge and neutralizer cathode functions. These cathodes supply electron currents ranging from 0.1 to 10 A of continuous emission at relatively low operating temperatures (800 to 1100°C). Mercury vapor is supplied to the hollow cathode as shown at a rate sufficient to maintain internal pressure in the 0.5 to 5 Torr pressure range. To ignite the cathode, heater current is applied to raise the tip temperature to about 800°C; this causes thermionic electron emission from the low-work-function (R-500) coated foil insert. The electrons are accelerated toward the keeper, which is biased at 1000 V but collide with and ionize the mercury gas along the way. The keeper current increases rapidly and its voltage drops to about 10 V at 10 A. An intense plasma plume is observed at the cathode orifice. In this steady-state mode, no heater current is required and the cathode temperature is about 800°C.

The objective of this task was to reduce or eliminate those potential failure modes in the present hollow-cathode design which are attributable to the low work-function emissive mix and the heater. In



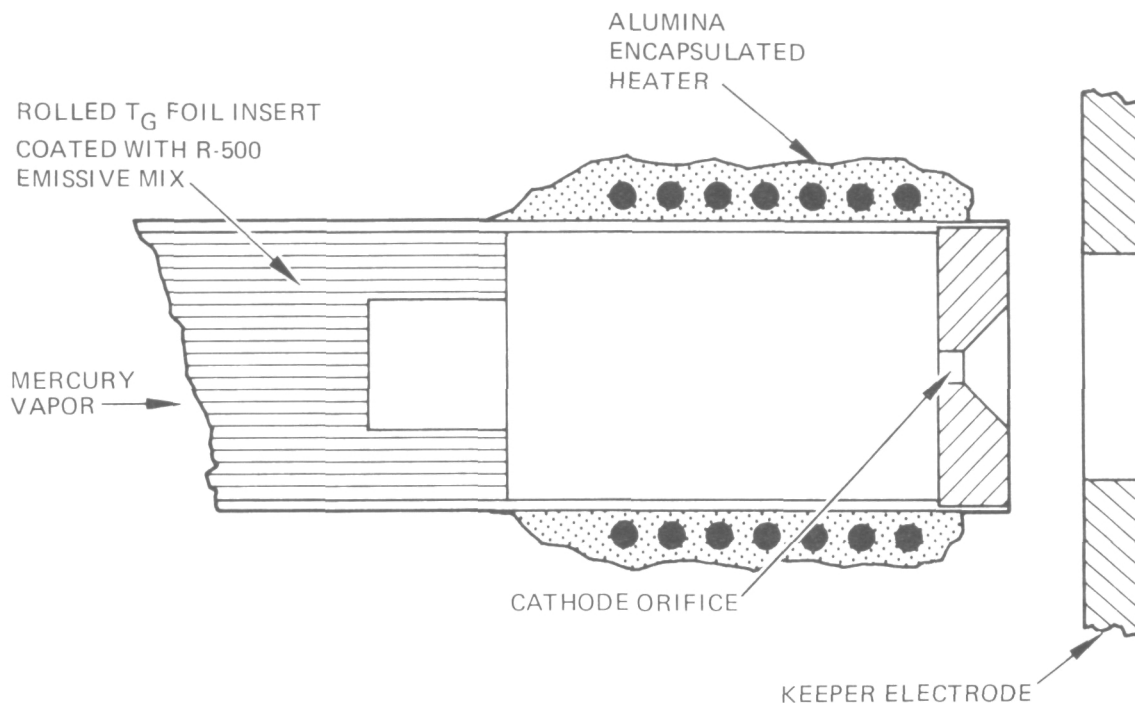


Figure 26. Hollow cathode configuration representative of 700 series 30 cm thruster technology.

present cathode operation, both are required for cathode startup and the emissive mix is required for steady-state operation. Experiments have shown that when the emissive mix is depleted, cathodes are difficult to ignite and operate at undesirable elevated keeper voltage. Failure of the emissive mix could be caused either by chemical contamination or mechanical separation from the tantalum foil. Heater failure modes include the usual open circuit of the heater wire and leakage across a short circuit of the insulation. The specific goals of this task were to find a new hollow-cathode design in which the cathode heater, the low-work-function material (e.g., foil insert), or both can be eliminated.

A new mercury hollow cathode that meets these goals was in fact found based on the work of Lidsky.<sup>13</sup> He showed that a simple, straight tube with neither a heater nor low-work-function material could exhibit hollow cathode action on  $H_2$ , He, Ar, and  $N_2$  gases. The

version of this type of cathode and rf igniter that was built for thruster operation is shown in Figure 27. The cathode tube was formed from 0.01 mm (0.5 mil) Ta foil that was wrapped on a 0.318 cm (0.125 in.) diameter mandrel and spot welded to form the seam. The igniter consisted of Tesla coil components as they exist before the potting steps during normal assembly. The high-voltage secondary LC circuit components were mounted in the vacuum enclosure near the cathode after several attempts to couple the rf output through the vacuum wall were unsuccessful.

A significant part of attaining successful cathode operation (i.e., startup and steady-state operation) was associated with the anode supply circuitry. Figure 28 shows the final circuit that was used for a bell-jar life test of the new cathode and for operation in a thruster. This circuit is similar to the present two-stage keeper type of power supply. To ignite the cathode, the full 500 V is applied to the anode or keeper and the vaporizer is set for  $\sim 1$  A of mercury flow. The rf igniter is then pulsed to initiate a high-voltage discharge between the cathode and the keeper. This high-voltage discharge serves mainly to heat the cathode (i.e., Ta tube); heating by the rf igniter alone is insufficient for ignition. As the cathode heats, the current increases and the voltage drops until an intense hollow-cathode discharge finally evolves. Actual cathode ignition is rapid (e.g.,  $< 1$  s between the rf pulse and full cathode current).

Continuous operation of the new cylindrical hollow cathode was demonstrated at high current and two flow rates. A high-voltage rf igniter mounted outside the cathode tube demonstrated successful operation both before and after the day-long tests. In the first test, the cathode was operated continuously for 7 hr at 10 A. The keeper electrode was removed for the tests and current was collected on a water-cooled anode located about 12 cm from the cathode orifice. The anode voltage ranged between 17 and 20 V at an average equivalent flow rate of 0.72 A. The cathode tube was inspected during and after operation without removing the cathode by using an optical pyrometer. Tube temperature varied from 1900 to 2200°C and was hottest near the

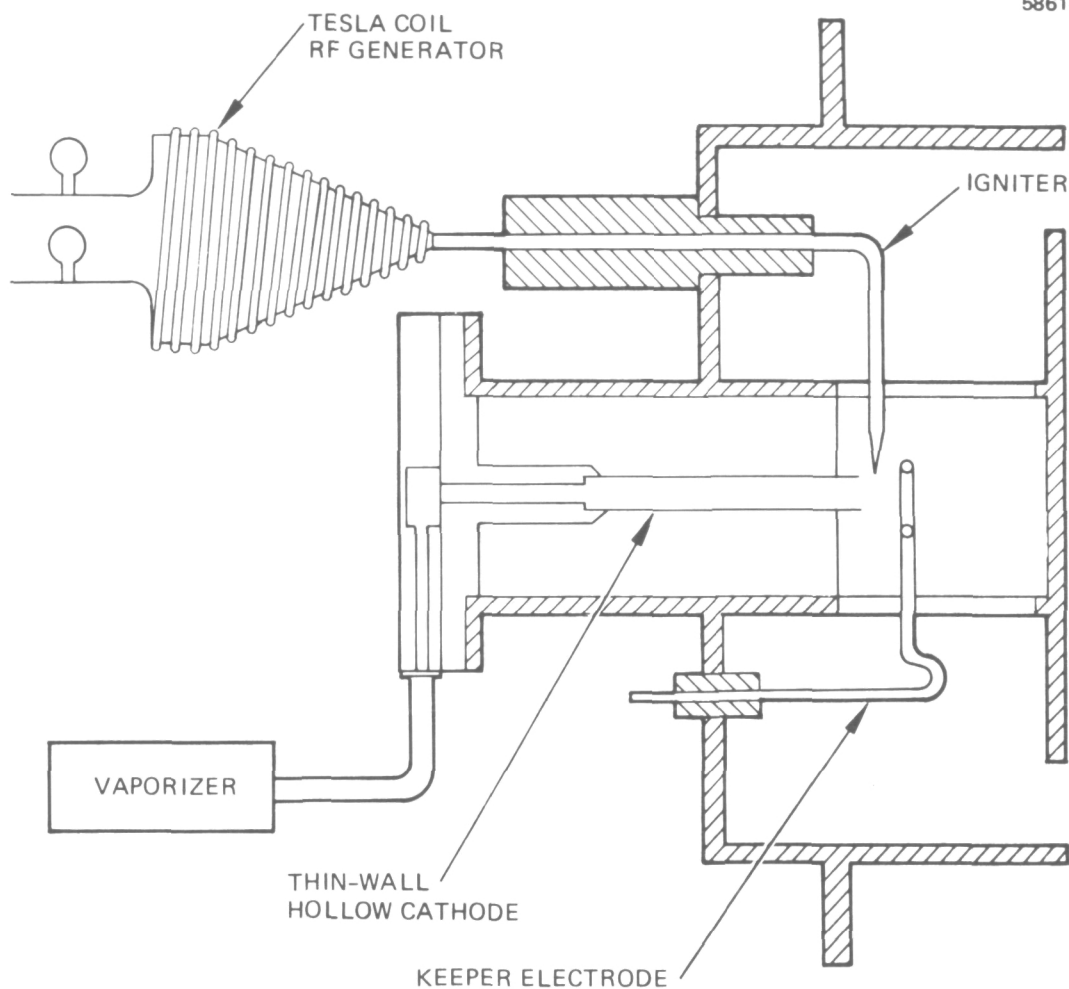


Figure 27. Thin wall hollow cathode/baffle polepiece configuration.

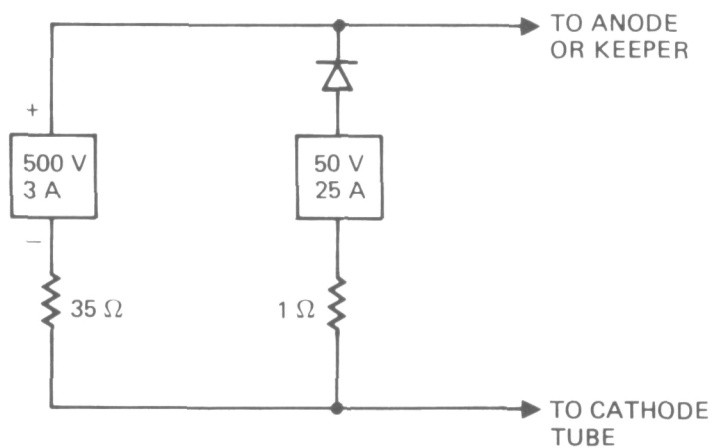


Figure 28.  
Power supply  
schematic for thin-  
wall cathode  
operation.

orifice. No visible erosion of the tube was observed through the pyrometer after either test. In the second test the flow rate was reduced to an average value of 0.43 A (equivalent) and a current of 10 A was maintained continuously for six hours. The anode voltage was slightly higher — 22 V at the reduced flow. From these tests it appeared that testing of a thin-wall hollow cathode in a thruster was feasible.

The new cylindrical hollow cathode and rf igniter that were developed under this task were installed and operated in a thruster representative of the 700 to 800 series design. Figure 27 shows the configuration of the cathode, baffle, and polepiece that was successful in igniting the cathode and discharge. Initially, an attempt was made to ignite the cathode in the thruster using only the igniter and the discharge chamber anode (baffle removed). It was not possible to produce any breakdown without the baffle in place. Using the configuration shown in Figure 27, ignition is readily obtained for cathode flow rates greater than 0.75 A and 300 V applied to the keeper. The keeper discharge ignites at about 100 V and 0.5 A, then transitions to a stable low voltage mode at 15 V and 2 A (power supply characteristics permitting). For keeper currents less than 2 A, the discharge is only marginally stable (thought to be susceptible to mode shifting, and its stability may depend on flow rate and power supply impedance). The coupling between the keeper and discharge and the thruster anode is readily accomplished with the keeper discharge in the low-voltage mode and is self-sustaining if the keeper discharge voltage is then shut off. The discharge operates at essentially constant voltage ( $\sim 45$  V) for discharge currents up to about 5 A, at which point the voltage rises directly with current. Variations in main vaporizer and cathode vaporizer did not produce appreciable changes in this characteristic. It is probable that changes in baffle size or magnetic field strength could alter this characteristic.

Applying beam voltage produced a beam of 0.3 to 0.5 A without difficulty, but propellant utilization was poor, drain currents were high, and the vaporizer flow rates had little control over the beam current. Best operation was at about 0.4 A beam for 0.8 A cathode propellant

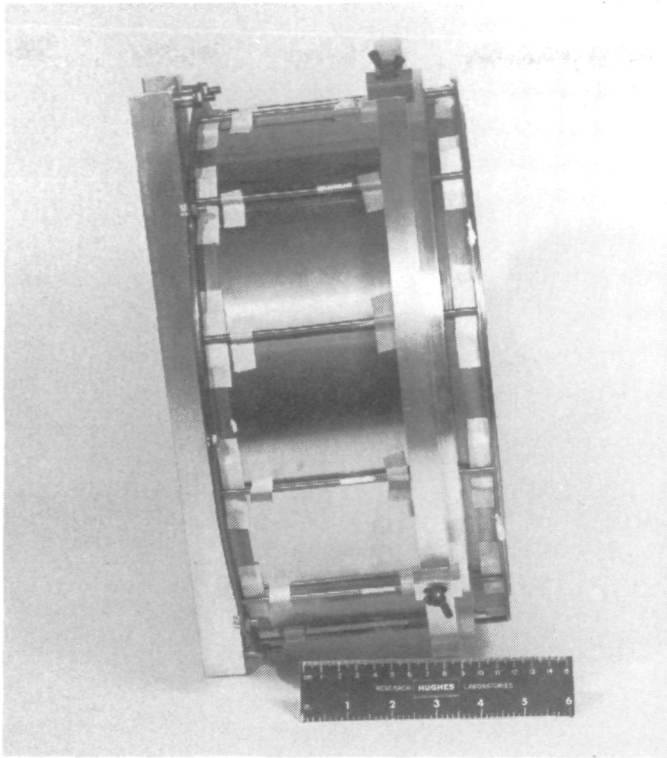
flow rate with no mercury supplied from the main vaporizer. The cathode and discharge were readily re-ignited (several times) after being extinguished, even with the vacuum chamber cold (ambient pressure  $\sim 10^{-6}$  Torr).

Thus, it is concluded that the thin-wall refractory cathode is feasible as an electron source for a mercury thruster. The cathode requires no special treatment and can be ignited without heat or an alkaline earth material being applied externally to lower the surface work function. The cathode — discharge-chamber combination is not efficient in terms of electrical or propellant efficiencies as operated here, but presumably the discharge chamber could be optimized to improve this situation. The discharge chamber control characteristics are also quite different when operated with this cathode and also would need redefinition.

#### D. Magnetic Circuit Design

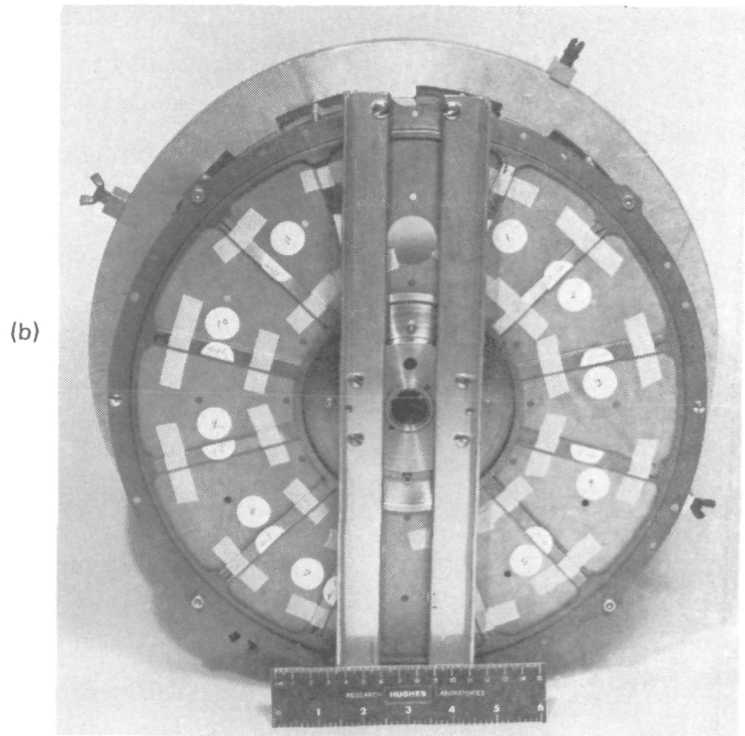
The objective of this project was to develop design criteria for the magnetic circuit of an ion thruster such that the magnitude and direction of the magnetic induction within the discharge chamber could be accurately reproduced from the specified dimensions and materials used to construct the magnetic circuit. The magnetic circuits of typical ion thrusters have evolved more by empirical processes than by analytic design and are not, in fact, tractable to usual design analysis procedures. In designing an efficient magnetic circuit using permanent magnets, the usual practice is to keep the air gap very short in comparison to the path of the lines of force through the magnetic materials. For an ion thruster, such a design would weigh far too much to be feasible, and successful magnetic configurations have been achieved using large air gaps and relatively little permanent magnet and pole-piece material. To explore the sensitivity of the measured magnetic induction distribution (magnetic mapping) to changes in the magnetic circuit elements, the thruster simulator shown in Figure 29 (a and b) was constructed to facilitate component variations. Measurements of the axial and radial components of the magnetic induction were

M11119



(a)

M11120



(b)

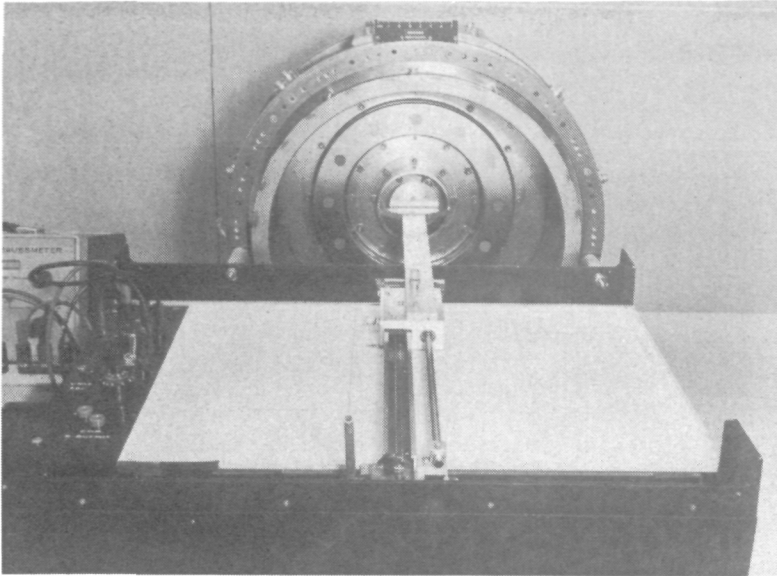
Figure 29. Thruster made-up for simulating and documenting magnetic induction distributions.

performed using the precision probe positioning device shown in Figure 30 (a and b). The thruster simulator could also be easily rotated to measure azimuthal variations in the magnetic induction.

Several magnetic induction mapping measurements were performed at the beginning of the project to compare the magnetic mappings obtained using the simulator with those measured in thrusters SN801 and SN804.

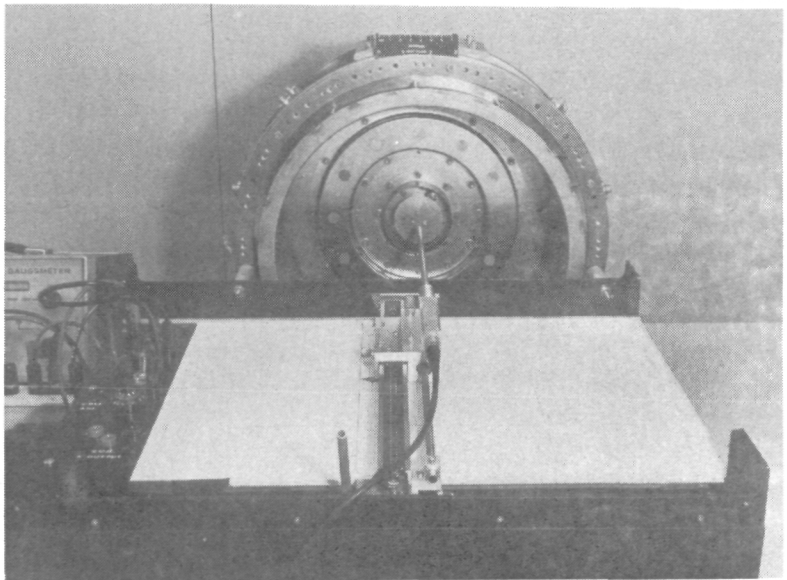
All magnetic configurations were constructed using "calibrated" permanent magnets and are considered to be magnetically identical. We do not believe that the operational performance variations observed with thrusters SN801 and SN804 can be explained in terms of magnetic induction distribution variations, since thrusters that have magnetic mappings which agree as closely as those shown in Figures 31 and 32 are considered magnetically identical. The differences in performance noted in thrusters SN801 and SN804 were correlated with magnetic baffle operation, however, and magnetic measurements were made in the cathode polepiece interior (with the baffle removed) as a function of baffle coil current. Figures 33 and 34 show the expected variations in the axial distribution of both axial and radial field components as functions of magnetic baffle coil current. These characteristics were measured for both thrusters, and Figures 35 and 36 compare the differences caused by operation with baffle coils of 9.5 and 11.5 turns. The construction of the 9.5 turn baffle coil also altered its relative position with respect to the cathode orifice and consequently the observed difference in performance is attributed at least partially to the different relative location of this coil. Other geometric dissimilarities also existed; correcting these discrepancies established equivalent thruster operation. This mapping exercise did not define any specific magnetic circuit design criteria, but it highlighted the importance of field variations in the cathode pole region. It also verified the correlation of identical mappings such as shown in Figures 38 and 40 with performance equivalence.

M10530



a

M10531



b

Figure 30. Magnetic field plotting apparatus. (a) With alignment fixture. (b) With Gaussmeter probe in place.



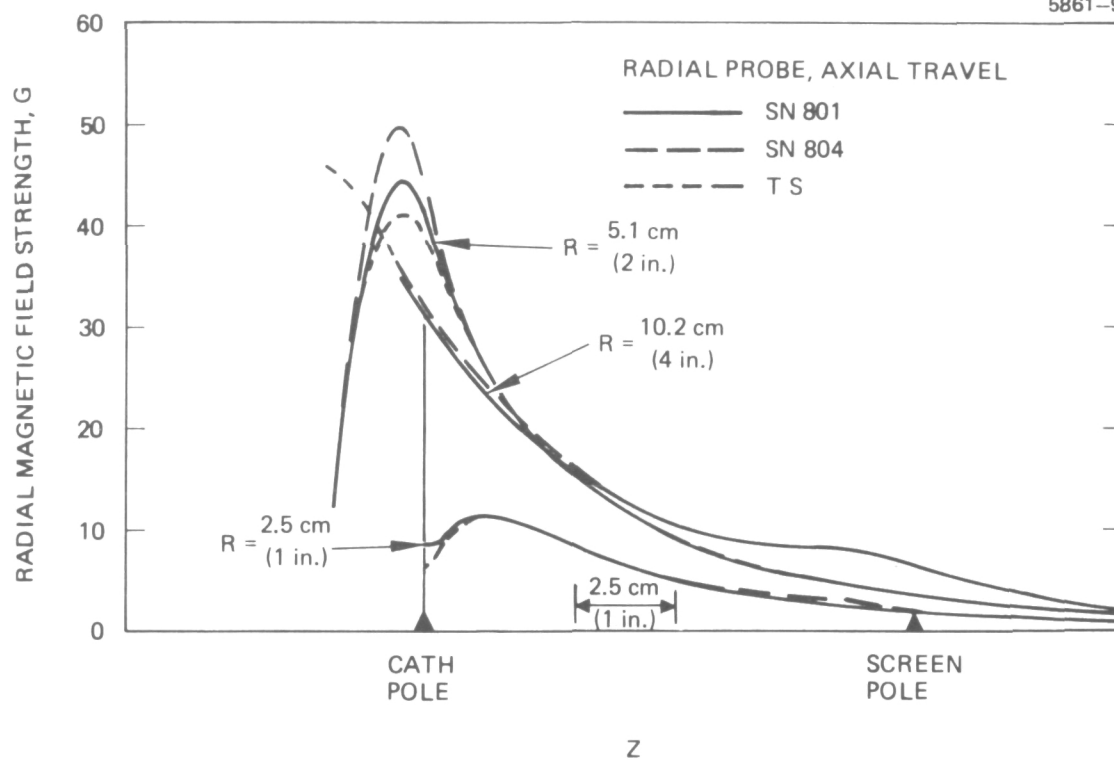


Figure 31. Comparison of radial magnetic field component versus axial distance for thrusters SN801, SN804, and the thruster simulator (TS) with radial location as a parameter.

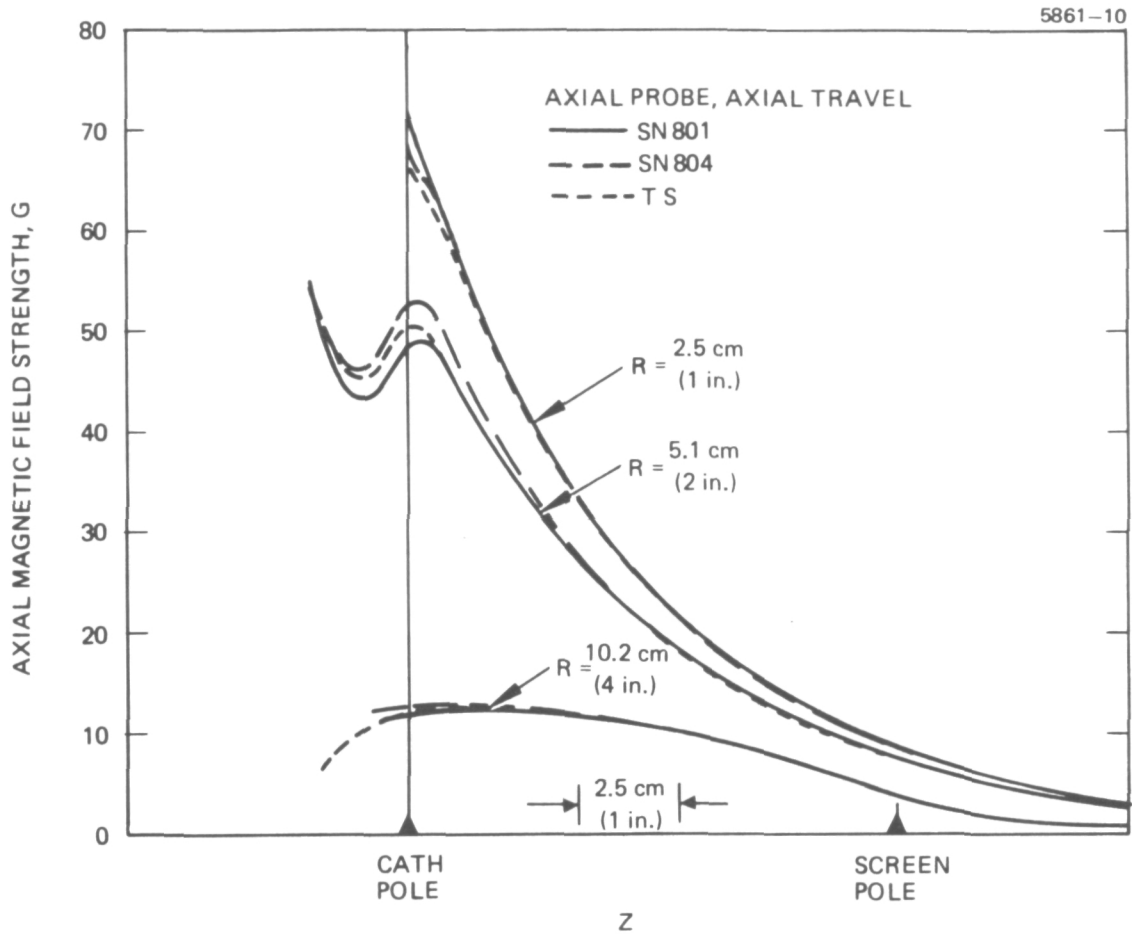


Figure 32. Comparison of axial magnetic field component versus axial distance for thrusters SN801, SN804, and the thruster simulator (TS) with radial location as a parameter.

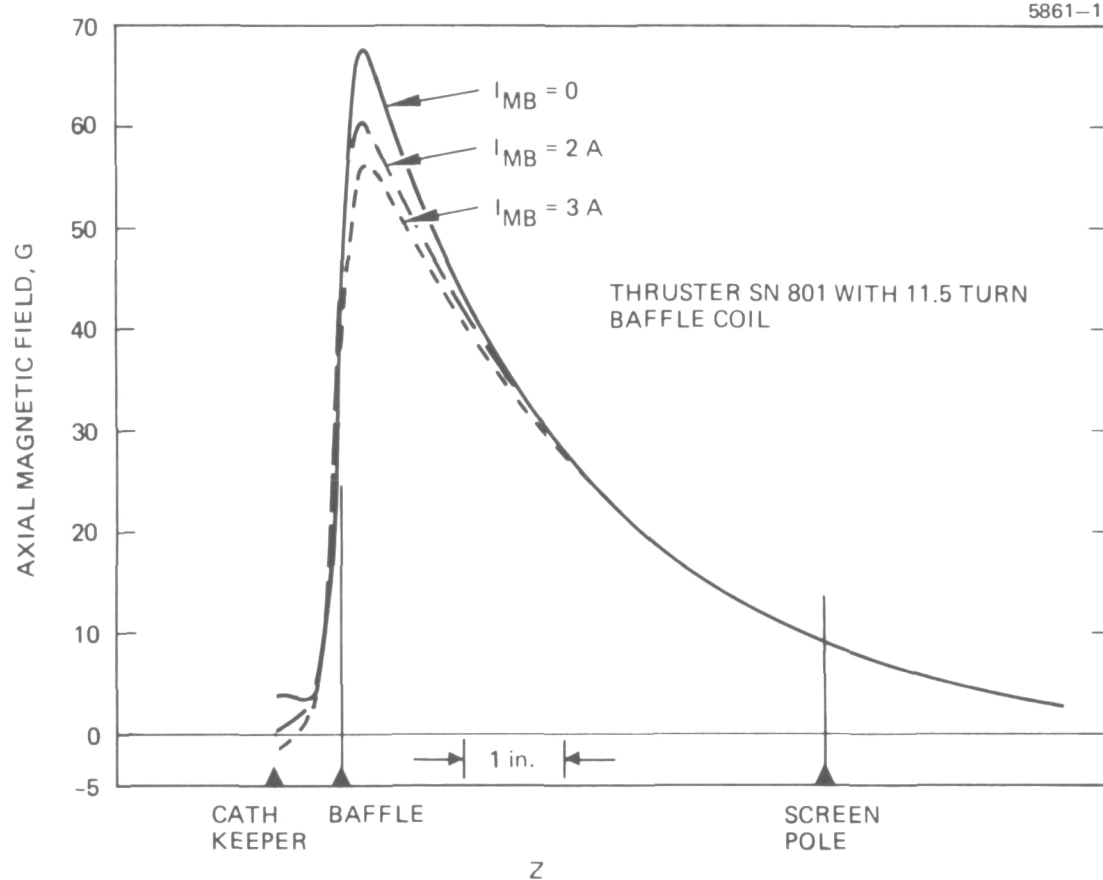


Figure 33. Axial magnetic field component versus axial location (on centerline) with magnetic baffle coil current as a parameter.

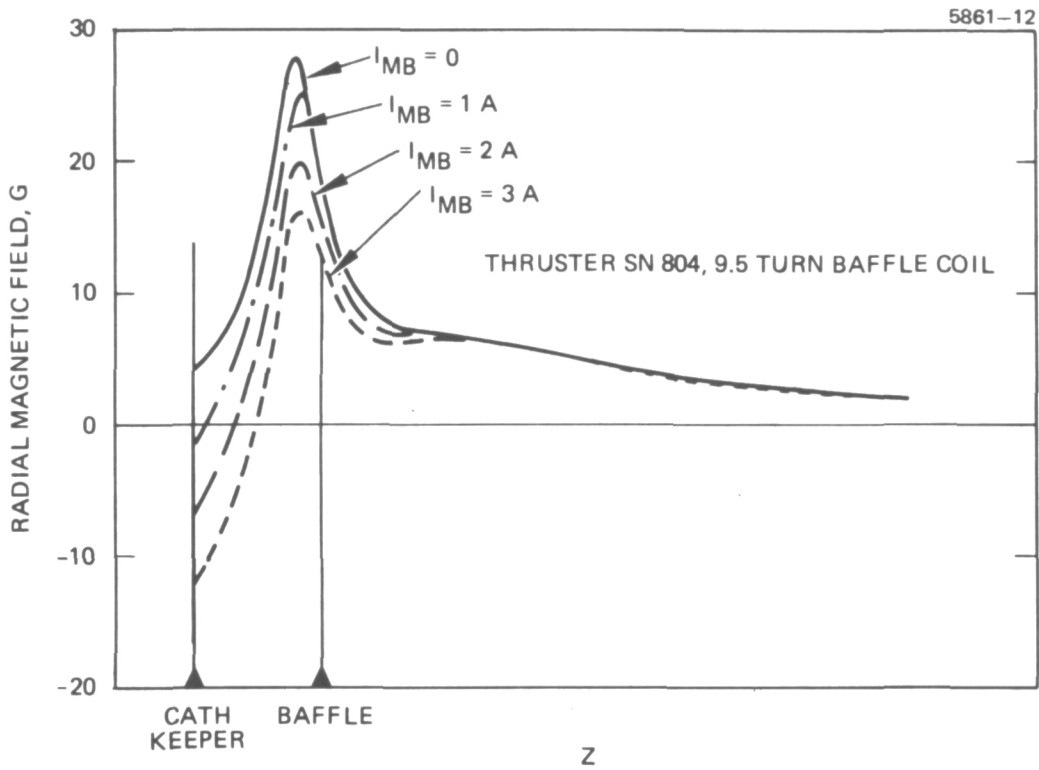


Figure 34. Radial magnetic field component versus axial location (on centerline) with magnetic baffle coil current as a parameter.

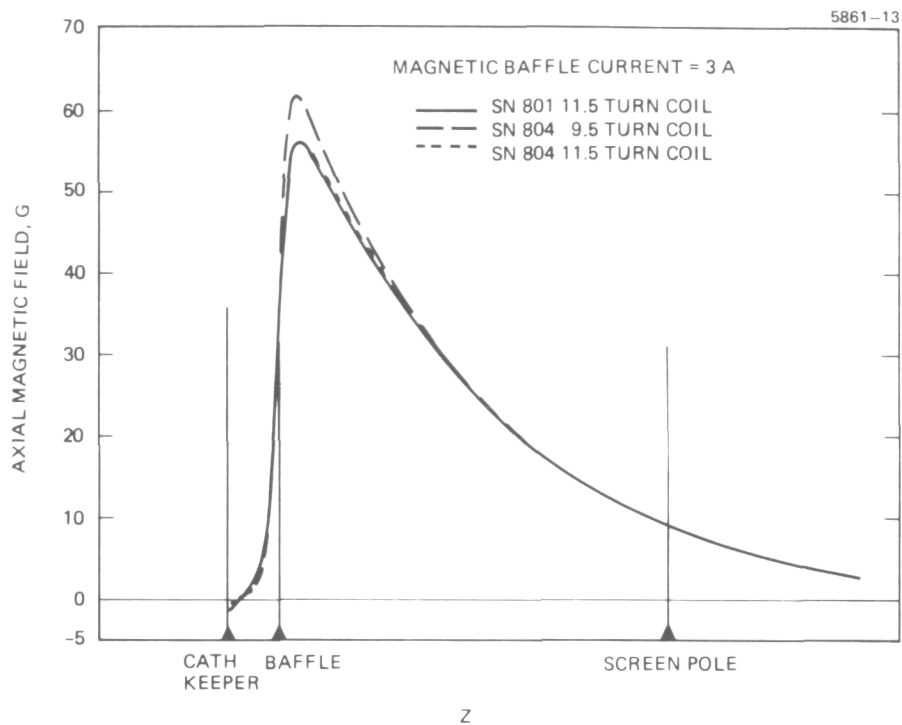


Figure 35. Axial magnetic field component versus axial location (on centerline) comparing variations between thruster SN801 and thruster SN804 with different baffle control coils.

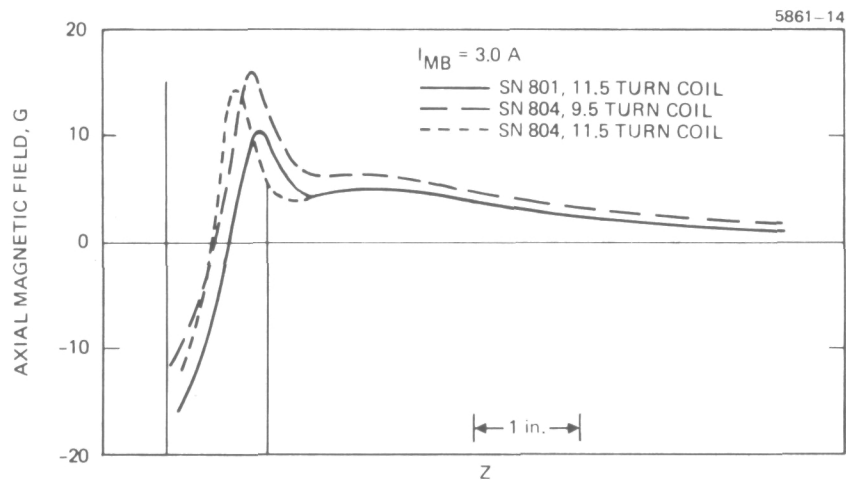


Figure 36. Radial magnetic field component versus axial location (on centerline) comparing variations between thruster SN801 and thruster SN804 with different baffle control coils.

The comparisons shown in Figures 31 through 36 identify a problem encountered in this project — how to compare magnetic mappings. Overlays such as those in these figures are time consuming and subject to considerable human error in aligning the reference points. Even if the aligning problem were eliminated, it was observed that the types of magnetic circuit changes that we initially thought were significant only produced subtle changes in comparisons such as those shown in the preceding figures and it is difficult to interpret such changes as being important to thruster operating parameters. With this consideration, the following variations in magnetic circuit will be discussed:

- 400 series and 700 series magnetic circuit design
- Effects of polepiece/magnet contact
- Azimuthal uniformity considerations.

1. Comparison of 400 Series and 700 Series  
Magnetic Circuits

The iron and magnet components and dimensions of 400 series and 700 series thrusters are shown in Figure 37. The principal differences in the components are the baffle support members and the radial magnet retainers. Both magnetic circuits produce essentially the same magnetic mappings in the regions where the discharge plasma is contained. Subtle differences in discharge chamber performance and operating characteristics have been observed, however, and an attempt was made to locate some property of the magnetic field that could explain such differences. Consequently, mappings were performed on these configurations with baffle coil current ( $I_{MB}$ ) as a parameter. To represent magnetic induction strength and direction more adequately, measured components were used to generate graphical vector plots of magnitude and direction, as shown in Figures 38 and 39. Although some subtle differences were noted in other measurements obtained close to the pole pieces, the representations in Figures 38 and 39 show the most significant systematic variation. The main difference is that, in the

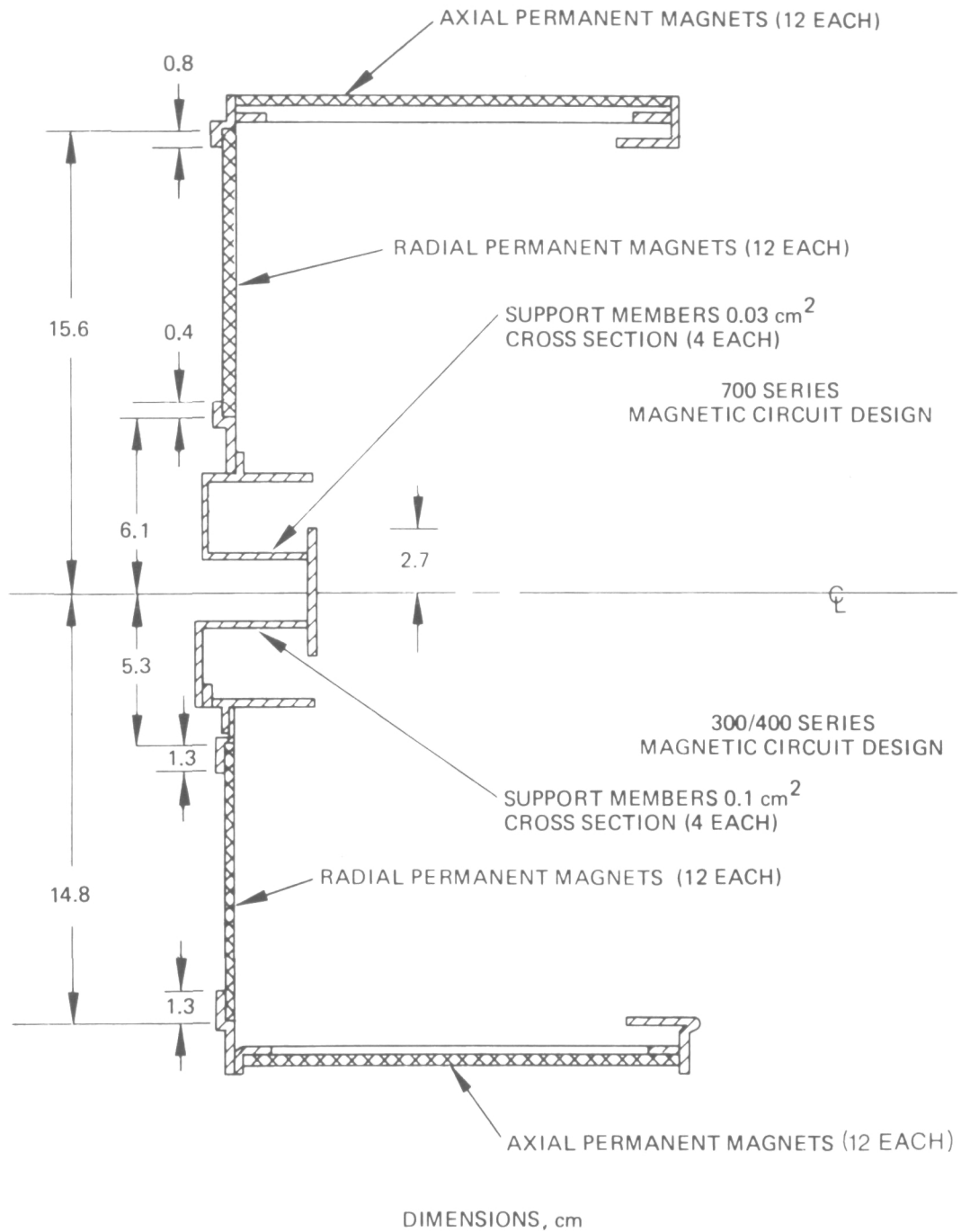
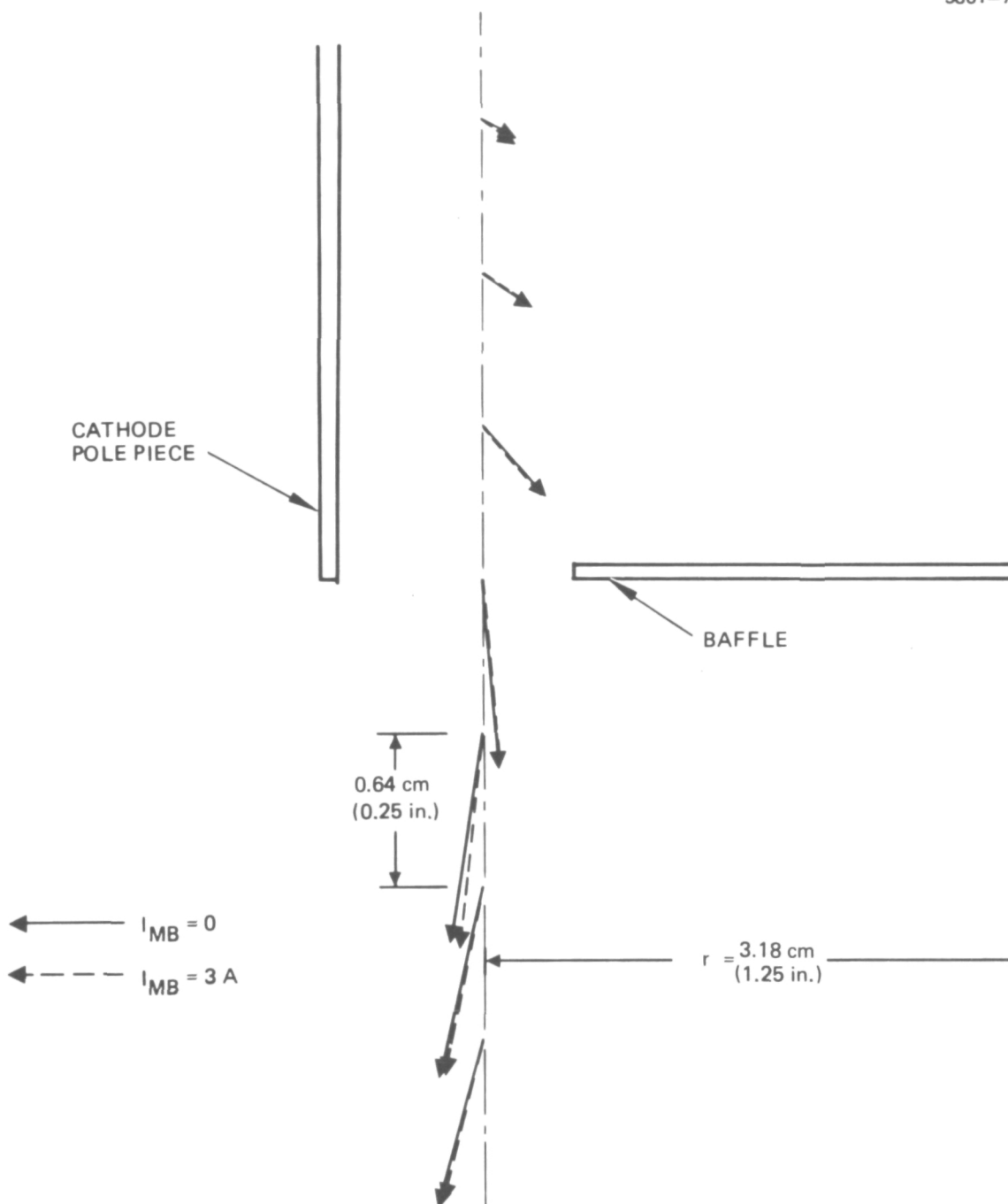


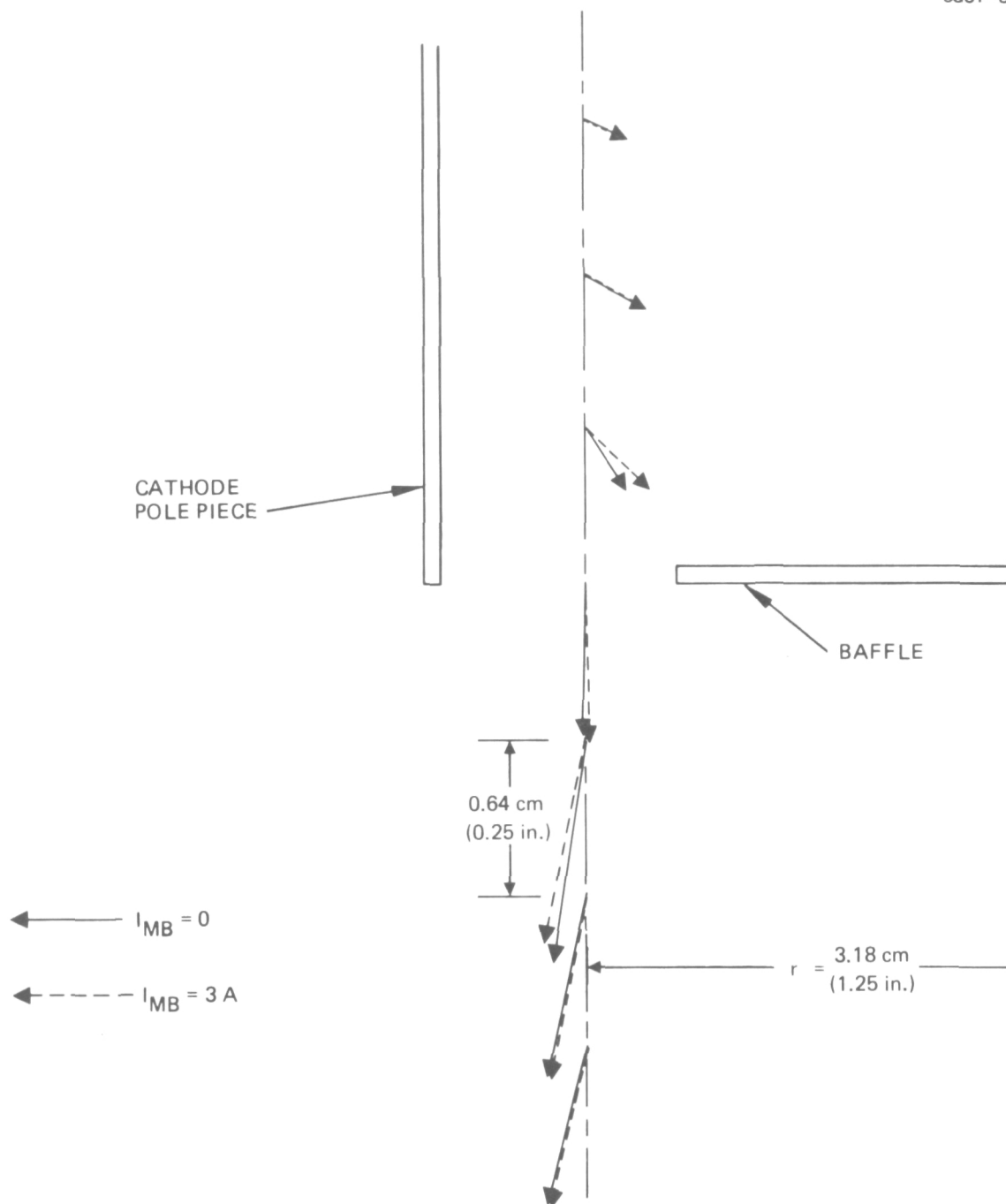
Figure 37. Dimensions of magnetic circuits representative of 400 series thrusters and 700 series thrusters.



MAGNETIC VECTOR SCALE: 20 g/cm

Figure 38. Comparison of magnetic field vectors along axial path at  $r = 1.25 \text{ in.}$  for magnetic baffle currents,  $I_{MB}$ , of 0 and 3 A. Baffle support is 700 series design.





MAGNETIC VECTOR SCALE: 20 g/cm

Figure 39. Comparison of magnetic field vectors along axial path at  $r = 1.25 \text{ in.}$  for magnetic baffle currents,  $I_{MB}$ , of 0 and 3 A. Baffle support is modified 400 series design.

configuration with the 700 series baffle support, there is very little change in the magnetic vector along a path through the baffle polepiece gap when the baffle coil is energized by 3 A of current. With the 400 series baffle support, however, the field in the gap is measurably changed by current in the baffle coil. Comparisons of the field vectors for locations in the vicinity of the cathode also show greater changes for the configuration with the 700 series baffle support. These comparisons lead to the conclusion that the cross section of the thin iron support members in the 700 series baffle support are only marginally able to carry the combined permanent magnet flux and that generated by the baffle coil. Since the 400 series baffle design, on the other hand, had adequate iron to provide a low-reluctance path for both circuits, the field change appears in the gap region as intended. Thus, the plasma potential distribution within the cathode polepiece of the 400 series magnetic design could possibly be depressed throughout the region, although the potential and begin to rise in the 700 series design in the immediate vicinity of the cathode. If this were the case, the effects of the magnetic baffle and the primary electron energy distributions would be different in each case and would perhaps account for the observed operational differences.

## 2. Effects of Contact Between the Polepiece and the Magnet

We initially thought that the repetitive making and breaking of contacts between the permanent magnets and soft iron polepieces could degrade the magnetic circuit. Although magnets were removed and replaced (carefully) either individually or in combination up to 50 times, no measurable change in the magnetic mapping could be induced. Similarly, small air gaps introduced between the magnets and soft iron polepieces ( $\sim 0.03$  cm) did not produce measurable changes in the magnetic mapping of the thruster simulator.

The magnetic circuit is not entirely insensitive to manipulation of its components, however, and certain locations very near the contact of polepieces and magnets are sensitive to magnet and polepiece

contact. Positioning the gauss meter at one of these locations and varying a single radial magnet contact can produce a detectable change in the measurement. Because magnet/polepiece contacts are located at an appreciable distance from the active discharge region, these variations are not considered significant to thruster operation (although there may be some implication to far-field magnetic contamination where exact cancellation of thruster fields is necessary for spacecraft science instrumentation). Since magnetic induction variations in the cathode orifice region (as introduced by the baffle coil) have been linked to the discharge chamber and to operational and performance variations, changes in this region introduced by differences in the magnet and polepiece contact are probably important to discharge chamber operation. The implication is that the magnetic circuit should be designed such that any leakage fields that result from variation in magnet and polepiece contact do not pass through or are shielded out in the cathode orifice region.

### 3. Azimuthal Uniformity Considerations

The conclusion that polepiece-to-magnet contact has little effect on the magnetic mapping in the main discharge chamber raises the question as to whether it is necessary to use the relatively massive members now used to form the transition between radial and axial magnets. The thruster simulator was assembled using only the screen and cathode polepieces, with the magnets interconnected as shown in Figure 40. Magnetic mappings again showed no measurable differences in the active discharge chamber volume. Azimuthal variations were detectable only in the regions near these discrete transitions. Eliminating the cylindrical ring-type transition members as now designed could provide a weight saving but would also need to be evaluated in terms of any asymmetries which might be introduced in the far field "magnetic contamination" associated with such a design.

The objective of this project has been to form guidelines for assessing modifications to improve the magnetic circuit such that the desired magnetic induction distribution is achieved while optimizing the

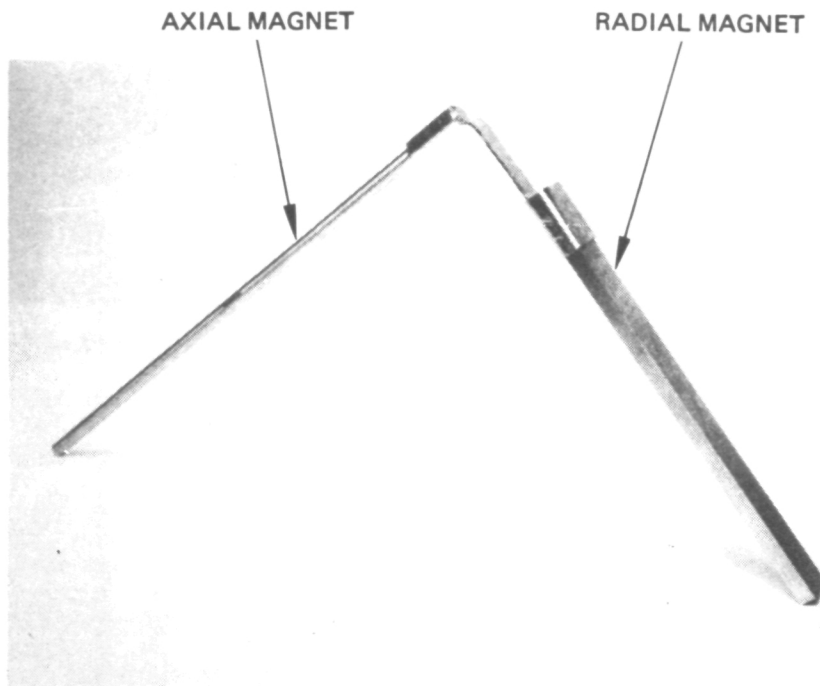


Figure 40. Photograph of soft iron member interconnecting radial and axial magnets to eliminate complete polepieces now used.

assembly in terms of quantities such as reproducibility, weight, or ease of fabrication. This effort has been prompted by observed anomalous differences in operational characteristics between thrusters thought to be identical in construction. The investigation has concentrated on magnetic geometries approximating the 700 and 800 series EMT design. The findings are summarized below:

- Changes in permanent magnet-to-iron polepiece contact cannot measurably influence the magnetic field distribution in the region of the active discharge volume (the far-field region).
- Except for the polepieces themselves, soft iron magnetic circuit components only influence the near-field region (the volume contained within 1 to 2 cm of the iron component).

- Although permanent magnet design principles do not apply quantitatively (because of the relatively large air gap), the qualitative rules governing location of the magnets and polepieces appear applicable, i.e., the field in the air gap is less influenced by fringing conditions if the permanent magnets are employed as the circuit elements closest to the gaps.
- The near-field region in the interior of the cathode polepiece is a "flux-leakage" region and can be measurably influenced by polepiece contact, residual polepiece magnetism, and relatively minor changes in polepiece dimensions.

#### E. Neutralizer Insert Tests

This project is a continuation of the neutralizer studies begun under the preceding contract (NAS3-17831). The neutralizer propellant flow rate of a 30 cm thruster is controlled in proportion to the neutralizer keeper discharge voltage. Tests performed under the preceding program and data obtained in the endurance test (NAS3-15523) indicated that the relationship between the neutralizer propellant flow rate and neutralizer keeper voltage varied with time. Work was performed both at NASA LeRC and at HRL under other programs to correct this anomaly. The current program began with an analysis of recent results and the formulation of a test project to investigate the remaining uncertainties.

Our review of neutralizer technology showed that the typical neutralizer control characteristics measured with neutralizers having impregnated porous tungsten inserts has the form shown in Figure 41. The limits of control are defined by a lower operating vaporizer temperature (vapor flow) at which the neutralizer decouples and by a higher operating temperature point at which the vaporizer power is full on. The control range  $\Delta V_{NK}$  between these extremes is approximately 2.5 V for the data shown in Figure 41 (taken at a keeper current of 2 A). At lower keeper currents, the control range  $\Delta V_{NK}$  decreases to about 1.5 V and  $I_{NK} = 1.5$  A. This control range and neutral Hg consumption is comparable to previous neutralizer designs which used rolled foil

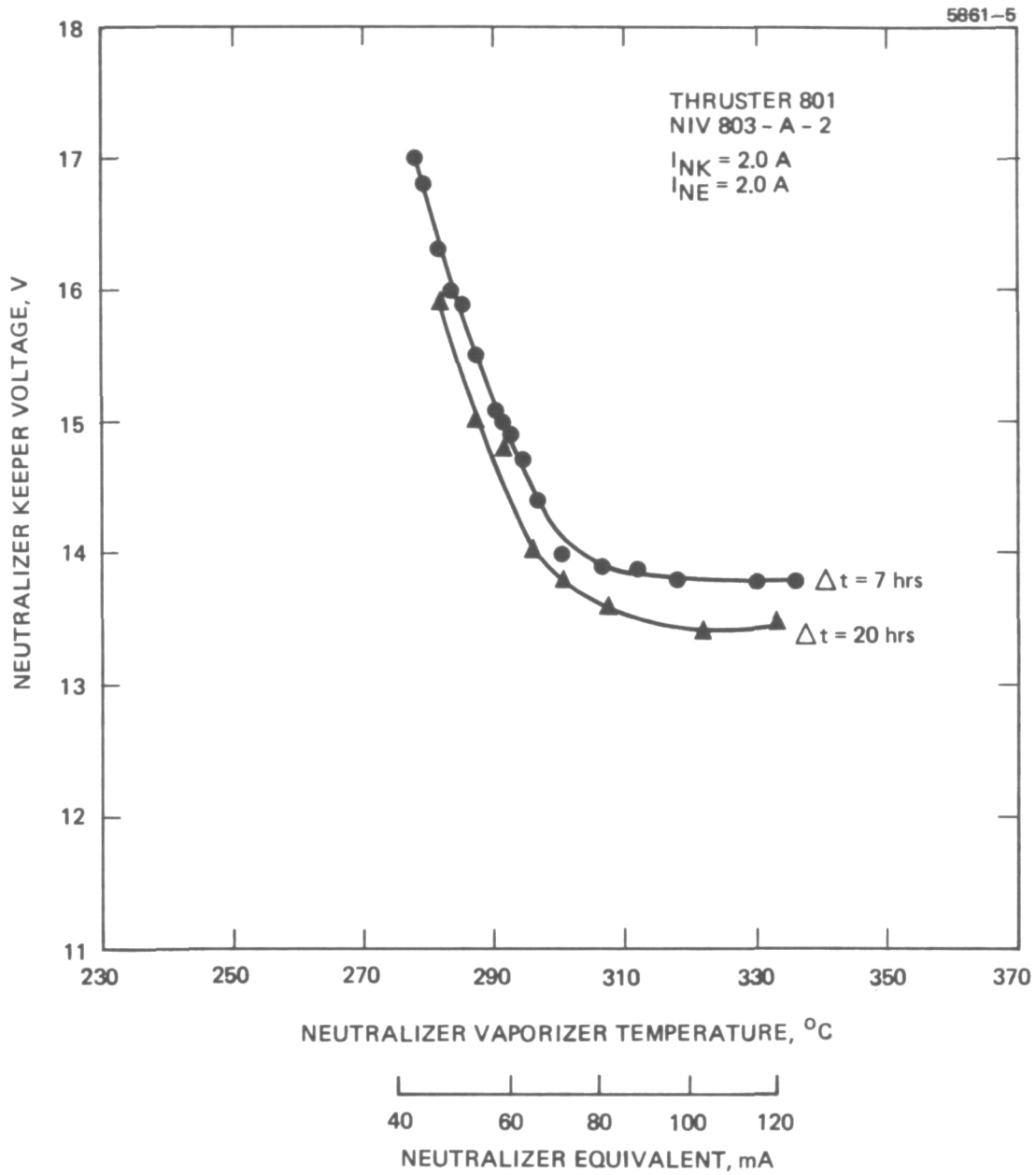


Figure 41. Typical neutralizer control characteristic measured on 30 cm neutralizer.

inserts<sup>14</sup> and to the baseline neutralizer geometry of Bechtel's work<sup>15</sup> (which investigated the effect on neutralizer performance of different neutralizer and keeper geometries). The baseline neutralizer cathode and keeper geometry of this latter work and the present 30 cm neutralizer have the following dimensions in common: cathode orifice, 0.38 mm diameter x 1.27 mm long (15 mil x 50 mil); keeper electrode aperture 6.35 mm diameter x 0.114 mm thick; (0.25 in. x 45 mil); keeper spaced 1.39 mm (55 mil) from cathode. These neutralizers have similar control characteristics for a given keeper current, and the use of an impregnated insert rather than a foil insert appears to have eliminated the undesirable mode shifting which was observed with the rolled Ta foil insert neutralizer (see Figure 42).

Thus the 30 cm thruster neutralizer design now being used in the EMT programs seems adequate to satisfy the present requirements. Possibilities for advancing neutralizer technology remain in the following areas:

- Documentation of impregnated insert lifetime capability versus operating temperature
- Reduction of keeper discharge power required to establish adequate control range
- Demonstration of stable control characteristics for all beam currents within the throttling range
- Exploration and elimination of factors causing the keeper discharge to extinguish during beam over-current recycling.

Of these possibilities, the most important is long life operation; consequently, the task of evaluating the capacity of an impregnated porous tungsten insert for providing an adequate barium supply was selected by the NASA and HRL program managers as most appropriate to this project.

A test fixture was designed and built to heat 10 cathodes containing impregnated inserts at five different temperatures under high vacuum conditions for 1000 hr. The cathode operating temperatures

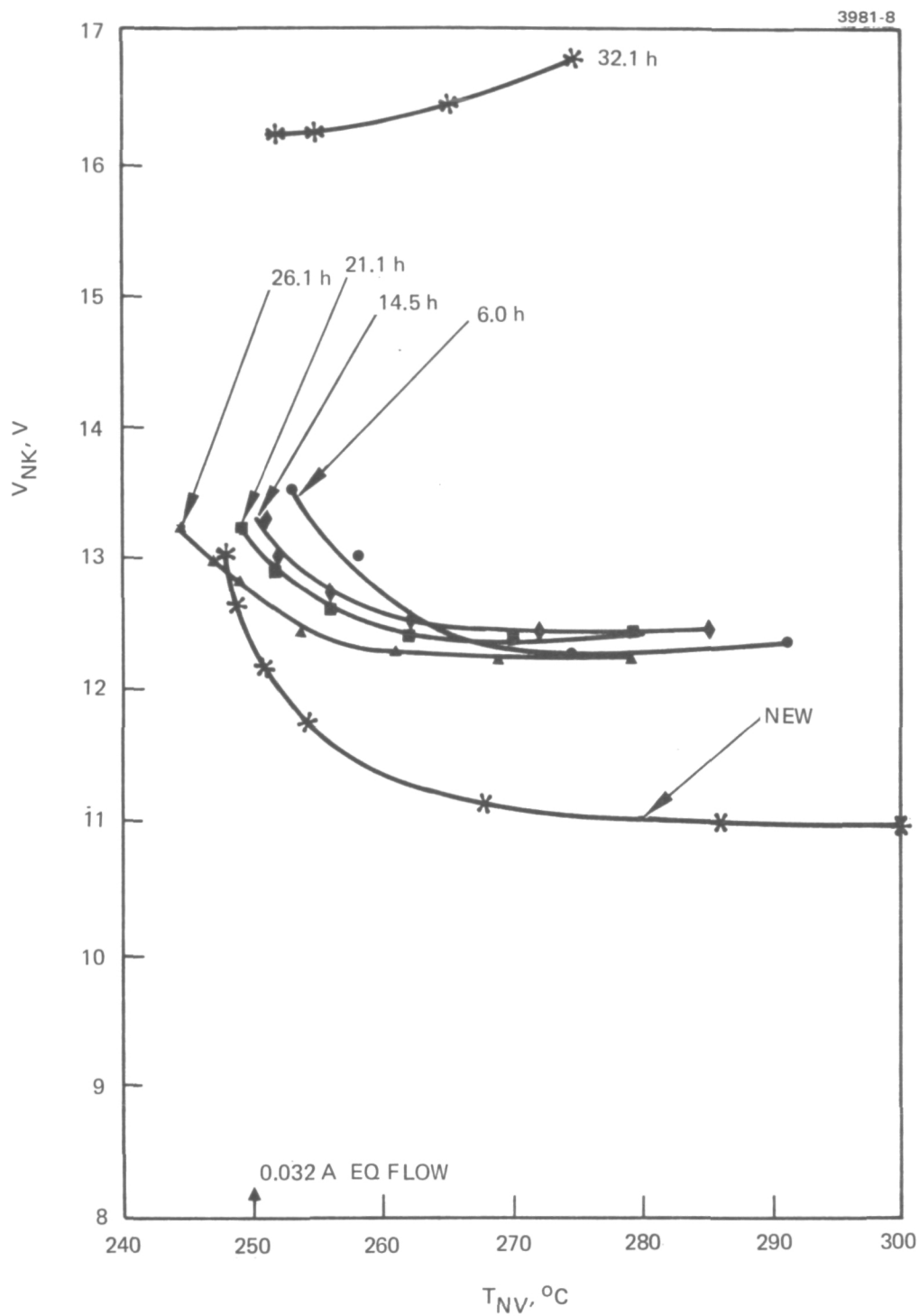


Figure 42. Variation in characteristic after accumulated time as indicated.  $I_{NK} = 1.5$  A,  $I_B = 2.0$  A.



were ambient, 1000°C, 1100°C, 1200°C, and 1300°C. Cathode heaters were extended approximately 1.2 cm on either side of the insert location so that a more uniform insert temperature was maintained. The Ta cathode tube (0.635 cm o.d. x 0.584 cm i.d.) was plugged on the upstream end and had an EMT design neutralizer cathode orifice (0.038 cm diameter, 0.127 cm tip thickness) at the end where the inserts were located flush with the tip. Cathode tubes were approximately 7.5 cm long, clamped at the upstream (plugged) end, and held at fixture ambient (~300°C). Insert temperatures were calibrated with respect to both heater power input and to the temperature measured on the external surface of the cathode tip. Temperatures were measured, for calibration, with both an optical pyrometer and platinum/platinum-rhodium thermocouples, using a bridge to measure thermocouple emf. Cathode tubes, plugs, and the test fixture were operated at maximum temperature under vacuum for 24 hours to fully outgas the materials used before the inserts were installed. The vacuum system used for the test was vac-ion pumped and interlocked so that it was fail-safe in case of a power failure.

The impregnated porous tungsten inserts, obtained from Semicon, Inc., were designated as type S-84 with impregnant SRLV211. The porous tungsten was 84% dense and the pore size was categorized as 0 to 3  $\mu\text{m}$ , 35%; 3 to 5  $\mu\text{m}$ , 50%; and ~5  $\mu\text{m}$ , 15%. The impregnant was  $4 \text{ BaCO}_3 \cdot \text{CaO} \cdot \text{Al}_2\text{O}_3$ , and each insert contained an exactly weighed amount of impregnant in the range of 150 to 200 mg. The insert material is a thick cylindrical tube with an o.d. of 0.53 cm (0.25 in.), i.d. of 0.381 cm (0.15 in.), and a length of 2.54 cm (1 in.). Inserts were weighed immediately after attaching the tantalum lead, which is normally used as an electrical connection but was installed here to facilitate handling and to make the test more representative. An electronic microbalance was used for weighing the inserts and total weight was recorded to the nearest 0.01 mg (the accuracy of the balance is  $\pm 0.01$  mg).

The test was performed using conventional laboratory supplies with a line voltage stabilizer. Temperatures were monitored and

recorded daily during the normal work week and minor adjustments were made for noted temperature excursions. Consequently, temperatures were maintained constant only to about an accuracy of  $\pm 50^{\circ}\text{C}$ , but with most time being logged near the set point. After 1000 hr of test time, the system was allowed to cool for 12 hr and then opened for analysis. The test cathodes were removed from the test fixture and the inserts were carefully removed and weighed. The results are summarized in Table 5. Except for Sample 2, it is apparent that weight loss is in direct proportion to operating temperature. The test record shows that the thermocouple readings were low over a considerable portion of the test of Sample 2, even though the power readings were constant. Consequently, it is considered probable that the temperature was not  $1300^{\circ}$  for this sample during the total test period. Another observation is that there was also weight loss for the ambient samples. This would be the case if the initial weight included some absorbed water vapor. In addition to showing a direct relationship between weight loss and temperature, the samples had a deposit on the upstream plug and internal surfaces of the cathode tube that was inversely proportional to tip temperature, with the ambient samples having no deposit or discoloration whatsoever. The last column of Table 5 has been computed on the basis that all samples contained approximately 9.5 mg of absorbed water. On the basis of this assumption, the adjusted fractional weight loss of barium has been plotted in Figure 43 as a function of temperature.

One sample for each temperature was sent to a vendor for chemical analysis to determine total barium content. The samples included the insert and the cathode tube and plug. Samples were dissolved in acid and analyzed for total barium. The results are shown in Table 6. Although the loss rates for Samples 1 and 3 agree quite well with the estimates based on weight loss, the lower temperature samples had an unexplainably high loss rate, and the loss as determined by weight is considered more credible.

Table 5. Summary of 1000 hr Insert Test Data  
Determined by Insert Weight Loss

Sample	Operating Temperature, °C	Weight Loss, g	Impregnant Weight, <sup>a</sup> g	Weight Loss, %	Total Ba <sup>b</sup> Contained, g	Ba Loss, %	Adjusted <sup>c</sup> Ba Loss, %
1	1300	0.06893	0.1891	36.5	0.1347	51.2	44.0
2	1300	0.03410	0.1563	21.8	0.1113	30.6	22.6
3	1200	0.03778	0.1479	25.5	0.1053	35.9	27.3
4	1200	0.04720	0.1747	27.0	0.1244	37.9	30.7
5	1100	0.02453	0.1676	14.6	0.1194	20.5	13.0
6	1100	0.02895	0.1801	16.1	0.1283	22.6	15.5
7	1000	0.01405	0.2005	7.0	0.1428	9.8	3.5
8	1000	0.01225	0.1910	6.4	0.1360	9.0	2.4
9	300	0.00950	0.1844	5.2	0.1313	7.2	—
10	250	0.00948	0.1678	5.6	0.1195	7.9	—

<sup>a</sup> Consists of 4 BaO · CaO · Al<sub>2</sub>O<sub>3</sub>.

<sup>b</sup> Ba contained is 71.2% by weight.

<sup>c</sup> Assumes weight loss of samples 9 and 10 to be totally H<sub>2</sub>O and representative of H<sub>2</sub>O loss for all samples, therefore all weight losses are reduced by 0.0095 g.

T2099

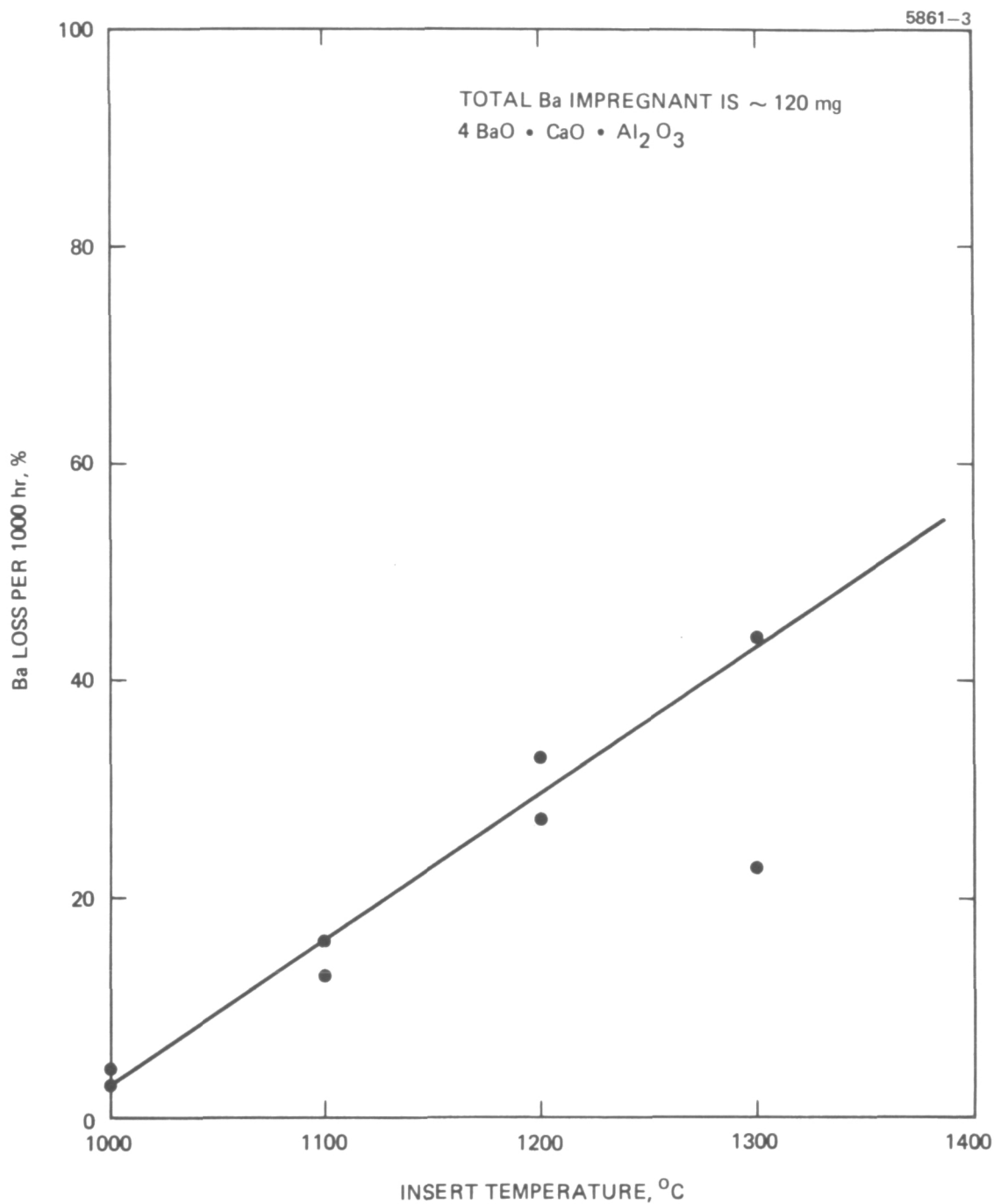


Figure 43. Barium loss per 1000 hr versus operating temperature for impregnated porous tungsten insert material (as determined by weighing entire insert sample).

Table 6. Summary of 1000 hr Insert Test Data  
Determined by Chemical Analysis of the  
Insert and Cathode

Sample	Operating Temperature, °C	Initial Ba Content, mg	Final Ba Content, mg	Ba Loss, mg	Ba Loss, %
1	1300	134.7	67.5	67.2	49.9
3	1200	105.3	70	35.3	33.5
5	1100	119.4	84.4	35.0	29.3
7	1000	142.8	80.9	61.7	43.2
9	300	131.3	70.1	61.2	46.6
1 <sup>a</sup>	1300	0	2.5		
3 <sup>a</sup>	1200	0	4.4		
5 <sup>a</sup>	1100	0	2.6		
7 <sup>a</sup>	1000	0	1.2		
9 <sup>a</sup>	300	0	0.04		
<sup>a</sup> Analysis of cathode tube and plug.					

T2100

An accurate analysis of the barium loss mechanisms and projected insert lifetime is a very complex problem<sup>16</sup> in that the factors to be considered include:

- The type of reaction that liberates barium at a given temperature
- The barium available from the predominant reaction
- The barium migration through the pores
- The barium evaporation rate at the vacuum-solid interface

- Re-condensation of barium vapor on the insert surface
- Formation of nonvolatile barium compounds
- Formation of barium compounds that do not lower the surface work function.

Within the scope of this project, only cursory consideration of these factors was attempted. To establish a zero-order estimate of insert lifetime, consider that all the barium can be made available for lowering the surface work function and that adequate coverage can be maintained up to the point that only 10% of the initial barium remains. If  $R$  is the percentage of barium consumed in the time period  $T$ , then the lifetime  $nT$  is determined by  $(1 - R)^n = 0.1$ . For an  $1100^{\circ}\text{C}$  operating temperature,  $R$  is 0.15 and  $n$  is approximately 14, which yields an insert lifetime of 14,000 hr. Measured neutralizer tip temperature is usually somewhat lower ( $1000$  to  $1050^{\circ}\text{C}$ ) and insert lifetimes of about 20,000 hr can be expected.

Although the experiments performed here were relatively unsophisticated and order-of-magnitude in nature, the results indicate that insert lifetime will not present a lifetime problem unless cathode temperatures exceed  $1100^{\circ}\text{C}$ . Moreover, the experiments were performed under high vacuum conditions, whereas under actual cathode operation the mercury vapor pressure in the insert region would be about 1 Torr. The presence of this gas pressure should tend to suppress the Ba evaporation rate somewhat and extend insert lifetime.

#### F. Vaporizer Material Evaluation

Thruster and component testing at NASA LeRC and in the Endurance Test Program (NAS3-18914) has produced anomolous changes in vaporizer flow rate characteristics. The objectives of this task were to assist in identifying possible causes of the vaporizer malfunctions and to evaluate commercially available porous tungsten material as a possible substitute for the porous tungsten now being used to fabricate EMT vaporizers.

## 1. Analysis of Vaporizer Anomalies

The work done on this portion of the project was directed primarily towards analyzing the observations made in the endurance testing of thruster SN901. The phenomenon observed was a decrease in the vaporizer temperature and heater power needed to produce the required cathode propellant flow rate. Both sudden and gradual changes had been observed and only speculative explanations could be offered. Among these were:

- Cracking of porous tungsten as a result of thermal cycling
- Wetting of porous tungsten as a result of mercury contaminants
- Partial penetration of porous tungsten by mercury as a result of large pores.

Because work at NASA LeRC showed the phenomenon to be reversible by vaporizer bake-out, the first possibility was dismissed. Although wetting a porous tungsten vaporizer usually results in complete penetration of the porous tungsten, the possibility of partial wetting led to a spectro-chemical analysis of the mercury in the endurance test mercury reservoirs. Table 7 gives the chemical composition of the samples taken. There is no appreciable difference seen in the samples analyzed and since only the cathode vaporizer displayed anomalous behavior, it is unlikely that contamination of the mercury could be the source of difficulty.

To investigate the possibility that large pores were responsible for partial mercury penetration, several samples of material were sent to NASA LeRC where they were examined with an electron microscope. Comparison of the vaporizer material being used in the 800/900 series EMT components with that in the SERT II vaporizer material showed that pore size was indeed more irregular in the 800/900 series material than in the SERT II material. Since the materials were designed to have different temperature-flow characteristics, further comparison seemed inappropriate.

Table 7. Composition of Endurance Test Mercury Samples

Element	Cathode Vaporizer Reservoir		Main Vaporizer Reservoir		Neutralizer Vaporizer Reservoir	
	C-1	C-2	M-1	M-2	N-1	N-2
Hg	Major element	Major element	Major element	Major element	Major element	Major element
Ag	0.0063 ppm	0.047 ppm	0.037 ppm	0.020 ppm	ND<0.005 ppm	ND<0.005 ppm
Cu	0.027	0.014	0.013	ND<0.004	ND<0.004	ND<0.004
Si	0.63	1.0	0.87	0.83	1.6	2.1
Mg	0.027	0.014	ND<0.008	ND<0.008	ND<0.008	ND<0.008
Al	ND<0.040	ND<0.040	ND<0.040	ND<0.040	ND<0.040	ND<0.040
Sb	ND<0.15	ND<0.15	ND<0.15	ND<0.15	ND<0.15	ND<0.15
As	ND<0.80	ND<0.80	ND<0.80	ND<0.80	ND<0.80	ND<0.80
Ba	ND<3.5	ND<3.5	ND<3.5	ND<3.5	ND<3.5	ND<3.5
Be	ND<0.0006	ND<0.0006	ND<0.0006	ND<0.0006	ND<0.0006	ND<0.0006
Bi	ND<0.040	ND<0.040	ND<0.040	ND<0.040	ND<0.040	ND<0.040
B	ND<0.040	ND<0.040	ND<0.040	ND<0.040	ND<0.040	ND<0.040
Cd	ND<0.10	ND<0.10	ND<0.10	ND<0.10	ND<0.10	ND<0.10
Ca	ND<0.0080	ND<0.0080	ND<0.0080	ND<0.0080	ND<0.0080	ND<0.0080
Pb	ND<0.30	ND<0.30	ND<0.30	ND<0.30	ND<0.30	ND<0.30
Ni	ND<0.050	ND<0.050	ND<0.050	ND<0.050	ND<0.050	ND<0.050
Pt	ND<0.040	ND<0.040	ND<0.040	ND<0.040	ND<0.040	ND<0.040
K	ND<2.0	ND<2.0	ND<2.0	ND<2.0	ND<2.0	ND<2.0
Mn	ND<0.060	ND<0.060	ND<0.060	ND<0.060	ND<0.060	ND<0.060
Fe	ND<0.060	ND<0.060	ND<0.060	ND<0.060	ND<0.060	ND<0.060
Cr	ND<0.010	ND<0.010	ND<0.010	ND<0.010	ND<0.010	ND<0.010
W	ND<2.0	ND<2.0	ND<2.0	ND<2.0	ND<2.0	ND<2.0
Mo	ND<0.040	ND<0.040	ND<0.040	ND<0.040	ND<0.040	ND<0.040
Ta	ND<2.0	ND<2.0	ND<2.0	ND<2.0	ND<2.0	ND<2.0
Co	ND<0.040	ND<0.040	ND<0.040	ND<0.040	ND<0.040	ND<0.040
Au	ND<0.020	ND<0.020	ND<0.020	ND<0.020	ND<0.020	ND<0.020
Na	ND<2.0	ND<2.0	ND<2.0	ND<2.0	ND<2.0	ND<2.0
Sr	ND<0.020	ND<0.020	ND<0.020	ND<0.020	ND<0.020	ND<0.020
Sn	ND<0.14	ND<0.14	ND<0.14	ND<0.14	ND<0.14	ND<0.14
Ti	ND<0.040	ND<0.040	ND<0.040	ND<0.040	ND<0.040	ND<0.040
V	ND<0.10	ND<0.10	ND<0.10	ND<0.10	ND<0.10	ND<0.10
Zn	ND<0.60	ND<0.60	ND<0.60	ND<0.60	ND<0.60	ND<0.60

T2101



An attempt was made to reproduce the anomalous vaporizer behavior under controlled conditions. One sample each of the cathode-isolator-vaporizer (C-IV) and neutralizer isolator vaporizer (NIV) assemblies that had been constructed with the suspect 800/900 series vaporizer material were obtained and a test was initiated to measure flow rate as a function of variations in reservoir pressure. This attempt was frustrated by the failure of the braze joint between the vaporizer housing and the feed line on both components. This produced a liquid leak when reservoir pressure was applied. No other assemblies were available and attempts at a "quick fix" consumed the resources allocated for this measurement.

## 2. Porous Tungsten Evaluation

Porous tungsten material manufactured by Spectra-Mat, Inc., has been used for vaporizer material under an 8 cm thruster program (NAS3-18917) with apparent success. Consequently, materials with three different combinations of particle size and density were purchased from Spectra Mat for evaluation to determine the correct specifications to obtain the desired temperature - propellant-flow characteristics. The porous tungsten materials were made with the following specifications: 5  $\mu\text{m}$  particles at 80% density, 4.5  $\mu\text{m}$  particles at 80% density, and 4.5  $\mu\text{m}$  particles at 75% density.

Of these, the 4.5  $\mu\text{m}$  at 80% best matched the desired flow characteristics; the other combinations produced too much flow at the calibration points of 260°C, 290°C, and 310°C. Four vaporizers were assembled using this material and tested at three temperatures and three pressures; the results are shown in Table 8. The flow rates for all these vaporizers were within, or very nearly within, the acceptable ranges except at the highest pressure. The greatest variation of flow rate with reservoir pressure occurred at the highest temperature. Vaporizer SN 95.5 was selected as the best example and 95.3 as an intermediate example for a 200 hr test at high pressure (414 kPa, 60 psig or an absolute pressure of 541kPa, 78.4 psia) and high temperature (310°C). The test was begun with vaporizer heaters set at

Table 8. Vaporizer Material Test Summary

$T_{VAP}$ , °C	Reservoir Pressure, psig	Mercury Flow Rate (Equivalent mA)				Specified Acceptable Range (Equivalent mA)
		Sample SN95.2	Sample SN95.3	Sample SN95.4	Sample SN95.5	
260	0	21.7	23.5	29.0	21.7	20 to 35
	30	21.7	30.8	30.8	25.3	
	60	27.2	43.4	36.2	23.5	
290		45.3	50.7	41.6	56.1	44 to 75
	30	50.7	70.6	68.7	54.3	
	60	50.7	88.7	90.5	59.7	
310		74.2	97.7	112.2	90.5	91 to 122
	30	83.3	126.7	121.3	97.7	
	60	99.6	172.0	150.2	106.8	
*						
<p>* Chosen for 200 hr test at 310°C, reservoir pressure = 60 psig</p> <p>Note: Material is 4.5 <math>\mu</math>m particle size, 80% dense (specified by Dwg. No. 1095511-95)</p>						

T2102

constant power. Vaporizer temperature (and flow rate) was observed to vary unacceptably under this test condition and the initial test was terminated. This test had been begun with minimal facility preparation and it was necessary to check all possible sources that could produce variations in time or indicated temperature. Among the difficulties identified were:

- Mercury condensation on thermocouple vacuum feed-through insulators
- Power line variations
- Vacuum facility pressure variations

- Thermocouple contact
- Vaporizer heater contact.

The initial test had been conducted with the assumption that measured temperatures were correct and power adjustments were made to accommodate the temperature change. This procedure produced mercury flow variations. It was not possible to isolate one of these as the single source for the problem; however, a combination of test facility and test procedure modifications (as described below) permitted 200 hr of operation without further difficulty.

The bell-jar test facility was modified to provide heat to all electrical feed-throughs, and the test was operated only during periods when the liquid nitrogen level in the cold traps could be kept relatively constant. A second "control" thermocouple was installed on each vaporizer; heater power was controlled to be in proportion to the temperature sensed by these thermocouples. The reservoir pressure was reduced, somewhat arbitrarily, to 276 kPa, 40 psig and that 242 kPa (35 psig) is representative of flight reservoir specifications. The initial test data obtained with these modifications indicated improved stability, and the test was continued until 259 hr of test time had been logged. Variations during the first 226 hr in vaporizer temperature and mercury flow rate are plotted in Figure 44 as a function of accumulated time. Fluctuations are present in both vaporizer temperature and mercury flow rate, but no systematic trend exists. There are correlations between vaporizer excursions and mercury flow rate excursions. The smaller temperature variations seen for sample 95.5 produced smaller mercury flow rate variations. Similarly, the pattern of the mercury flow rate variation appears the same for both vaporizer samples and may still be a consequence of some facility interaction. It is therefore concluded that the variations seen are more likely to have been caused by fluctuations of test apparatus than by a property of the material under test. A more meaningful test of material stability would require more careful preparation and control of the test apparatus to

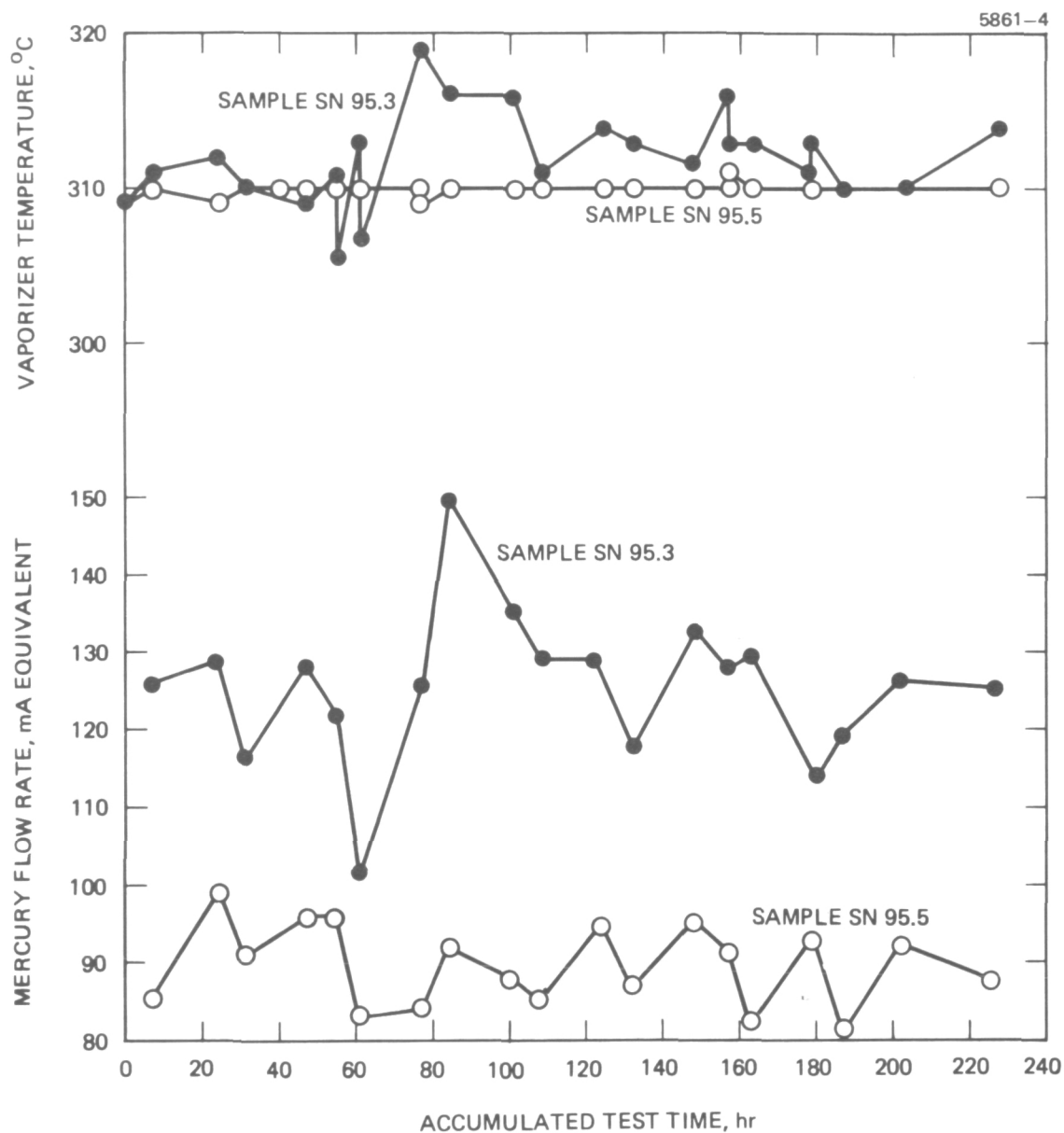


Figure 44. Comparison of mercury flow rate and vaporizer temperature variations during 200 hr test for samples SN95.3 and SN95.5. Head pressure 40 psig, 58 psia.

maintain vacuum conditions, temperatures, and power supply outputs within narrower limits.

In addition to mercury flow calibration, the porous tungsten material was tested for its ability to withstand high reservoir pressure without penetration. It typically required applying pressures in the  $864 \pm 34$  kPa ( $125 \pm 5$  psig) range to the mercury to cause penetration. Vaporizers were also "bubble checked" to evaluate uniformity of vapor transmission; Figure 45 shows a photograph of such a vaporizer surface "bubble" pattern with 55 kPa (8 psig) gas pressure applied. This is considered to be a suitably uniform bubble pattern.

We concluded on the basis of the samples tested that the porous tungsten material obtained from Spectra-Mat, Inc., can satisfactorily meet the mercury-flow-rate — temperature characteristics for cathode and neutralizer vaporizers as specified in the EMT design. Additional testing would be advisable, since the number of samples tested was small and all were from the same lot. Evaluation of samples from several manufacturing lots would provide more conclusive documentation.

5861-2

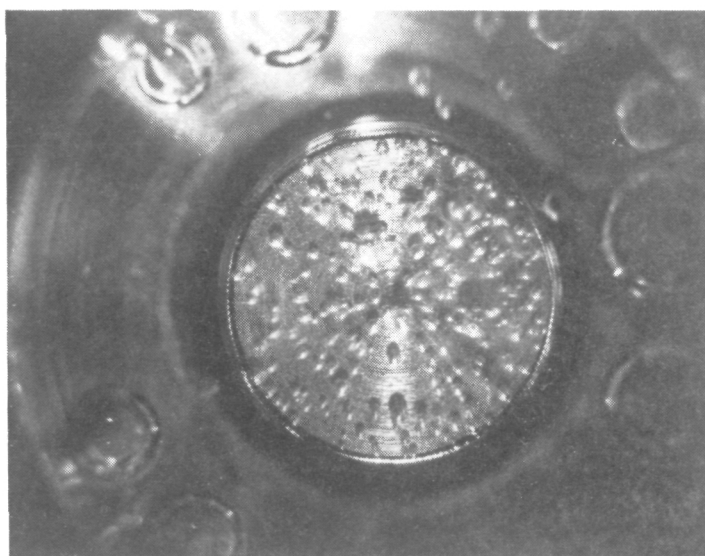


Figure 45. Bubble pattern of vaporizer at 5.5 kPa (8 psig) gas pressure.

### III. HIGH-POWER OPERATION OF A 30 cm THRUSTER

The nominal input power to the 30 cm EMT is considered to be 2.5 kW. The beam voltage is operated at 1100 V and the beam current at 2 A to produce 135 mN (30 mlb) thrust (specific impulse 3000 sec). The purpose of the investigation described below was to determine the capability for and consequences of operating this thruster at higher power and thrust levels. Higher power operation was approached in two ways. In the first, beam current was increased by increasing discharge power and propellant throughput, hence maintaining specific impulse constant. In the second, beam current was kept constant and the beam voltage was increased, thus increasing specific impulse and the power to thrust ratio. The results of this work are presented in the following sections.

#### A. Operation of a 30 cm Thruster at Increased Beam Current

The objective of this task was to obtain thruster performance and operational data for operation in the 2 to 4 A beam current range. A goal was to maintain beam voltage as low as possible (or, in other words, to increase it as little as possible from 1100 V). From the outset we recognized that this would present a problem, since the upper current limit for the EMT ion optics design is about 2.5 to 2.75 A at the accelerating voltages usually applied. Consequently, an alternative ion optics design was evaluated. The ion optical system's grid parameters for all assemblies used in this project are listed in Table 9. The high perveance assemblies are the last two entries, SN653 (EMT) and SN822. Although SN822 had, in principle, a higher perveance per hole and a larger number of holes, the ion optics assembly did not produce a higher overall perveance (as seen in Figure 46). The perveance line obtained at constant R (ratio of beam voltage to total voltage) with a typical EMT design grid set is shown for reference. This perveance limit was measured at currents below 2 A with  $R = 0.69$ . It is apparent that the beam extraction capability of grid set SN822 is no better than that of SN653 (EMT design). Failure of the higher perveance design

Table 9. Grid Parameters of the Ion Optical System

Grid Set Serial Number	Screen Grid					Accelerator Grid				Interelectrode Spacing, cm
	Aperture Diameter, cm	Aperture Spacing, cm	Thickness, cm	Open Area, %	Compensation, %	Aperture Diameter cm	Aperture Spacing, cm	Thickness, cm	Open Area, %	
653	0.191	0.221	0.038	67.6	0.4	0.152	0.221	0.051	43.3	0.102
638	0.241	0.279	0.038	67.7	0.5	0.193	0.279	0.076	43.5	0.102
653	0.191	0.221	0.038	67.6	0.4	0.152	0.221	0.051	43.3	0.051
822	0.152	0.178	0.038	66.9	0.5	0.119	0.178	0.051	41.0	0.051

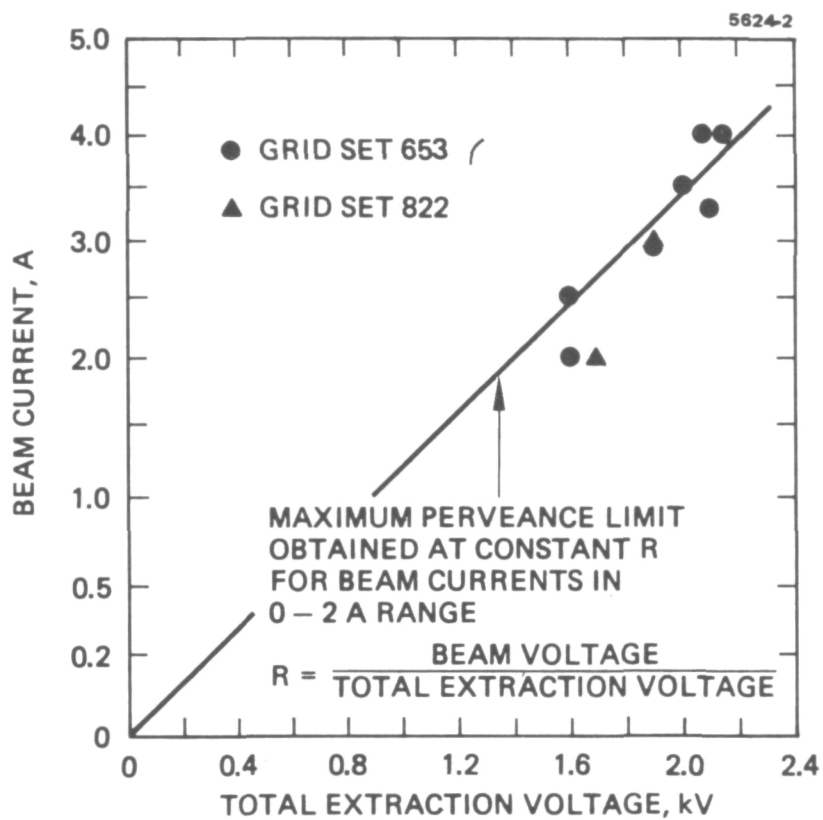


Figure 46. Comparison of high current points with maximum perveance limit measured in the 0 to 2 A beam current range.



to realize the higher perveance is attributed to the thickness of the screen grid relative to the screen aperture diameter. The ion optics are thought to be characterized by the "thick-screen" condition in which the plasma penetrates into the aperture and the effective transmission of the screen grid is less than the physical open area (as compared with greater transmission when the plasma boundary is established upstream of the electrode). Operation with smaller apertures was not pursued strenuously because it offered no apparent advantage and discharge chamber operation was prone to "low-mode" shift. This mode shift could probably have been stabilized by using a different baffle diameter, but emphasis was placed on documenting the high-current operation with grid set SN653 for double ionization, discharge chamber erosion, and any other consequences of high-current operation.

The performance parameters for high beam current operation with grid set 653 are listed in Table 10. Parameters were adjusted to obtain the desired beam current with the minimum beam voltage consistent with operation at accel currents of 0.2 to 0.3% of the beam current. Comparing the measured propellant utilization for the first three entries in the table shows that an increase in beam current at constant discharge losses (eV/ion) and extraction voltage (approximately) produces a decrease in propellant utilization efficiency (note that the double-ion fraction also remains essentially constant). This is considered to be a consequence of operation approaching the perveance limit of the ion optical system and is thought to occur because the plasma boundary moves into the aperture, thereby increasing the ion loss to the screen grid. Improved overall efficiency is produced under perveance-limited operation by increasing the discharge losses (discharge voltage or current), but the doubly charged ion fraction is also increased.

Perhaps the most ominous observation associated with the high-current experiments is the increase in doubly charged ions measured in the ion beam. The thrust loss associated with doubly charged ions is not of great concern, since the overall corrected efficiency is still observed to increase with increasing beam current. The greatest

Table 10. Thruster Performance Data For High Beam Current Operation  
(Parameters Adjusted as Necessary to Obtain Indicated Beam Current)

Beam Current, A	Beam Voltage, V	Accel Voltage, V	Accel Current, mA	Discharge Voltage, V	Discharge Current, A	Discharge Losses, eV/Ion	Propellant Utilization, %	I <sup>++</sup> /I <sup>+</sup> On Beam Axis, %	I <sup>++</sup> /I <sup>+</sup> Average, %	Thrust Factor, $\alpha$	Thrust Factor, $F_t$	Power <sup>b</sup> Efficiency, %	Total <sup>b</sup> Efficiency, (Corrected), %
2.0	1100	500	4.0	37	10	185	95.5	45	14.8	0.957	0.994	83.3	70.6
2.5	1100	500	5.0	37	12.5	185	93.6	49	16.5	0.958	0.98	83.8	68.6
3.0	1200	700	6.7	37	15	185	92	47	16.1	0.959	0.98	85.0	68.2
3.0	1200	700	5.6	38	15	190	95.8	70	20.3	0.951	0.98	84.8	69.8
3.3	1300	800	6.3	36	18.2	199	97	75	20.6	0.950	0.98	85.5	72.5
3.5	1300	700	8.5	37	17.3	183	95.7	65	18.6	0.954	0.98	86.5	71.6
4.0	1210	870	10	38	21	200	98	78	22.5	0.946	0.98	84.8	70.8
4.0	1280	870	9.4	37	22	203	100.2	-	-	-	-	85.2	72.5 <sup>c</sup>

<sup>a</sup>Discharge chamber only, not corrected for doubly charged ions

<sup>b</sup>Assumes 70 W fixed losses and 40 mA (equivalent) neutralizer propellant flow rate

<sup>c</sup>Assumes  $\alpha \approx 0.94$ ,  $F_t = 0.98$

cause for concern is the increasing concentration of doubly charged ions in the discharge chamber because these ions contribute most heavily to the erosion of discharge chamber surfaces. Short-term tests were performed at the 4 A beam current operating point to determine the erosion rates (at the locations shown in Figure 47) with the thin-film erosion monitors. The fastest erosion occurred at location 1, the center of the screen grid, equivalent to 100 nm/hr of molybdenum (Mo/Cu monitors). Erosion at the screen grid mid-radius, location 2, was 72 nm/hr. Tantalum films were used to monitor the baffle surface erosion and the equivalent tantalum erosion rates were 60 nm/hr for location 5 and 24 nm/hr for location 6. These rates are equivalent to about twice the rates that were extrapolated from the 10,000 hr endurance test for 2 A operation (the doubly charged ion concentration at 4 A beam current is also about twice that at 2 A beam current). This amount of erosion presents a life limitation problem in that the eroding surfaces must have adequate material thickness, and the deposits formed by the sputtered material must be accommodated in a manner such that spalling of such deposited coatings cannot form large flakes that could short out the various discharge chamber electrode structures (anode, keeper, extraction grids). Thus, increasing beam current by increasing propellant throughput and discharge power produces an increasing concentration of doubly charged ions in approximately direct proportion to the increase in beam current. Consequently, operating at increased beam current produces higher discharge erosion rates and, if long lifetime is required, provision must therefore be made in thruster design to either accommodate erosion or to reduce erosion rates.

We were concerned at the start of the high-current experiments that the additional discharge power required would produce intolerably high temperatures in the critical components. To determine whether or not this was the case, thermocouples were installed at the locations shown in Figure 48, and the temperatures listed were measured after several hours of operation at 4 A beam current (parameters shown in Table 10). These temperatures are only 20 to 30°C higher than for 2A operation<sup>17</sup> and are considered well within the acceptable range. Note

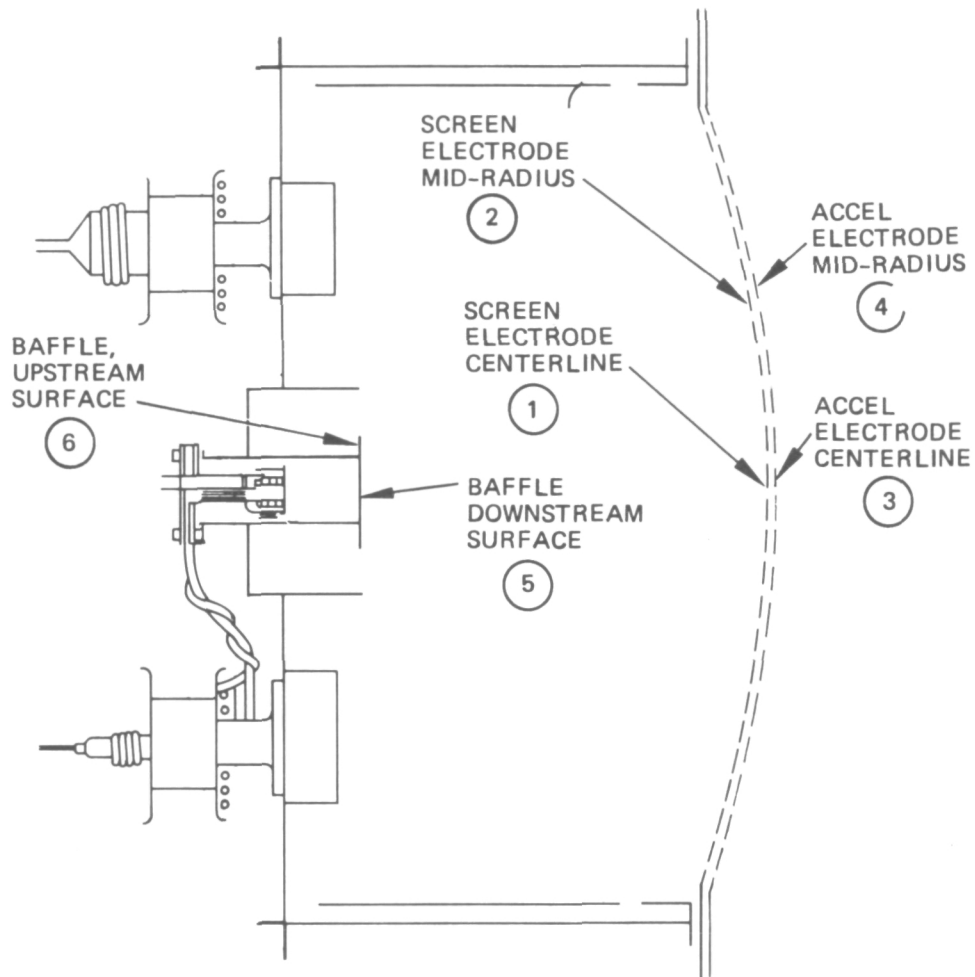


Figure 47. Schematic drawing of thruster discharge chamber showing erosion monitor locations.

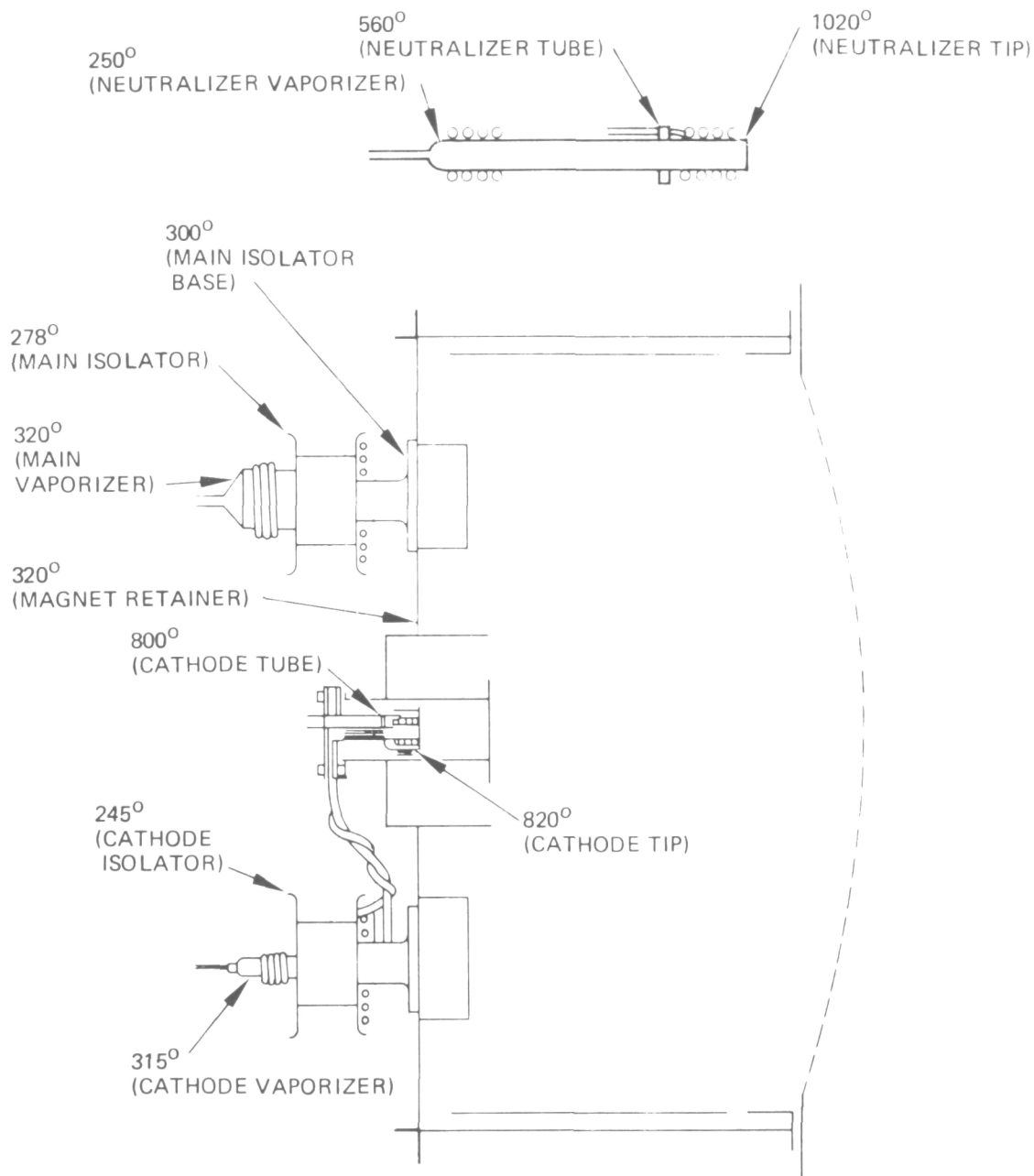


Figure 48. Schematic drawing of thruster discharge chamber showing thermocouple locations and temperatures measured ( $^{\circ}\text{C}$ ) at typical 4 A beam current operating point.

that cathode tip temperatures have not increased appreciably even though emission current is more than twice that at 2 A beam current.

We were also concerned at the start about whether the test facility could be operated at adequately low pressure with a 4 A beam input to the target. This concern also proved to be unfounded; after a short outgassing period, vacuum conditions were maintained adequately. Some comment is appropriate, however, with regard to thruster operating conditions and ion optics interelectrode spacing. Initial thruster testing was attempted with the smallest possible interelectrode spacing of  $\sim 0.5$  mm (0.020 in.) because maximum perveance was desired. Attempts to operate the thruster with this ion optics adjustment were unsuccessful because of excessive overcurrent recycling, although no arcing on the grids could be observed visually. This behavior was eventually traced to large amplitude oscillation in the discharge current at relatively low frequency (period  $\sim 15$  msec). Onset of this oscillation was found to be critically dependent on cathode vaporizer propellant flow rate, main vaporizer propellant flow rate, and magnetic baffle control current. By inserting a 3 mh inductor in the discharge anode lead, it was possible to operate the thruster at beam currents up to 1.5 A; however, the control of propellant flow required was much more sensitive than that required previously to prevent onset of the low-frequency oscillation or shift to "low mode." Any attempt to operate the thruster at higher beam current or without continuous monitoring and readjusting of the vaporizer control produced a shift in operation that resulted in repetitive overcurrent recycle. Although no prior instance where grid spacing had affected thruster operation in this manner was known, it was decided to increase the spacing of the ion optics grids from the nominal 0.051 cm (0.020 in.) spacing to 0.064 cm (0.025 in.). This adjustment changed the range of propellant flow rates consistent with stable thruster operation, although the tendency toward large-amplitude, low-frequency discharge current oscillation was still present. By appropriate adjustment of the discharge parameters and use of the 3 mh inductor in the anode lead, it was possible to operate the thruster at the nominal operating point (37 V discharge

voltage, 185 eV/ion discharge losses) for beam current in the 0.5 to 2.0 A range. Operation at increased beam current was obtained without difficulty following the increase in interelectrode spacing.

B. Operation of a 30 cm Thruster at Increased Beam Voltage

Under this project, the 30 cm thruster was operated at 2, 3, 4, and 5 kV beam voltage and 2 A of beam current. The thruster itself was not modified in any way, but the wiring was replaced and rerouted to avoid any voltage stresses. The propellant electrical isolators were short-circuited and the vaporizers and mercury reservoirs were operated at the thruster cathode potential (beam voltage). Two ion optical system designs were evaluated, and the interelectrode spacings were set at the same nominal value of 0.102 cm (0.040 in.) based on empirical tests. Other parameters for these grids are listed in Table 9 under the first two entries for SN653 and SN638.

Initial testing was conducted at 2 kV beam voltage using grid set SN653 (EMT design). Minimum accel voltage (-300 V) was used because the ion optical system had more than adequate perveance for extracting a 2 A beam. Operation at higher beam voltage with this same accel voltage produced heating of the baffle such that it was observed to glow a dull red. Increasing the magnitude of the accel voltage to -400 V eliminated the baffle coloration without producing discernible effects on the metered quantities. This observation was interpreted as being a consequence of electron backstreaming in the central regions of the ion optical system where the contribution to total current is relatively small but where the plasma and current densities in the extraction apertures are relatively large. To ensure against this phenomena, an accel voltage of -450 V was chosen (rather arbitrarily) as a minimum value for all experiments.

Thruster performance parameters for operation at the higher beam voltages with each of two grid set designs are listed for comparison in Table 11. Since the power associated with ionization of the propellant is approximately constant, beam power increases relative to total power input as beam voltage is increased. Consequently, power efficiency increases as beam voltage increases. Propellant utilization also increases slightly as beam voltage increases. This can be explained by considering the change in the plasma boundary that supplies ions to each extraction system aperture.<sup>7</sup> For higher voltages, this boundary moves upstream, the area of the plasma boundary becomes larger, and the plasma density required to produce a given current becomes smaller. This reduces the neutral density required, which then reduces the neutral loss. At constant beam current, this increases propellant utilization. This effect should diminish as the voltage increment becomes a smaller fraction of total beam voltage (This is illustrated by the data in Table 11).

Of the two grid sets tested, the one with larger apertures showed slightly better overall corrected efficiency. The difference is probably not of great significance, however, since it was of the same order as the experimental error. If a real difference does exist, it may be accounted for by the beam divergence compensation (0.5% as compared with 0.4%) of the grid set (638) that has the larger apertures, since the other parameters are not significantly different. One conclusion from these measurements is that performance parameters are relatively independent of ion optical system parameters when the thruster is operated at beam currents and voltages such that the beam current is well below the "perveance" or "Child's Law" limitation of the ion optical system.



Table 11. Thruster Performance Data

Operating Parameters				Measured Thruster Parameters					Beam Diagnostics					
Grid Set	Beam Voltage, V	Accelerator Voltage, V	Accelerator Current, mA	Total <sup>a</sup> Power Input, W	Total <sup>a</sup> Corrected Efficiency, $\eta_{T, a}$	Power <sup>a</sup> Efficiency, $\eta_p, \eta_v$	Propellant <sup>b</sup> Utilization Efficiency, $\eta_{th}$	Main Vaporizer Propellant Flow Rate, A (Equivalent)	Cathode Vaporizer Propellant Flow Rate, A (Equivalent)	Total <sup>b</sup> Propellant Flow Rate, $m^3/A$ (Equivalent)	Ratio of Doubly Charged Ion Current to Total Current, $\eta_{dc}$	Thrust Reduction Factor, $\sigma$	Thrust Reduction Factor, $\Gamma_t$	Propellant Utilization Factor, $\mu$
653	2000	450	4.0	4,435	73.1	90.2	95.3	2.02	0.079	2.099	16.2	0.952	0.978	0.919
	3000	460	4.1	6,435	-	93.2	96.0	1.97	0.108	2.078	-	-	-	-
	4000	480	3.6	8,435	78.3	94.8	96.5	1.99	0.083	2.073	15.8	0.954	0.979	0.921
	5000	500	5.0	10,435	-	95.8	96.7	1.97	0.094	2.064	-	-	-	-
	2000	450	4.5	4,435	74.1	90.2	94.8	2.03	0.080	2.110	16.1	0.952	0.987	0.918
638	3000	450	4.9	6,435	-	93.2	95.0	2.02	0.085	2.105	-	-	-	-
	4000	540	4.6	8,435	78.8	94.8	96.6	1.97	0.101	2.071	16.6	0.950	0.986	0.916

<sup>a</sup> Assumes neutralizer parameters as follows:  $V_{NK} = 15$  V,  $I_{NK} = 1.3$  A,  $V_g = 12$  V, equivalent mercury flow rate of 0.040 A.

<sup>b</sup> Discharge only.

Note: Data for High Beam Voltage Operation at 2 A Beam Current, 37 V Discharge Voltage and 10 A Discharge Current.

<sup>a</sup> Assumes neutralizer parameters as follows:  $V_{NK} = 15$  V,  $I_{NK} = 1.3$  A,  $V_K = 12$  V, equivalent mercury flow rate of 0.040 A.

<sup>b</sup> Discharge only.

Note: Data for High Beam Voltage Operation at 2 A Beam Current, 37 V Discharge Voltage and 10 A Discharge Current.

### C. Short-Duration Endurance Evaluation

The initial plan for this project was to perform four 100 hr endurance tests to assess thruster wear for operation at high power. By the time all the equipment necessary to operate at high power was obtained, relatively good success had been demonstrated with the multi-layer thin-film erosion monitors. Consequently, three of the 100 hr duration tests were replaced by testing with erosion monitors for approximately 10 (instead of 3) different operating parameter variations. The duration of these tests varied from 4 hr for operation at 4 A beam current to 30 hr for testing EMT SN804. The test results have been reported in the appropriate sections. The point is that such short tests permit relatively rapid evaluation of discharge chamber wear under controlled conditions. In several cases when the chamber pressure became abnormally high at the beginning of the test, the test was stopped and the erosion monitors replaced with one day lost.

Cathode orifice and insert deterioration are not as readily assessed in short duration tests as is surface erosion, and therefore one 100 hr test was performed at the 4A beam current operating point. We monitored keeper voltages, cathode tip temperatures, and vaporizer flow rate characteristics during this test. The test data revealed no appreciable variations or trends. Similarly, the dimensions of the ion optics apertures and cathode orifices were measured using both gauges and photographs before and after the test; the measurements showed no discernible changes.

Reiterating the conclusions, these short duration endurance tests showed that operating the thruster at

- Higher beam voltage has no apparent effect on wear rates
- Higher beam current (up to 4 A) increases the sputtering erosion rate on the screen grid and baffle
- At higher discharge current (up to 22 A) associated with higher beam current has no detectable effect on the cathode operating characteristics or wear rate (no wear).

#### IV. DESIGN AND FABRICATION OF ION OPTICS ELECTRODES FOR LARGE DIAMETER THRUSTERS

This project has explored the requirements for and possible approaches to fabricating ion optics electrodes for thrusters larger than the 30 cm EMT. We concentrated on materials other than molybdenum because of its limited availability in large, thin sheets. Stainless steel was selected for experimental evaluation before the materials analysis was made. This work is discussed in the following paragraphs.

##### A. Alternative Grid Material Study

The objective of this task was to select materials other than molybdenum for 30 cm ion optics. This requirement is prompted by the possibility that sheet molybdenum will not be available in the future, especially in the larger area sheets and/or thinner stock sizes. The selection of a candidate material was limited to those materials that can be fabricated and formed by present techniques.

##### 1. Fabrication Procedure

The 30-cm screen and accelerator electrodes were fabricated from low-carbon arc-cast molybdenum sheets. The blank sheets were first imprinted by a vendor on both sides with a photosensitive material and then exposed to light through a special photomask which contained the grid hole pattern, mounting holes, and outside dimensions. The printed blanks were then returned to HRL to be formed in the special fixture and large hydraulic press shown in Figure 49. The press is capable of forces up to 4.5 MN (500 tons) and is instrumented with pressure controls and gauges, heater controls, and an auxiliary hydraulic system for grid forming. The grids are installed in the fixture and clamped around the grid periphery using 4.5 MN (500 ton) press. The fixture cavity was pumped with a separate supply of hydraulic oil until the desired free-form depth was achieved. The depth was measured by a dial indicator while the process took place.

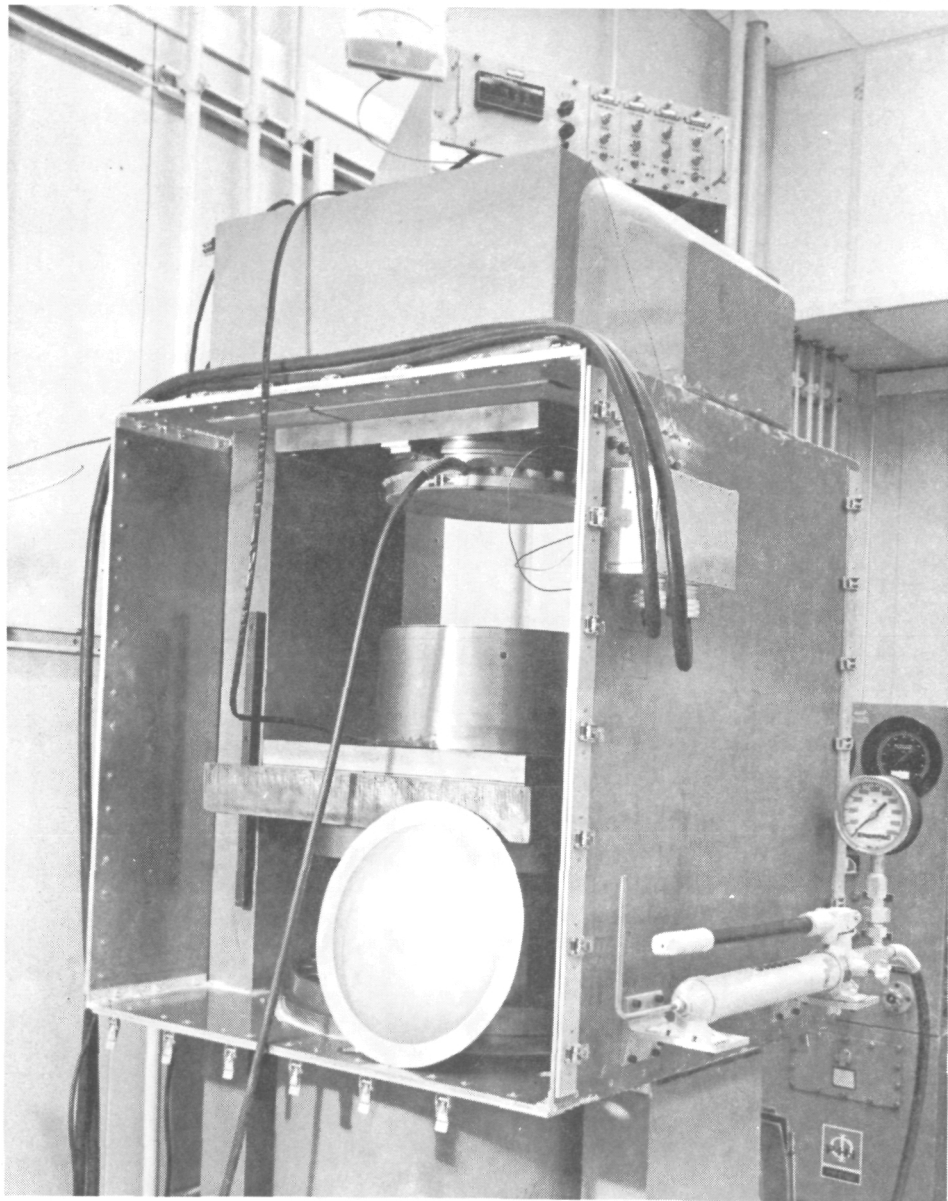
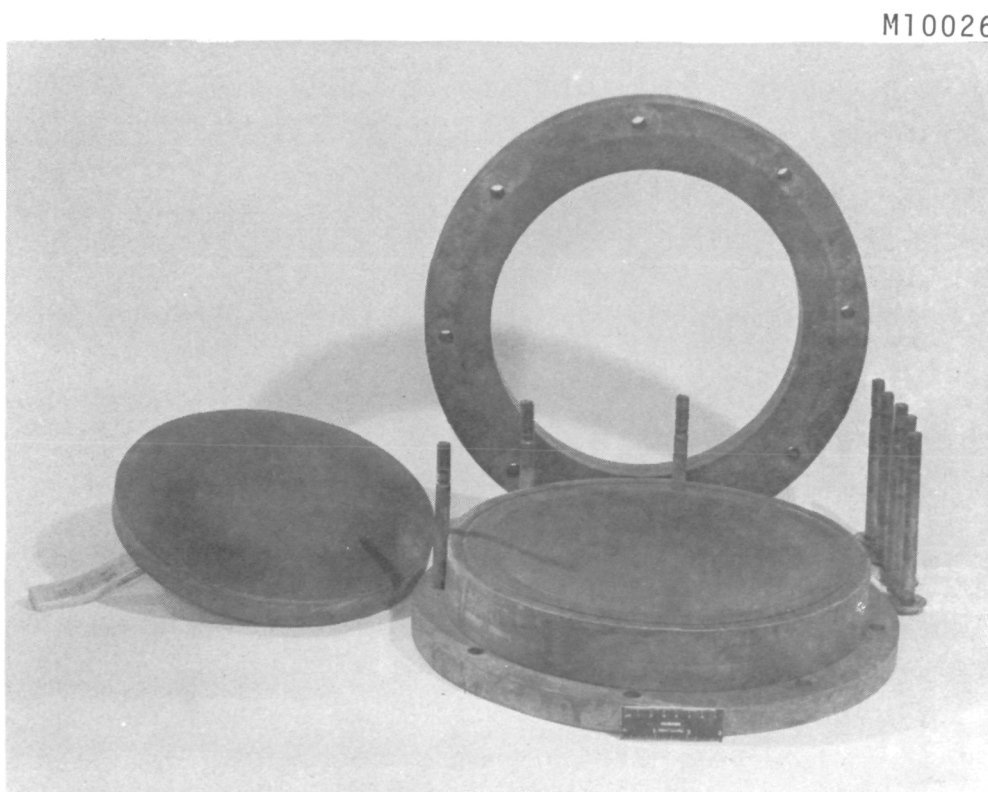


Figure 49. 30 cm dished grid hydroforming press and fixture.

Since molybdenum is more readily formed at temperatures above the ductile-brittle transformation temperature (approximately  $100^{\circ}\text{C}$ ), internal heaters were used to warm the forming fixture and grids in the vicinity of the forming process. The grids, after being formed, were returned to the vendor for final etching of the hole pattern. The grids were then stress relieved in the fixture shown in Figure 50.

## 2. Material Selection

Because the screen grid electrode is vulnerable to sputter erosion, the initial selection of candidate alternative materials to molybdenum was based on sputter yield data. Materials which offer resistance to sputtering comparable to or better than molybdenum include graphite, beryllium, titanium, vanadium, zirconium, iron,



M10026

Figure 50. Grid stress relieving fixture.

tantalum, and columbium. Although graphite has the lowest sputter yield, it was not considered because using it would have required a completely new electrode fabrication process.

Thermal properties of the candidate materials were considered next in importance; our evaluation of these used an analysis by Oglebay<sup>18</sup> and experimental data obtained under NAS3-14140. These studies placed maximum screen electrode temperatures in the 420 to 450°C range. The materials listed above should not present any problems in this temperature range. Oglebay reports that most of the heat transfer from the grids occurs through radiation; consequently, emissivity is more important than thermal conductivity. Thermal emissivity depends as much on surface conditions as on the material used. Fabrication by chemical milling requires a brightly finished surface on the original sheet stock for good photoresist adherence; such a surface would not be expected to exhibit good thermal emissivity. Subsequent surface treatment could be used to improve the emissivity if it could be applied in a manner compatible with the curved, perforated electrode configuration. This aspect of material choice was reconsidered after choices had been narrowed down somewhat. Thermal conductivity was not a consideration in the evaluation.

The fabrication techniques which were developed at HRL and NASA LeRC require sufficient ductility for hydroforming and suitability for chemical milling using photoresist masking techniques. This latter requirement results in the greatest variance between candidates. Titanium, while being favorable in most other considerations, is very corrosion resistant to the most frequently used etching agents. Therefore, the machinery and apparatus used by all the commercial vendors who have etched the molybdenum grids contains a large number of titanium components which would be imperiled if they were to attempt etching of titanium. If titanium seems most desirable, it may be possible to locate a vendor equipped to process the titanium. Tantalum and columbium are in the same category as titanium from the standpoint of chemical machining. Three vendors were contacted on the subject of etching these materials.

The principal vendor for molybdenum grids has etched columbium on a commercial basis but has discontinued offering this service and will not consider tantalum. Another vendor has fabricated molybdenum grids for 8 cm thrusters but will not consider etching tantalum or columbium. A third vendor would consider etching either tantalum or columbium, but on a totally experimental best-effort basis. The largest sheet they can handle would be 61 by 91 cm (24 by 36 in.) and their cost estimate was significantly greater than the present cost for etching molybdenum.

On the positive side for tantalum and columbium, both materials are thought to have a lower sputtering yield than molybdenum. Tantalum is 60% heavier than molybdenum; columbium is 16% lighter. Both materials benefit from alloying with tungsten to increase their tensile strength and such alloys are readily available. Both tantalum and columbium have a slightly higher coefficient of linear thermal expansion.

Availability of the materials in sheet stock is also a consideration; however, there does not appear to be any advantage of one material over another for those on the list.

Another consideration studied was the requirement for special handling procedures in fabrication or testing. Two materials on the list are potentially hazardous and will not be pursued further for that reason. Beryllium is highly toxic in finely divided form and would present a problem in machining and in the vacuum facilities used for testing. Zirconium is pyrophoric and therefore would also be dangerous in fabrication processes and in vacuum facilities where sputtered material collects over a period of time.

Of the two remaining materials, iron and vanadium, iron could require a major change in the thruster because it is magnetic. Similarly, iron is not greatly different in its properties from stainless steel, which has been used in fabricating and evaluating a set of 30 cm grids. Availability of vanadium in the 41 by 41 cm (16 by 16 in.) sheet, which is the electrode blank size, is still in question.

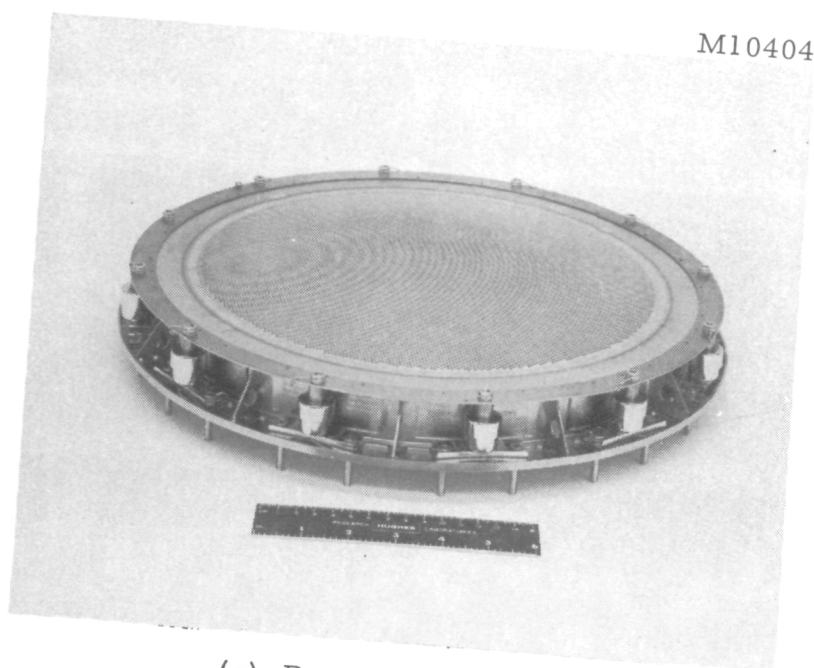
Thus, there appears to be no clear alternative to molybdenum as a material for grid fabrication. Molybdenum is available in 61 x 16 cm (24 x 36 in.) sheet size from either arc cast or pressed and sintered forming process suppliers. Tantalum alloyed with 10% tungsten would be desirable from a sputtering rate consideration, but the chemical milling process would have to be developed in a commercial vendor. Although this may seem like a relatively large technology requirement, it is not altogether different from the situation at the time chemically milled molybdenum grids were first considered. Thus, tantalum, columbium, or titanium are the recommended alternate choices in order of preference, preference being based on thermal expansion considerations.

#### B. Stainless-Steel Grid Ion Optics Assembly

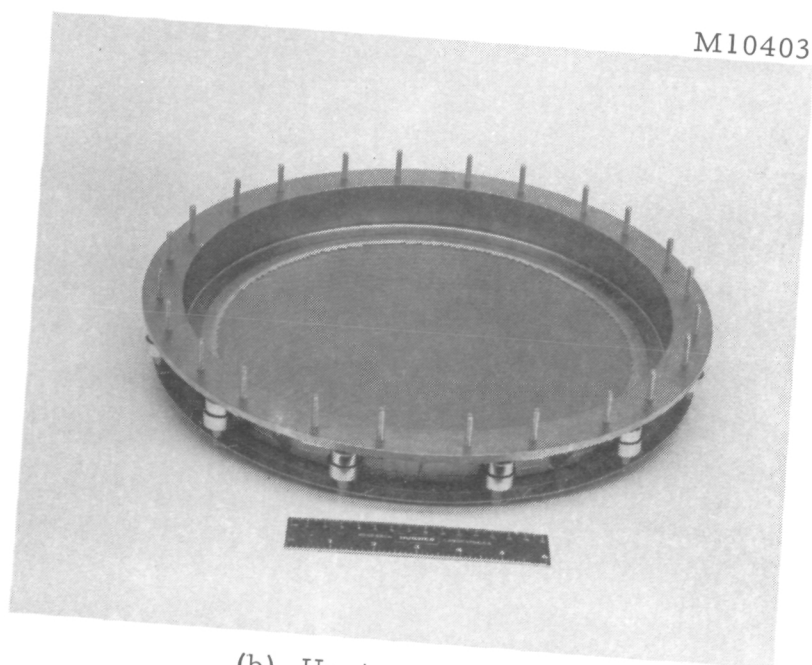
A set of stainless-steel electrodes was fabricated and tested under this project. The electrode specifications were the same as those of the EMT molybdenum grids (or grid set SN653). Hydroforming and chemical milling of the apertures was accomplished without difficulty. Because there was concern for the ability of the photo-resist mask to withstand the temperature normally established in hydroforming molybdenum grids, the hydroforming or "dishing" was done without heating. Material thinning occurred uniformly, varying from 0.0018 cm (0.0007 in.) at the center to 0.00025 cm (0.0001 in.) at the edge of the curved portion of the grid. There was no evidence of coating failure and the apertures were etched successfully.

The grids were subsequently stress relieved and assembled on the EMT design titanium mount shown in Figure 51, and the initial interelectrode spacing was set according to EMT specifications (0.051 to 0.064 cm or 0.020 to 0.025 in. at the center and half radius locations). The assembly was then installed on thruster SN301B for test.





(a) Downstream view



(b) Upstream view

Figure 51. Ion optical system assembly using titanium support ring.

Initial test of the stainless-steel grid set followed the normal start-up procedure using a 30 min pre-heat period for cathodes and vaporizers, obtaining cathode and discharge ignition, and a 10 min discharge stabilization period at full discharge power before application of the beam and accel voltages. Using this start-up procedure, an attempt to apply the high voltage after the 10 min discharge operation produced a short-circuited electrode symptom. The interelectrode resistance was subsequently measured and a direct short was confirmed. The main discharge voltage was shut off and the interelectrode resistance was monitored. No change occurred, so the keeper discharge was also extinguished. Within a short time, the interelectrode resistance measurement indicated an open circuit. To confirm the assumption that this effect was thermally driven, the main keeper discharge was re-established and the interelectrode resistance monitored. Within a short time, the short-circuit condition was again observed and the test was terminated.

Several attempts were made to re-space the electrodes to larger interelectrode spacing so that the increased thermal expansion of the grids could be allowed without interelectrode contact. With the interelectrode spacing adjusted as shown in Figure 52, it was possible to extract and maintain an ion beam up to 1 A of beam current. Thruster operation was unstable, however, because the overload trip (arc) rate was high and consequently it was not possible to obtain meaningful perveance or propellant flow data. The overloads were related to visible arcs that occurred repetitively in the region indicated on the spacing chart shown as Figure 52. The thruster was allowed to run (under the frequent arcing condition) for several hours, but there was no indication of any reduction in arc rate. Inspection of the electrodes after this test showed some electrode discoloration in the region of arcing but no other signs to indicate a reason for arcing (such as protrusion, distortion, etc). One final attempt was made with the grids spaced approximately 0.0127 to 0.0254 cm (0.005 to 0.010 in.) farther apart than shown in Figure 53, but the test results were essentially the same. Examining the assembly carefully after the test, it was noted that the

**30 cm OPTICS ASSEMBLY RECORD  
SCREEN ACCELERATOR SPACING CHART**

DATE: 7-20-76  
TECH: H.T.

MOUNTING RING ASSEMBLY S/N EXP  
ACCELERATOR ELECTRODES S/N 824  
NOTES: STAINLESS STEEL

TYPE 0.830 DISH  
DRAWING NO. \_\_\_\_\_  
APERTURE dia \_\_\_\_\_  
SPACING CTR/CTR \_\_\_\_\_  
THICKNESS \_\_\_\_\_

SCREEN ELECTRODES S/N 824  
NOTES: STAINLESS STEEL

DRAWING NO. \_\_\_\_\_  
APERTURE dia \_\_\_\_\_  
SPACING CTR/CTR \_\_\_\_\_  
THICKNESS \_\_\_\_\_  
REDUCTION (%) 0.5%

2769-5R1

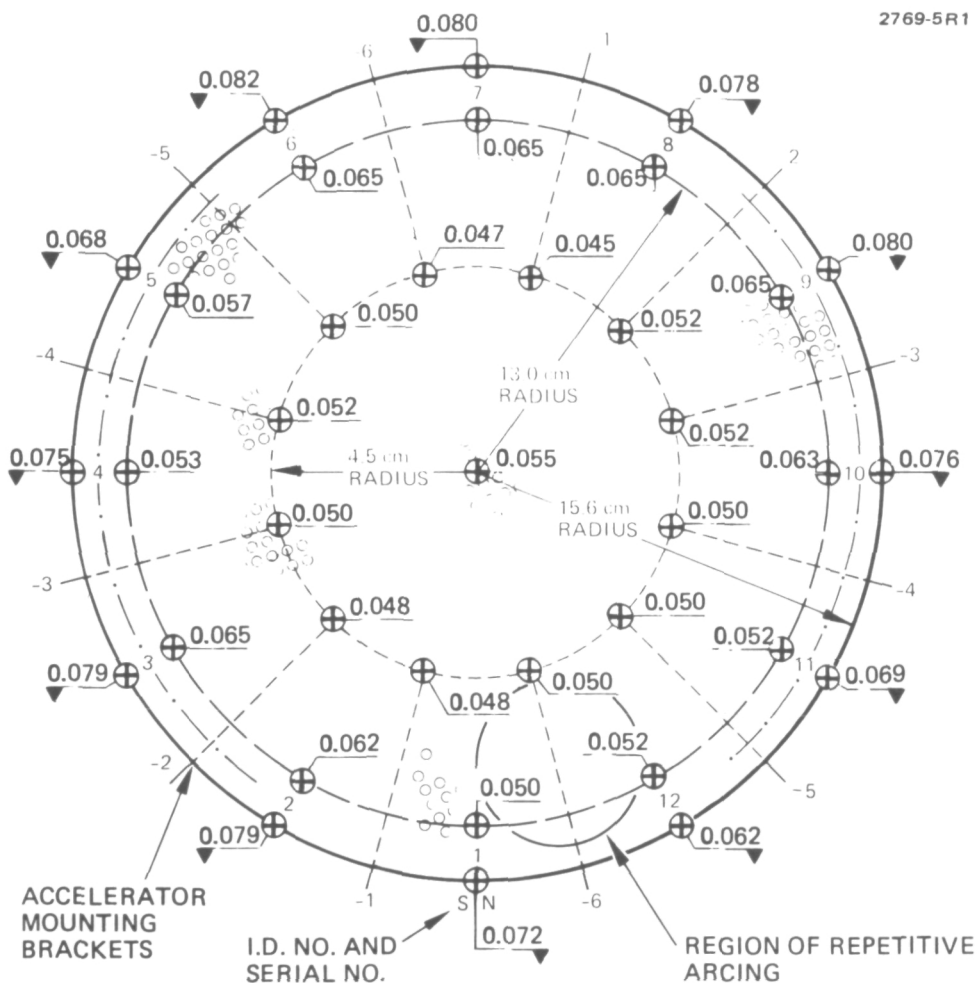


Figure 52. Stainless steel electrode spacing chart showing region of arcing.

screen grid was "bowed" and lifted up from the titanium mount between each of the attaching screws. The conclusions drawn from these experiments are as follows:

- The coefficient of linear expansion for stainless steel is three times that of molybdenum, and consequently the electrode movement is significantly greater for stainless steel than for molybdenum grids.
- The requirement for greater linear expansion results in local distortions of the electrode surfaces as a result of the normal temperature gradients.
- Successful operation of stainless-steel electrodes would require a mounting system and a dish configuration that could accommodate larger electrode movement without geometric distortions.

## V. CONCLUSIONS

The work performed under the High-Power and 2.5 kW Advanced-Technology Ion Thruster Program produced the following conclusions. Improvements to 30 cm ion-thruster technology are still possible with respect to reducing ion sputtering erosion and thereby extending thruster lifetime. Significant gains in reducing ion sputtering could require relatively major modifications in the discharge chamber design. Thruster operation at higher beam voltage or current presents no significant difficulties but has implications on thruster lifetime and component design.

As stated above, the main problem area for 30 cm ion-thruster technology is the erosion of the discharge chamber by ion sputtering (in particular, the screen grid and the baffle). A technique using multiple thin layers of alternating materials was shown under this program to be useful in evaluating erosion rates in relatively short time periods. The accuracy of the technique and the influence of ambient conditions have not been adequately investigated, however. Investigation of double-ionization processes has been successful to the extent that parametric relationships between double ionization and causal factors are now relatively well understood. Unfortunately, little progress has been made in finding a means of reducing double ionization without also sacrificing some performance characteristic. The most promising approaches to reducing erosion are concluded to be the reduction of accelerator grid hole diameter to reduce neutral loss rate and modification of the discharge chamber primary electron region to produce a more uniform, lower density plasma. Substantial opportunity remains for investigating modifications to implement these concepts in an optimal way.

Considering that discharge chamber erosion cannot be eliminated altogether, the hazard exists that metallic flakes of backspattered deposits will bridge and short-circuit the closely spaced ion optics electrodes. A technique for removing such short circuits was

demonstrated under this program using a capacitive discharge; it did not cause appreciable electrode damage. It is concluded that including a circuit to perform this function would remove the threat of short-circuited ion optics causing premature thruster failure during flight operation.

From the study of the thruster magnetic circuit, it can be concluded that the distribution of magnetic induction throughout most of the discharge chamber volume is relatively insensitive to the configuration of the polepiece and magnet and that the permanent magnets themselves are most important to reproducing the magnetic mapping. Measurements do indicate that the magnetic circuit around the cathode itself is quite critical and it is concluded that a less sensitive geometry would simplify production of identical thrusters (from an operational standpoint).

The tests performed on barium impregnated porous tungsten of the type now in use for cathode inserts were not totally conclusive; however, insert lifetime should prove adequate at anticipated operating temperatures. Because of this, it can also be concluded that the hollow-cathode configuration developed, which requires neither cathode heater nor alkaline earth material, offers no appreciable advantage over the conventional thruster hollow cathode for present operational requirements.

Finding a source of suitable porous tungsten vaporizer material has presented a recurring problem until now. On the basis of the samples tested, porous tungsten formed using 4.5  $\mu\text{m}$  particles, pressed and sintered to 80% density by Spectra-Mat, Inc., is concluded to meet specifications for cathode and neutralizer vaporizers.

High-power operation of a 30 cm thruster representative of the EMT design presents no significant difficulties. Beam currents of up to 4 A can be obtained with slight increases in accelerating voltages, and thruster operation is effected only with respect to wearout lifetime. Double ionization is increased in proportion to increasing beam current and so is the corresponding erosion of the discharge chamber. High current operation should not present any problems in situations where

shortened life is not a factor. Operation at higher beam voltage (and constant current) only requires extending insulation capacity. This implies adjusting the ion-optics interelectrode spacing and using an appropriate propellant isolator. Propellant isolators were not explored and higher voltage operation ( $>1500$  V) would require a new isolator design.

The study of materials as alternatives to molybdenum for fabrication of ion optics electrodes led to the conclusion that no other material offers a possibility as a direct substitute for molybdenum electrodes using the same design and the procedures now being used to fabricate them. The implication is that a new material would require a new ion optics assembly design and development, including fabrication procedures.

## REFERENCES

1. R.P. Vahrenkamp, "Measurement of Doubly Charged Ions in the Beam of a 30-cm Mercury Bombardment Thruster," AIAA Paper 73-1057, Lake Tahoe, Nevada, October, 1973.
2. C.R. Collett, et al., "Thruster Endurance Test," NASA CR-135011, Hughes Research Laboratories, May, 1976.
3. C.R. Collett, "A 7700 Hour Endurance Test of a 30 cm Kaufman Thruster," AIAA Paper No. 75-366, New Orleans, Louisiana, March, 1975.
4. W.S. Williamson and J. Hyman, Jr., "Discharge Chamber Sputtering Investigation," AIAA Paper No. 76-1026 International 12th Electric Propulsion Conference, Key Biscayne, Florida, November, 1976.
5. D.D. Beebe, A. Nakanishi, and R.C. Finke, "Electric Arc Discharge Damage to Ion Thruster Grids," NASA TM X3044, May, 1974.
6. J.W. Ward and R.P. Vahrenkamp, "Characterization of Ion and Neutral Efflux from a 30-cm Mercury Ion Thruster," AIAA Paper 75-357, New Orleans, La., March, 1975.
7. H.R. Kaufman, "Technology of Electron Bombardment Thrusters," Advances in Electronics and Electron Physics Vol. 36, Academic Press, Inc., San Francisco, 1974.
8. G. Aston, "The Ion-Optics of a Two Grid Electron-Bombardment Thruster," NASA CR-135034, Colorado State University, May, 1976.
9. V. Rawlin, "Performance of 30-cm Thrusters with Dished Accelerator Grids," AIAA Paper 73-1053, Lake Tahoe, Nevada, October, 1973.
10. R.R. Peters, et al., "A Doubly Charged Ion Model for Ion Thrusters," AIAA Paper 76-1010, Key Biscayne, Florida, November, 1976.
11. T.D. Masek, "Plasma Properties and Performance of Mercury Ion Thrusters," AIAA Journal 9, No. 2, February, 1971.
12. J.W. Ward and T.D. Masek, "A Discharge Computer Model for an Electron Bombardment Thruster," AIAA Paper 76-1009, Key Biscayne, Florida, November, 1976.



13. L.M. Lidsky, et al., J. Appl. Phys. 33, 2490, August, 1962.
14. J.S. Sovey and H.J. King, "Status of 30 cm Mercury Ion Thruster Development," AIAA Paper No. 74-1117, AIAA/SAE 10th Propulsion Conference, San Diego, CA, October, 1974.
15. R. Bechtel, "A Hollow Cathode Neutralizer for a 30 cm Diameter Bombardment Thruster," AIAA Paper 73-1052, Lake Tahoe, November, 1973.
16. M.J. Mirtich and W.R. Kerslake, "Long Lifetime Hollow Cathodes for 30 cm Mercury Ion Thrusters," AIAA Paper No. 76-985, AIAA International Electric Propulsion Conference, Key Biscayne, Florida, November, 1976.
17. R.L. Poeschel and R.P. Vahrenkamp, "Performance Mapping of a 30 cm Engineering Model Thruster," AIAA Paper No. 75-342, New Orleans, La., March, 1975.
18. J. Oglebay, "A Thermal Analytic Model of a 30 cm Engineering Model Mercury Ion Thruster," AIAA Paper 75-344, New Orleans, La., March, 1975.

## APPENDIX A

The Langmuir probe data for each case listed in Table 4, p. 42 is presented in Tables A-1 through A-5 for the measurement locations shown in Figure A-1.

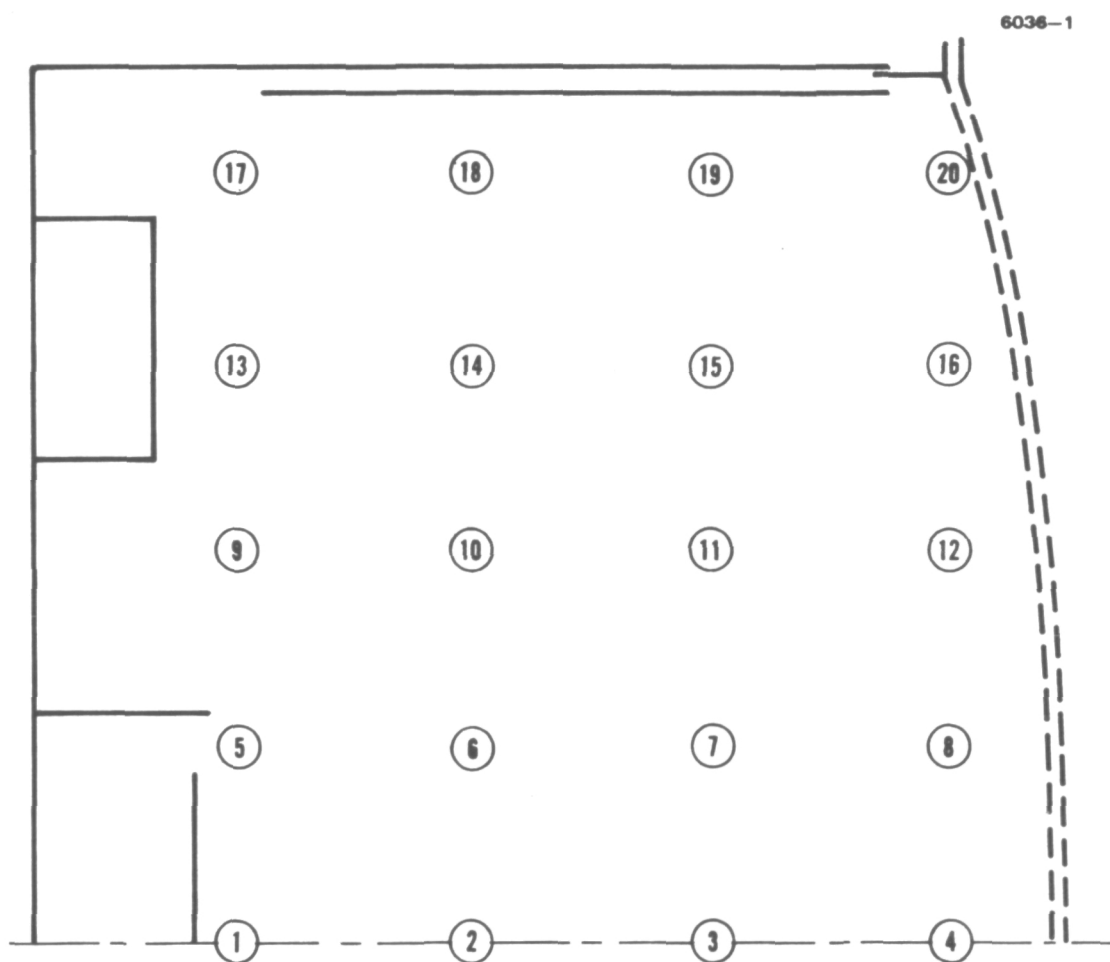


Figure A-1. Thruster schematic showing location of Langmuir probe data points.

Table A-1. Langmuir Probe Data

EM Optics,  $I_B = 2.0$  A

Probe Location	$\phi$	$T_e$	$E_p$	$n_p \times 10^{11}$	$n_m \times 10^{11}$
1	33.0	3.3	26.4	0.30	1.8
2	36.9	3.5	27.2	0.51	2.9
3	36.2	4.0	29.0	0.59	2.6
4	33.9	3.8	28.1	0.46	1.9
5	37.0	4.1	29.3	0.45	1.65
6	38.5	4.5	30.2	0.66	2.2
7	35.1	3.8	28.1	0.51	1.9
8	32.9	3.7	26.9	0.49	1.7
9	38.9	1.5	0	0	0.55
10	40.2	4.2	28.6	0.29	1.5
11	35.0	3.5	26.6	0.43	1.55
12	32.8	3.6	26.6	0.42	1.66
13	41.0	1.9	0	0	0.29
14	42.3	3.4	0	0	0.70
15	36.9	3.8	28.4	0.36	1.2
16	31.0	3.4	25.8	0.40	1.2
17	41.4	1.95	0	0	0.24
18	45.0	3.3	0	0	0.39
19	36.8	3.4	27.5	0.21	0.77
20	23.8	6.1	0	0	1.0

Table A-2. Langmuir Probe Data  
EM Optics,  $I_B = 1.5$  A

Probe Location	$\phi$	$T_e$	$E_p$	$n_p \times 10^{11}$	$n_m \times 10^{11}$
1	32.5	3.6	26.5	0.41	1.1
2	33.9	3.1	25.0	0.41	1.4
3	32.4	3.1	24.5	0.31	1.3
4	31.0	3.1	24.2	0.28	1.0
5	33.5	3.9	26.3	0.31	0.85
6	34.7	3.4	26.1	0.46	1.0
7	33.1	3.4	25.4	0.35	1.1
8	30.5	3.2	24.1	0.27	0.88
9	37.1	1.6	0	0	0.22
10	36.8	3.2	24.7	0.16	0.63
11	34.5	3.8	26.8	0.38	0.86
12	30.7	3.3	25.0	0.34	0.86
13	39.3	1.9	0	0	0.12
14	38.5	2.5	0	0	0.29
15	34.3	3.5	26.0	0.18	0.63
16	29.0	3.4	23.5	0.29	0.63
17	39.1	1.9	0	0	0.10
18	37.7	2.0	0	0	0.18
19	34.5	3.3	25.5	0.15	0.37
20	20.0	5.0	0	0	0.57

Table A-3. Langmuir Probe Data  
EM Optics,  $I_B = 1.0$  A

Probe Location	$\phi$	$T_e$	$E_p$	$n_p \times 10^{11}$	$n_m \times 10^{11}$
1	32.2	3.8	26.9	0.40	0.92
2	35.0	3.2	27.3	0.46	1.3
3	32.5	3.2	26.2	0.71	0.95
4	31.7	3.5	26.0	0.36	0.77
5	32.2	3.0	26.1	0.39	0.71
6	36.0	4.1	28.8	0.56	1.1
7	31.8	3.3	25.4	0.45	0.84
8	30.5	2.9	25.3	0.36	0.80
9	39.0	2.2	0	0	0.22
10	37.3	3.6	27.3	0.21	0.40
11	31.8	2.9	25.5	0.35	0.72
12	29.6	3.7	25.8	0.37	0.55
13	38.9	1.8	0	0	0.16
14	39.0	1.6	0	0	0.28
15	33.9	3.4	26.1	0.23	0.43
16	26.0	3.3	22.1	0.27	0.49
17	38.6	1.4	0	0	0.093
18	38.4	1.5	0	0	0.20
19	33.0	2.8	23.8	0.16	0.30
20	15.0	3.9	0	0	0.50

Table A-4. Langmuir Probe Data  
SHAG 1 Optics,  $I_B = 2.0$  A

Probe Location	$\phi$	$T_e$	$E_p$	$n_p \times 10^{11}$	$n_m \times 10^{11}$
1	25.3	2.6	20.6	0.27	1.4
2	28.2	2.3	20.0	0.38	2.7
3	27.3	2.4	19.9	0.35	1.9
4	24.6	2.3	19.1	0.24	1.4
5	26.5	2.5	19.9	0.33	1.2
6	29.0	2.6	21.0	0.49	2.1
7	27.3	2.5	20.3	0.39	1.8
8	25.0	2.5	19.5	0.27	1.4
9	31.4	1.1	0	0	0.39
10	29.5	2.4	19.1	0.20	1.0
11	26.7	2.4	20.0	0.39	1.5
12	23.0	2.2	18.6	0.25	1.3
13	--	--	--	--	--
14	32.7	2.1	10	0.09	0.41
15	27.6	2.7	20.0	0.21	0.8
16	21.5	2.3	17.5	0.19	1.1
17	--	--	--	--	--
18	--	--	--	--	--
19	28.6	2.5	20.0	0.12	0.53
20	16.0	3.7	0	0	0.75

Table A-5. Langmuir Probe Data  
SHAG 1 Optics,  $I_B = 1.5$  A

Probe Location	$\phi$	$T_e$	$E_p$	$n_p \times 10^{11}$	$n_m \times 10^{11}$
1	24.3	2.2	18.5	0.14	1.1
2	28.3	2.5	20.3	0.27	1.9
3	26.4	2.3	19.0	0.20	1.4
4	24.1	2.2	18.4	0.14	1.1
5	18.3	1.8	13.6	0.13	1.0
6	27.8	2.6	20.3	0.32	1.7
7	25.5	2.4	18.8	0.21	1.3
8	23.8	2.2	18.6	0.15	1.0
9	30.8	0.97	0	0	0.22
10	29.1	2.7	20.1	0.14	0.68
11	26.4	2.8	19.8	0.25	1.0
12	22.3	2.5	18.4	0.13	0.89
13	--	--	--	--	--
14	32.1	2.3	0	0	2.0
15	27.3	2.7	19.3	0.14	0.56
16	18.3	3.7	0	0	0.68
17	--	--	--	--	--
18	--	--	--	--	--
19	26.6	2.4	18.5	0.053	0.27
20	18.5	4.2	0	0	0.41